Università
Ca'Foscari
Venezia

Master's degree programme in

Chimica e tecnologie sostenibili

Final thesis

A study on lead halide perovskites: preparation and characterization

Supervisor:
Prof. Patrizia Canton

Graduand:
Erica Galvagno
Matriculation number: 866557

Academic year:
2021/2022

INDEX

1. INTRODUCTION

In the last decade, metal halide perovskites (MHP) have been amply studied because of their remarkable properties which can be tuned to be exploited into a vast range of applications. Most notably, metal halide perovskite nanocrystals possess optoelectronic properties similar to the ones seen in bulk perovskites, but enhanced by effects associated to their smaller sizes, leading to a considerable array of characteristics such as tunable band gaps, narrow emission, strong light-absorption coefficients, and high defect tolerance [1]. For this reason, they are used in a variety of applications as components of optoelectronic devices; to name a few: photovoltaic solar cells, lasers, catalysts for photocatalysis, sensitive photodetectors and light-emitting diodes (LEDs) [2; 3; 1]. Beside their extensive array of uses, these materials are relatively straightforward to synthesize and there have been many developments in their shape-controlled synthesis. This thesis focuses on lead halide perovskites (LHP) nanocrystals, which present two main environmental problems: lead's well-known toxicity and bioaccumulation in the ecosystem and the employment of problematic solvents in the conventionally used synthetic pathways [3; 4; 5].

The first section of this work will include a theoretical discussion which will touch on all the main aspects of halide perovskite nanocrystals necessary to give a general idea of their features. Consequently, the common structures, the optical properties and the synthetic processes will be reviewed. Furthermore, a variety of relevant topics, including post-synthetic treatments and environmental problematics, will be examined so as to supply a complete view of the topic.

The second part will instead describe the experimental elaborations that were carried out. First, a conventional hot-injection synthesis will be dealt with, in order to gather some basic information on the desired products as a starting point to then determine the aspects that need improving. Then, a new synthetic approach will be developed with the purpose of substituting some critical reaction features with greener alternatives. First of all, the approach will be developed at room temperature and ambient conditions, in order to avoid the main problems associated with the hot-injection method, that generally does not allow the scaling up of the process and that requires higher costs. In addition, the conventional solvents used at room temperature, dimethylformamide (DMF) and dimethyl sulfoxide (DMSO), will be discarded and substituted with water, a green solvent. Taking into consideration the fact that this synthetic method has not been implemented before, the obtained nanocrystals will be characterized to clarify the outcome of this procedure. Such characterization will be primarily conducted through X-ray diffraction (XRD), scanning electron microscopy (SEM) and photoluminescence investigations. In addition, infrared (IR) spectroscopy will be used for the analysis of the final products to investigate the coordination of the capping ligands to the surface. Overall, these techniques will allow to rationalize the structure, size and shape of the final nanomaterials and to evaluate their optical properties for future applications.

2. THEORETICAL SECTION

Perovskites are a class of compounds defined by the general formula ABX_3. This category includes materials with structures similar to $CaTiO_3$, the first mineral discovered owning the typical "perovskite arrangement". This mineral's name was given to the compounds discussed and it was chosen in honour of Alekseyevich von Perovski [6; 7; 1]. The minerals included into this group present an array of phases, but the study of their structures can be generalized by considering them ionic compounds made up by two cations, the larger monovalent A and the smaller divalent B, and an anion, X [8; 9]. As was anticipated in the introduction of this thesis, the focus will be on lead halide perovskites, so the B ion is a divalent lead cation and the X sites are occupied by halide monovalent anions (chloride, bromide and iodide). Generally, lead halide perovskites can be distinguished into organic-inorganic hybrid (OIH) or inorganic, depending on the nature of the A cations; the firsts are characterized by organic A-site cations, such as methylammonium (MA) and formamidinium (FA), while inorganic perovskites usually present caesium or rubidium in the A-sites [10; 5; 11]. The first part of this introduction will be dedicated to briefly rationalizing the main structures of lead halide perovskites. From now on the term "perovskite" will be used to indicate the more specific class of lead halide perovskites.

After that, their main optical properties will be delineated focusing, in particular, on perovskite nanocrystals, the topic of this work. The enormous variety of perovskite-like compounds is reflected in the range of their properties, which is an attractive requirement for the purpose of exploiting these materials in numerous technological fields. For example, metal halide perovskites are vastly used for solar cells, light-emitting diodes, lasers, photodetectors, photocatalysts and transistors, thanks to their optical and electronic properties [12; 13; 5; 14]. Some of the most diffused applications will be briefly listed at the end of the theoretical portion of this thesis.

Before that, the main synthetic approaches and some of the post-synthetic procedures will be amply discussed as an introduction to the experimental part, where the hot-injection method and an innovative room temperature method will be studied. Lastly, a paragraph will focus on the toxicity and environmental issues of lead halide perovskites and their conventional synthesis.

2.1 Perovskites structures

As introduced, this chapter gives a general idea of the placement of cations and anions in the structure and of the broad variety of dispositions that can assume the ions in this class of compounds. It will in fact contain a brief description of some of the main architectures seen in perovskites, but it will not include, for one, all the details regarding the dependence of perovskite structures from changes in temperature and pressure.

2.1.1 Cubic structure

Ideally, perovskites are considered to have a cubic structure where: A atoms are arranged on each corner of the cubic cell, B cations occupy the centre and X anions lie at the centre of each face of the cube in an octahedral disposition (Figure 1) [8; 9; 15].

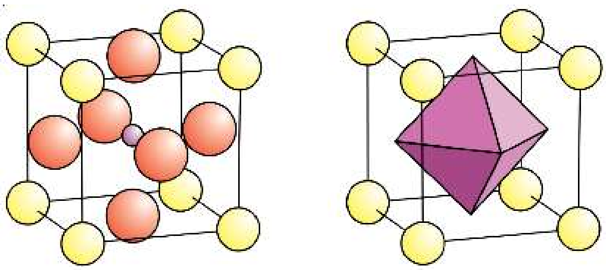

Figure 1. The atom positions are shown on the left side of the picture, while the octahedron of anions is represented on the right side [9]. In this picture: A cations = yellow spheres; B cations = purple spheres; X anions = red spheres.

This same structure can also be seen from another point of view in which A cations occupy the centre of the cubic cell, B cations lie at the corners and X anions are arranged at the midpoints of the cube's edges (Figure 2) [16; 9]. The octahedron of atoms, that forms from the BX_6 configuration and contains the bigger A cation at the centre, is connected to the other octahedra by sharing the corner halides [17; 4; 1].

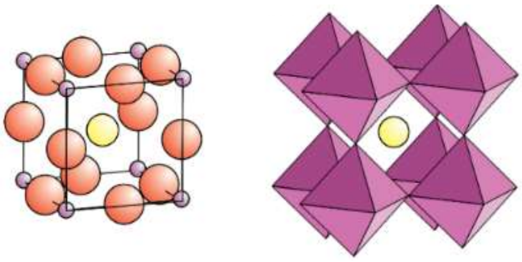

Figure 2. The atom positions are shown on the left side of the picture, while the octahedra of anions is represented on the right side [9]. In this picture: A cations = yellow spheres; B cations = purple spheres; X anions = red spheres.

Perovskites following this ideal structure are defined aristotype perovskites [6; 9; 15].

2.1.2 Structural distortions

The highly symmetric cubic structure described in the previous paragraph is not always observed under normal conditions because perovskites tend to distort towards different phases [18; 1]. In particular, a tetragonal or an orthorhombic phase, characterized by a lower symmetry, are also possible [17; 11].

Three main changes in the ideal structure are: B-cation displacement (Figure 3), BX_6 tilt/rotation (Figure 4) and BX_6 distortion (Figure 5) [16; 9; 19]. The first two modifications maintain the perfect octahedral geometry of BX_6 units, but they can be distinguished depending on the involved ions. On the one hand, B-cation displacement presents B cations too small for the octahedral site, with a consequent displacement of such cations from the centre of the octahedra. On the other hand, in BX_6 tilt/rotation, A cations are too small for the structure, resulting in a twist of the octahedra to reduce the cavity dimensions [16; 18; 9]. Both these changes can have consequences on optical, electrical and other physical properties [16].

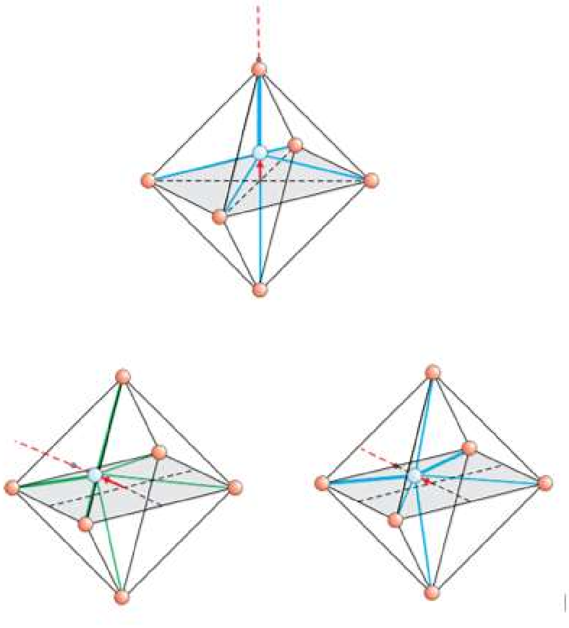

Figure 3. Cation displacement along three different axes [9]. In the picture B cations are the light blue spheres in the centre and X anions are the orange spheres.

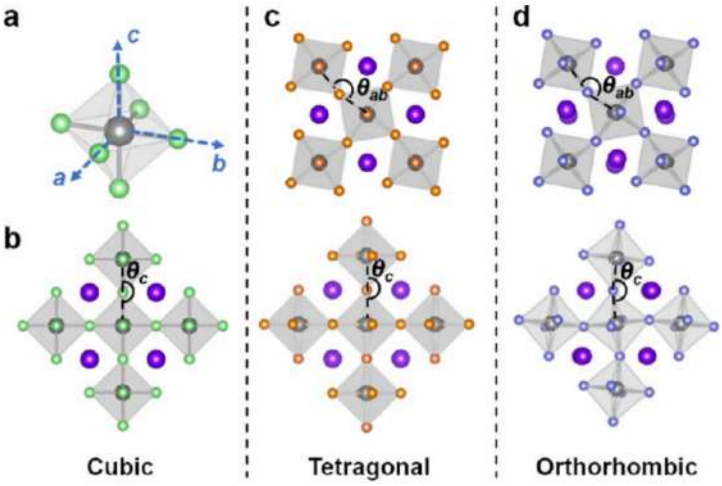

Figure 4. BX_6 octahedra tilt/rotation along different axes, equatorial (a; b) and apical (c) [19].

The last listed alteration entails a distortion of the octahedron itself by elongation or compression and it is mainly caused by orbital interactions between B cations and the surrounding X anions, generally linked to the Jahn-Teller effect [9]. Another trigger that may bring to BX_6 distortion is the disproportionation of B cations in the compound [16; 9].

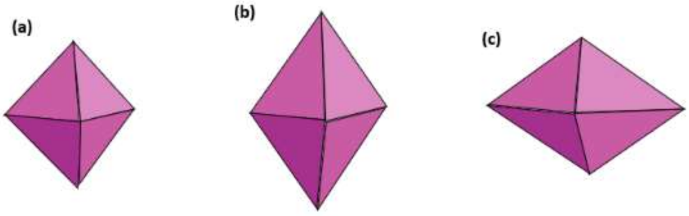

Figure 5. BX_6 octahedra distortion by elongation (b) and compression (c) along the same axis.

As introduced, the described variations are often the result of the Jahn-Teller effect, either the second or the first order one, even if such effect has only a partial influence on the distortions that modify the symmetry [20; 9; 15]. The Jahn-Teller effect is characteristic of non-linear complexes that present a degenerate electronic ground state asymmetrically occupied in its configuration. These kinds of molecules undergo a distortion aimed at removing the degeneracy and reduce the overall energy [18; 21]. The phenomenon can be observed both with the AMX_3 and the $A_2BB'X_6$ perovskite structures, provided that they contain an ion apt at giving Jahn-Teller effect, such as Cu^{2+} and Mn^{3+}. However, the magnitude and orientation of the Jahn-Teller effect depends on the anions and cations involved and is somehow influenced by local cation order and by octahedral tilting [18].

All the mentioned changes can result in a change of symmetry and in the loss of some of the elements of the space groups, with the consequent formation of trigonal, rhombohedral or orthorhombic perovskites [22]. For example, the following image (Figure 6) illustrates the distortion of a cubic structure to an orthorhombic one by octahedra tilting.

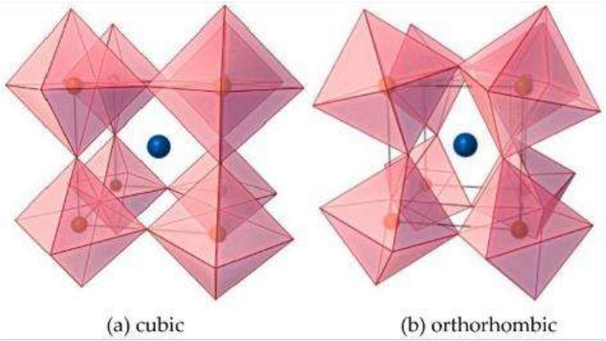

Figure 6. Representation of the distortion from a cubic (a) to an orthorhombic (b) structure [22].

2.1.3 Other perovskites structures

It is possible to detect architectures that differ from the ones described, where the compounds contain, for instance, chemical defects (vacancies in the A and B sites) or specific mixtures of A, B and X ions. For instance, some perovskites may present two or more type of cations in the A-site, in the B-site or in both [16; 9; 7]. These materials are not described by the conventional perovskite's formula ABX_3 as can be deduced by the following examples. Some double perovskites present a B-site cation substitution that leads to structures where the B site is doubly occupied; they are characterized by the formula $A_2(BB')X_6$ [9; 7]. Some examples of this particular structure are $Cs_2AgInCl_6$, $Cs_2AgBiBr_6$ and K_2NaAlF_6 [7]. In Figure 7 the structure is represented. Depending on the mutual arrangement of B and B' cations this same structure can result in many different varieties such as the rock-salt type, where B and B' are organized in a chessboard pattern, or a setup where BX_6 and $B'X_6$ are placed on parallel sheets with a precise disposition into the main perovskite cell [6; 9].

Another type of double perovskites similar to the ones that were just described are the ones that include in the B-sites (or in the A-sites) two cations of the same element, but with a different charge (for instance, monovalent and trivalent cations) [16, 7]. This last double perovskite structure is shown in Figure 7.

Sometimes it is also possible that the B' cation of the typical $A_2(BB')X_6$ double perovskite structure is substituted with the same A cation present in the other cationic sites. In this case, the formula describing the composition is A_3BX_6 and an example is Na_3AlF_6 [7]. This structure is also reported in Figure 7.

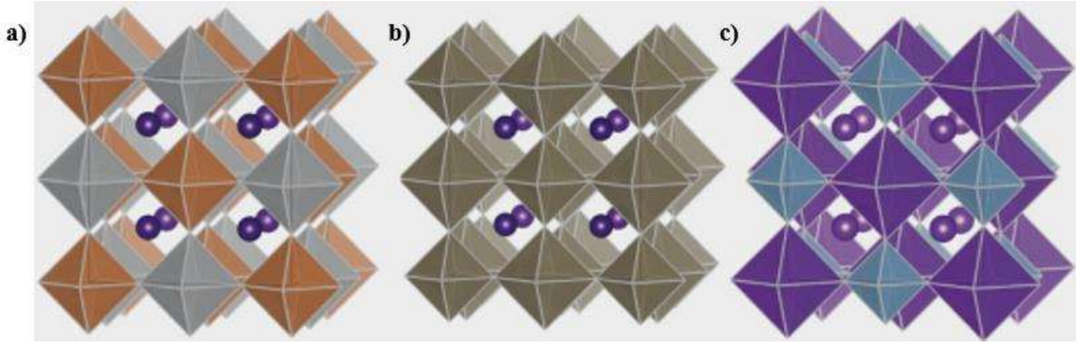

Figure 7. The typical $A_2BB'X_6$ structure (a), the $A_2B(I)B(III)X_6$ structure (b) and the A_3BX_6 structure (c) are reported [7].

While halide perovskites can only present these cation modifications on the B-sites, oxide perovskites can present them in both cationic sites, forming quadruple perovskites, defined by the main formula $AA'BB'O_6$ [15; 7]. Since they are not the main focus of this thesis, these structures will not be further discussed.

Beside the cases that have just been described, compounds that lack ions in the A-sites, B-sites or in the X-sites are also considered perovskite-like materials and, as the previous modified structures, they too present different formulas compared to the conventional ones [16; 9; 7]. The main difference between double perovskites and perovskites containing site vacancies is that the first are stoichiometric compounds, while the latter are often non-stoichiometric [16; 15]. When the B cation is in the oxidation state 4+, some B-sites can be substituted by vacancies, resulting in the formation of $A_2B[V]X_6$ structures. For instance, Cs_2SnI_6 and Cs_2PbBr_6 belong to this group of ordered perovskites [7]. This structure is shown in Figure 8.

Alternatively, if the B cation has an oxidation state of 3+, perovskites assume the formula $A_3B_2[V]X_9$ because the ratio between the cations and the vacancies is not 1:1 but 2:1 [7]. This structure is reported in Figure 8.

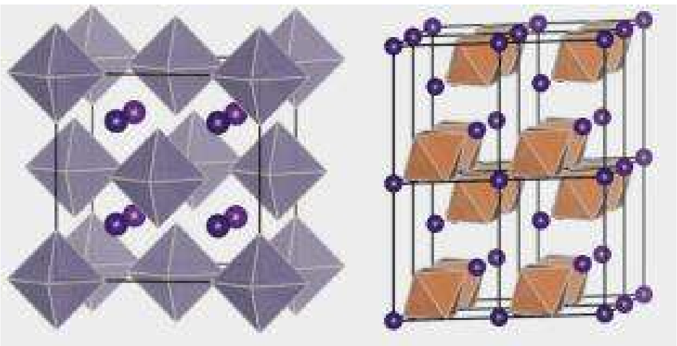

Figure 8. On the left the $A_2B[V]X_6$ structure is represented, while on the right the $A_3B_2[V]X_9$ structure is reported [7].

2.1.4 Related structures

Some other structures containing the main components of halide perovskites (monovalent A cation, bivalent B cation and halide anion) can be observed, but they fall into the nonperovskite metal halide group [7]. Cs_4PbBr_6 and Cs_4SnBr_6 fall into this category and so do the other structures described by the general formula A_4BX_6, which are usually defined 0D perovskites [23; 7; 5]. These particular materials are made up of disconnected BX_6 octahedra and their A cations occupy two distinct crystallographic sites [23; 3; 7].

The second type of compounds that can be considered in the nonperovskite category are the so called 2D perovskites, characterized by the formula AB_2X_5. Once again, the main example falling into this class of compounds is a lead halide perovskite ($CsPb_2Br_5$) [7]. The structure is not assimilable to the one observed in conventional perovskites because it does not include BX_6 octahedra, but instead contains the hendecahedral units $[PbBr_8]^{6-}$ [24]. The described structures can be observed in Figure 9.

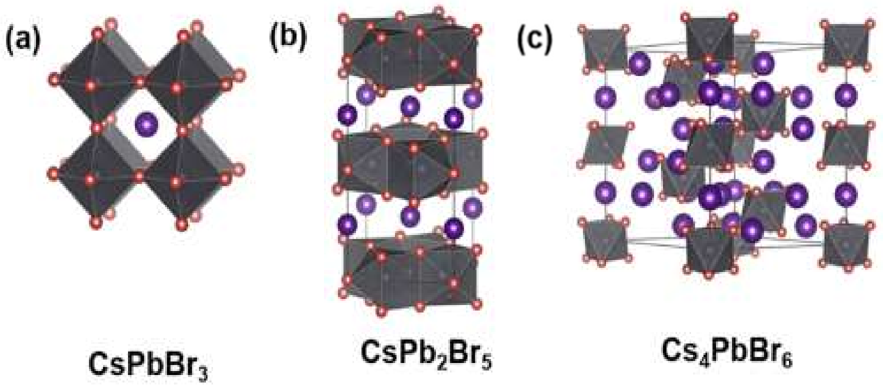

Figure 9. The classical perovskite structure (a) is represented along with the nonperovskite structures AB_2X_5 *(b) and* A_4BX_6 *(c). The picture has been modified from [25].*

Some other nonperovskite structures can be formed with heavy metals such as bismuth and antimony. They assume the $A_3B_2X_9$ composition and they comprise caesium-separated dimers (or other large cations, such as methylammonium and formamidinium, can be included in the A site). Said dimers are composed by face sharing BX_6 octahedra and the final structure is a hexagonal 0D ternary metal halide. The main examples of this structure are $Cs_3Bi_2I_9$, $MA_3Bi_2I_9$ and $FA_3Bi_2I_9$ [7]. This structure is represented in Figure 10.

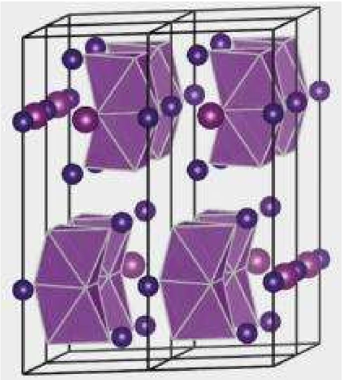

Figure 10. Representation of the $A_3B_2X_9$ non perovskite structure [7].

2.2 Nanoperovskites characteristics

The reduced size of perovskite nanocrystals brings out optical and electric properties that are not usually present in conventional perovskites and that depend on the size and shape of the nanocrystals themselves. Such differences are mainly due to the quantum confinement effect [26; 5]. For instance, bulk perovskites show some limitations when it comes to photoluminescence quantum yields (PLQYs) due to small exciton binding energies and to mobile ionic defects. In contrast, perovskite nanocrystals introduce the chance to boost the PLQY and to tune the emission by accessing quantum confinement size regime [3; 5; 11].

Another difference between bulk perovskites and nanoperovskites lies in their surface free energy, which results higher in the second kind of materials due to their smaller sizes. This generally leads to less lattice strain and consequently less octahedral tilting; this explains, for example, the presence of multiple phases when bigger particles are involved and of only the cubic one with smaller particles [27; 19; 11]. Beside this characteristic, surface chemistry is an important topic to investigate when it comes to perovskite nanocrystals, since it is related to their stability and it often influences their optoelectronic properties. For example, it has been shown that anion-related vacancies, which constitute structural defects, may alter phase transition's temperatures and the structure itself [28; 19]. The degree of knowledge on the type of defects that affect the structure and the mechanisms they follow is still limited, but it is clear that nanoperovskites are without doubt more defect-tolerant with respect to the conventionally-sized perovskites [23; 26; 4].

This chapter will briefly introduce the optical properties of perovskite nanocrystals, since the characterization of the compounds prepared in this work will be focused on the relationship between emission and the observed structure. After that, the peculiar defect tolerance of lead halide perovskite nanocrystals will be examined, in order to explain where this particular characteristic is originated from. Then, this chapter will contain a paragraph detailing surface chemistry, paying special attention to capping ligands and how their interaction with the surface may influence the stability of nanocrystals. Lastly, a general overview of their stability and, specifically, how it is linked to their structure and interface and how it is influenced by environmental factors will be provided.

2.2.1 Optical Properties

Lead halide perovskites will be the main focus of the experimental section of this thesis, so the following information will be mostly referred to this class of perovskites and, more in general, to metal halide perovskites. These compounds are particularly interesting because of their remarkable optical properties. They present high photoluminescence quantum yields, narrow full width at half-maximum (high colour purity) and a tunable photoluminescence which extends from the ultraviolet region to the near-infrared one. The aforementioned photoluminescence tuning can be achieved through size control, quantum confinement and compositional mixing [29; 3; 11].

2.2.1.1 Compositional mixing

Compositional mixing includes the modification of the halide constituents and this can be obtained by chemically managing the composition during the synthesis or by applying an anion exchange reaction as a post-synthetic process [3; 5]. As is shown in Figure 11, the substitution of an anion with another anion characterized by a bigger size leads to a red shift [11].

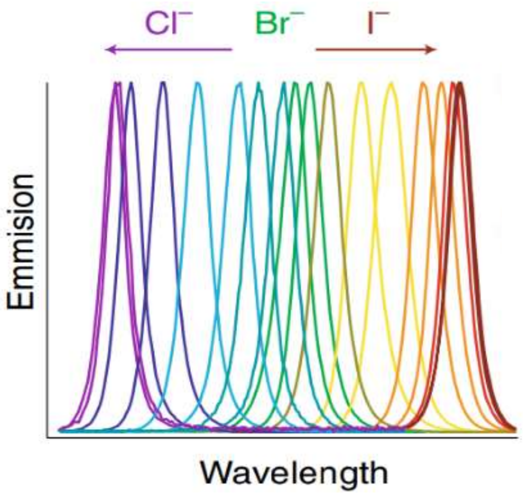

Figure 11. Photoluminescence tunability by anion substitution [23].

It is possible to change completely the anion present in the structure or to compose a material including more than one type of halide ion [30; 26; 11]. This second alteration gives rise to mixed halide perovskites, which allow to obtain the intermediate photoluminescence wavelengths [11]. However, they present some stability issues related to the fact that halide migration may happen and lead to phase segregation and formation of traps or domains of different pure halides. Then again, ionic migration can be lessened when using perovskite nanostructures, since the phenomenon happens mainly through grain boundaries, which can be reduced with a size reduction of the crystal [30; 26]. In order to tune the photoluminescence, the B cations' composition can also be adjusted by substituting completely the already present cation or by introducing a second cation and operating only a partial substitution [26]. The influence on the band gap of the X and B ions is understandable considering that the main contributors to the valence band maximum and the conduction band minimum are the σ antibonding orbitals and the π antibonding orbitals respectively, obtained by the combination of the B cation and the halide orbitals [31; 26]. A representation of the molecular orbitals involved in the formation of the valence and the conduction bands is shown in Figure 12.

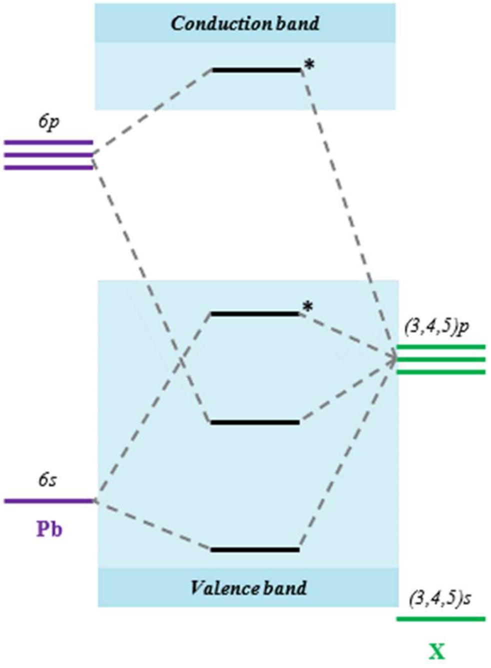

Figure 12. The molecular orbitals that form the conduction and the valence bands. The stars in the picture denote the antibonding orbitals.

Beside the obvious influence of the B and X ions on the band gap, the A cation can also modify said separation. Some works link this influence of the A cation on the photoluminescence to the fact that said cation interacts with the octahedral structure and the alteration of such bonding ends up changing the ionic/covalent character of the Pb-X bond too [26]. Some other works state that the band gap depends on the changing of A cations because a reduction in this size induces a distortion of the cubic structure and the consequent tilting of the angle of Pb-X-Pb bonds [11]

2.2.1.2 Quantum confinement effect

When it comes to size and shape, low dimensional perovskites and nanoplatelets are particularly characteristic. Their light emission can be tuned by changing the cited features and these compounds are generally stable and characterized by optimal PLQYs. These low-dimensional nanocrystals have been cited as an example to show how the improvement of the optical properties in perovskites is mostly linked to quantum confinement effect. This phenomenon gains importance when at least one of the physical dimensions is similar or smaller than the Bohr exciton radius of the material, a parameter that indicates *"the most probable delocalisation distance of an exciton in the bulk semiconductor"* [11]. Usually, the quantum confinement effect is not particularly important for $CsPbBr_3$ nanocrystals because their dimensions are not much smaller than the Bohr radius. Consequently, as can be observed in Figure 13, the phenomenon can be observed, but it will not be strong since the degree at which it presents is dependent on the degree of the confinement [31].

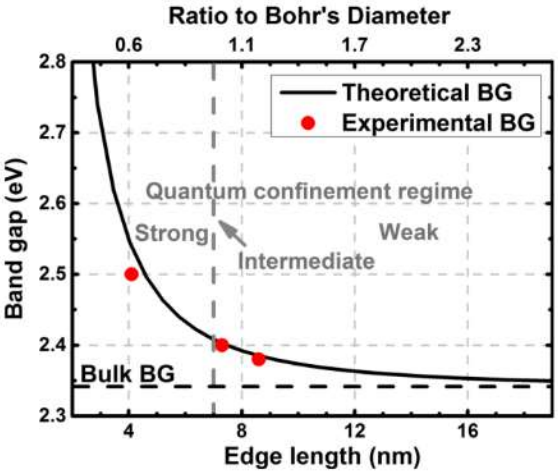

Figure 13. Relation between the degree of quantum confinement effect and the dimensions of the considered particles [31].

In general, quantum confinement deals with the restriction of electron wave functions and the following modification of the electrons' energy levels, which in the end do not appear continuous, but discrete [32]. The confinement effect can produce discrete states when the particles' sizes are smaller than the Bohr radius. It usually leads to intermediate bands which are not neither single bands nor molecular-like states when the dimensions are larger than the Bohr radius [31].

The consequences of quantum confinement effect on perovskite nanocrystals are evident in the position of the absorption peaks. A shift in the resultant emission peak can be in fact observed when the confinement energy increases and, more precisely, they tend to blue-shift when the size of the particles is reduced (Figure 14) [31; 26; 11].

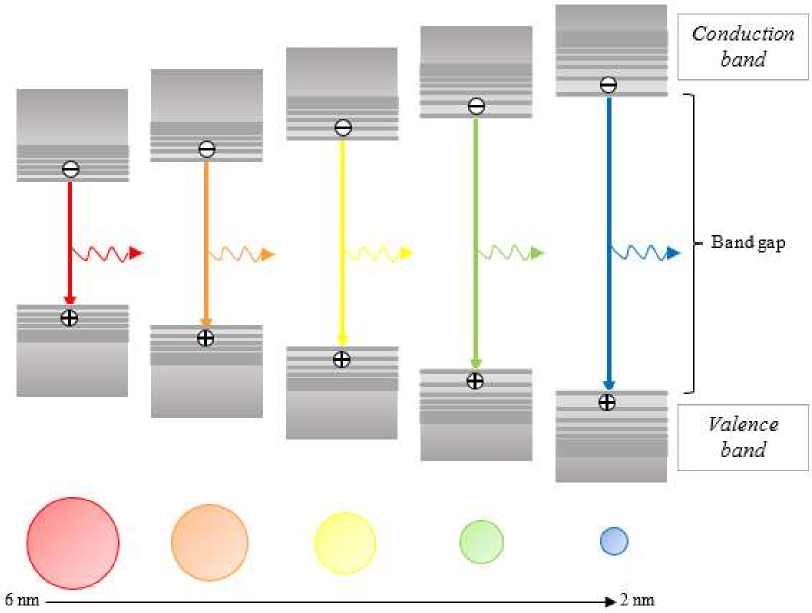

Figure 14. Effect of the quantum confinement effect on the band gap of lead halide perovskite nanocrystals.

The two-dimensional perovskites cited in this paragraph, together with nanowires and nanosheets, are a unique case, in the sense that they usually present a higher degree of quantum confinement effect compared to 3D perovskites. This can be obtained by containing the size of the nanocrystal along a specific direction through the use of long chain ligands [11].

2.2.1.3 Surface defects

The last factor that affects perovskite nanocrystals' optical properties is the presence of surface defects. In particular, this last parameter explains why it is so important to make sure the materials undergo post-synthetic treatments to saturate vacancies at the surface or to modify the distribution of the capping ligands, aiming at improving parameters such as the PLQY. As a case in point, one of the main factors that leads to a lower PLQY is an incomplete surface passivation since it gives rise to charge trapping and nonradiative recombination which are responsible for energetic losses [33; 34]. Figure 15 shows the two distinct cases where the surface is or is not passivated.

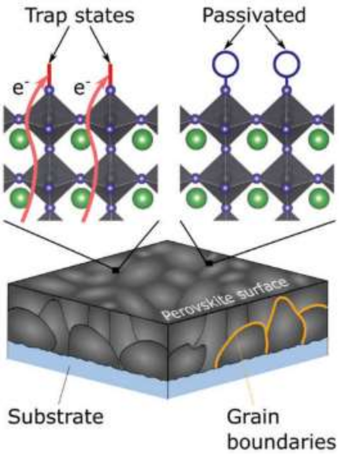

Figure 15. On the top left the situation where the surface present trap states is represented, while on the top right the situation where the surface is passivated is shown [35]. In the picture: A cations = green spheres; B cations = black spheres; X anions = blue spheres.

Charge trapping may happen when an atom in the periodic structure is not located in its designed site, since this leads to the formation of defects and of intermediate electronic states where charges can get trapped. To regain their mobility in the structure an additional energy barrier needs to be overcome and this can be obtained through thermal energy absorption or optical excitation. These new electronic states linked to the rise of defects are problematic when their energy is in-between the conduction and the valence bands' energies. The traps located in the band gap can be divided into shallow and deep traps; shallow traps have energies that differ only slightly from the respective conduction or valence band's energy, while deep traps are generally positioned in the middle of the band gap and may lead to non-radiative recombination [35]. A schematic illustration of the different type of traps is represented in Figure 16.

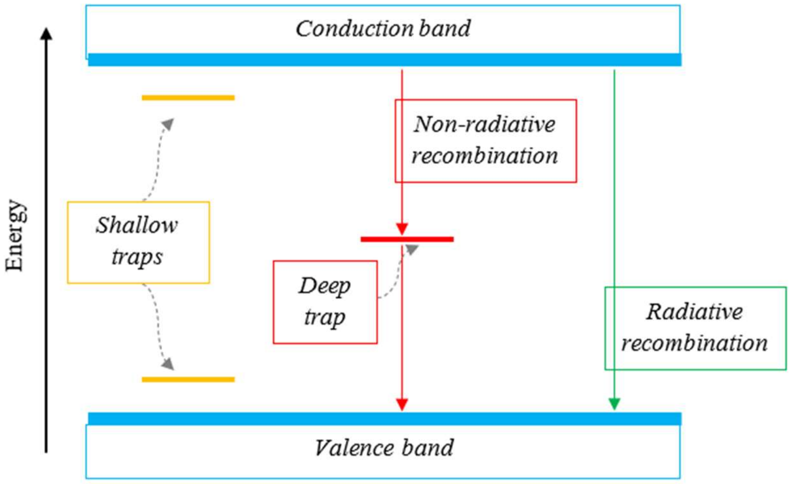

Figure 16. Representation of the two different kind of trap states.

Lead bromide and lead iodide perovskites follow the description that has just been delineated, meaning that they present shallow traps due to the presence of halide vacancies on the surface. On the other hand, some calculations have shown that halide vacancies in lead chloride perovskites lead to the formation of deep traps and these midgap levels are highly localized on the lead atom that remains uncoordinated [33; 36; 34]. This theorical calculation can be explained considering that the lattice parameter decreases when modifying the halide ion in the order I – Br – Cl. As a consequence, lead(II) dangling bonds, formed due to halide vacancies, present stronger interactions. Such interactions paired to low electron affinity are the cause of deeper trap levels in lead chloride perovskites [34]. This formation of deep trap levels is also the reason why nonradiative recombination is so significant in $CsPbCl_3$ nanocrystals, compared to $CsPbBr_3$ and $CsPbI_3$, where neither electrons nor holes are strongly localized [33]. In Figure 17, the relation between the PLQY and the halide vacancies' density is shown for the three different halides. In the picture the nanocrystal concentration is also reported and its trend is inverse to the one observed for halide vacancies because of the weak binding of oleylammonium halide as a capping ligand [33].

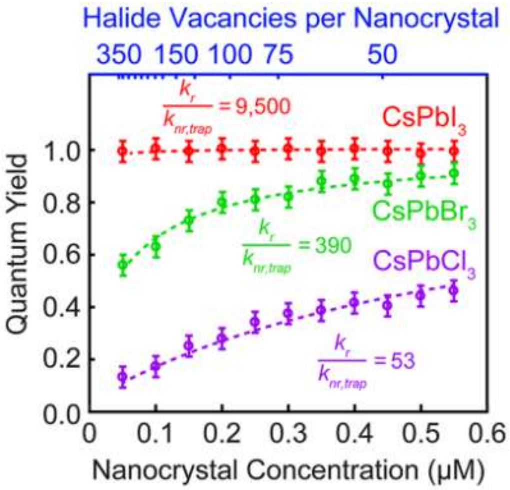

Figure 17. Dependence of the PLQY from the concentration of halide vacancies in a perovskite phase. The representation reports a comparison between $CsPbCl_3$, $CsPbBr_3$ and $CsPbI_3$ [33].

2.2.1.4 Defect tolerance

Defect tolerance is one of the characteristics of perovskite nanocrystals which make these materials particularly interesting in optoelectronic applications [17; 23; 35; 34]. It describes the ability of these materials of retaining their electronic structure even if they contain a high concentration of defects [11].

Defects can be distinguished into two categories depending on their characteristics and some of these are schematically represented in Figure 18. Intrinsic defects are internal to the structure and involve a specific lattice site, while extrinsic ones are linked to the environment or to unsaturated surface bonds [35]. The first category can be furtherly divided into point defects (vacancies, interstitial defects and anti-site defects) and extended/structural defects (dislocations) [34]. However, these are not particularly significant, since the extrinsic type of imperfections are the most relevant in lead halide perovskites [35].

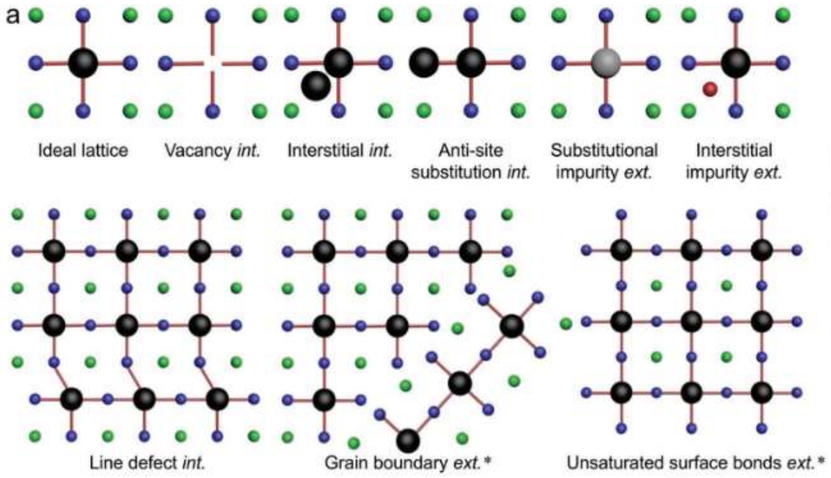

Figure 18. Type of defects that may be found in lead halide perovskites [35]. In the picture: A cations = green spheres; B cations = black spheres; X anions = blue spheres.

Lead halide perovskite nanocrystals present plentiful defects due to their low formation energies and to their inherently high specific surface, but these do not pose a problem [17; 35]. The only issue that may arise in lead halide perovskites is in fact the formation of X-site vacancies, since interstitial and anti-site defects and B-site vacancies are highly unlikely [23; 4, 11]. Indeed, vacancies have a low formation energy and they end up forming shallower traps, while interstitial and anti-site defects would form deeper traps, but they would require the misplacement of ions in the perovskite lattice and this is energetically difficult [23; 35]. So, as explained, halide vacancies are not as compromising in perovskites compared to other nanocrystals because the following defects end up in-band (in particular in the valence band) or as shallow trap states [4; 35; 11]. This is a consequence of the position of the band gap with respect to the atomic orbitals, in this type of nanocrystals. Both the conduction and the valence band form from antibonding orbitals and the original atomic orbitals result closer to the bands' edges rather than in the middle of the band gap. Consequently, since to a first approximation defect states form close to the original atomic orbitals, the states formed from the vacancies reside in-band instead of between bonding and antibonding states as in conventional semiconductors [17; 23; 26; 34]. This is better illustrated in Figure 19, where lead halide perovskites are compared to conventional semiconductors.

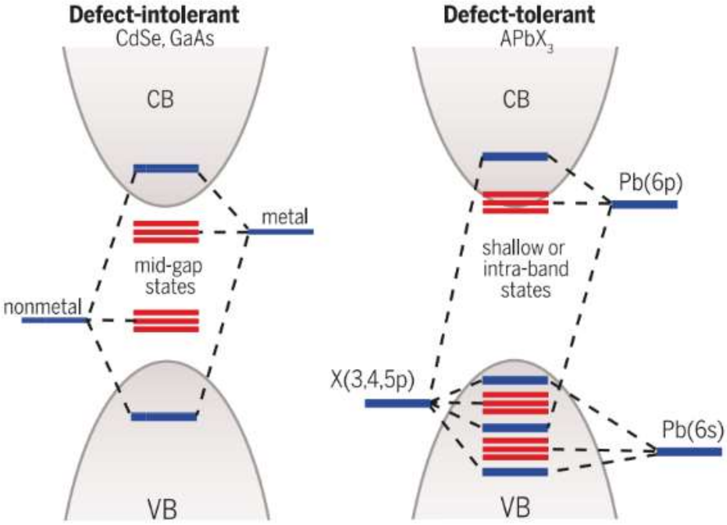

Figure 19. Comparison between the consequence of defects in the electronic structures of conventional semiconductors (left) and lead halide perovskite nanocrystals (right) [17].

This explains why, despite surface passivation being quite important to achieve optimal properties, the dissociation of ligands from the surface is not that much of an issue when working with lead halide perovskites [4].

2.2.2 Surface chemistry

Surface chemistry is particularly important when working with nanocrystals because the fraction of surface atoms can be quite high and incomplete coordination of these atoms can lead to nonradiative recombination thanks to the formation of defect energy levels [5]. Halide vacancies are one of the main contributors to said nonradiative recombination, so passivation is usually applied to nanocrystals, when aiming at reaching the highest values possible of PLQY [33; 5]. It is especially important to obtain trap-free nanocrystals when these materials have to be used for optoelectronic applications since, in that case, they need to possess a series of characteristics to guarantee satisfying performances (tunable band gaps, high luminescence efficiencies, excellent photostability and strong light absorption and emission) [33]. In order to passivate the halide vacancies on the surface, it is possible to use a post-synthetic or an *in situ* passivation approach. The post-synthetic passivation is often used, but it may bring impurities into the material, which will consequently require further purification and this presents a problem since perovskite nanocrystals have a tendency to deteriorate under repeated washings with solvent-antisolvent methods. The *in situ* passivation is obtained through the stoichiometric control of the reaction, the use of appropriate capping ligands or the optimization of the precursors and it allows to avoid a second purification stage [5].

This chapter will focus on the utilization of capping ligands since this is the most used type of surface passivation that can be seen in lead halide perovskite nanocrystals. The use of capping ligands has effects on both the kinetics of nanocrystals' formation (it affects the crystal growth) and on their morphologies, determining the final size and shape of the material [3; 5; 11]. Moreover, passivation can avoid or limit crystal agglomeration and influence the crystals' solubility; for example, the hydrocarbon tails of some ligands enable the dispersion in organic solvents of the crystals they are associated to [4; 5; 11].

This passivation strategy requires an accurate choice of ligands so to conserve the nanocrystals' characteristics; for example, nanocrystals whose main use is in optoelectronic devices need ligands characterized by specific electrical conductivities [4; 5]. Depending on the kind of ligands capped to the surface, different binding methods may be observed; the so-called X-type ligands generally form covalent bonds due to their tendency to share one electron each with the perovskite cations, while L-type ligands donate two electrons toward the metal centre, bringing to the formation of a dative covalent bond. There is also a third ligand type, the Z- one, which is less common than the others and has the ability to accept an electron pair to form a dative covalent bonding with perovskite anions. While L-type ligands can be seen as Lewis bases with an orbital filled with two electrons, Z-type ligands are Lewis acids that can accept electrons in an empty orbital. This schematic division follows Green's Covalent Bond Classification (CBC) and it is represented in the following picture (Figure 20) [37; 33; 5; 11; 1].

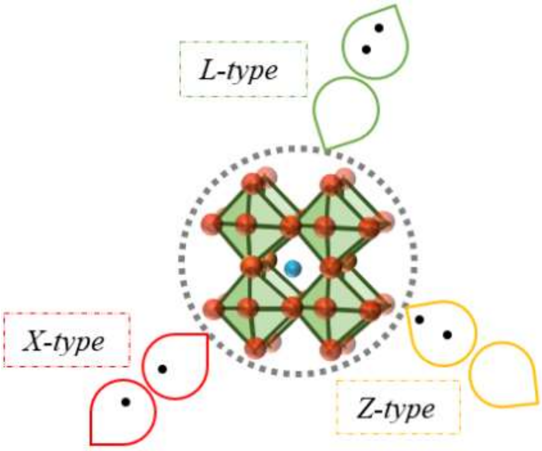

Figure 20. The main type of capping ligands for nanocrystals, according to Green's Covalent Bond Classification.

The main obstacle in surface passivation by capping is the dynamicity of the bond between the surface itself and the ligand, which has been proved to lead to instability and consequent degradation of the materials' optical properties and, at times, of their structure [37; 3; 4; 5]. As a matter of fact, if ligands are not bonded strongly enough to the surface, they might dissociate from the nanocrystal during the isolation or purification processes, which are generally conducted through multiple precipitation–redispersion steps [23; 4; 5]. This concept is represented in Figure 21.

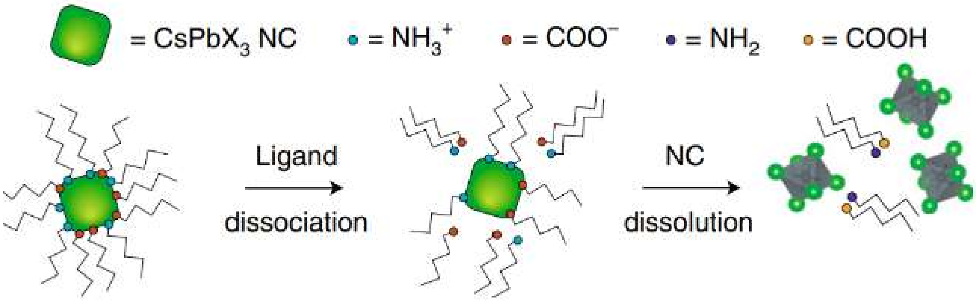

Figure 21. Description of the dissociation of the weakly bound ligands and of the consequent dissolution of the nanocrystals [23].

The instability of the interaction of ligands with the surface can be linked to the ionic nature of these nanomaterials [37; 3]. Moreover, the aforementioned instability is a consequence of the quick proton transfer that occurs between acid/base pairs such as amine/ammonium and carboxylic acid/carboxylate [4]. As a consequence of these processes, the surface of the nanocrystals is acidic due to the protons (formed from the deprotonation of the ammonium) and the unwashed Lewis acids present on the surface itself. This acidic environment acts as a catalyst for the formation of amides as the condensation products between carboxylic acids and amines [11]. In the following picture (Figure 22) the process is illustrated.

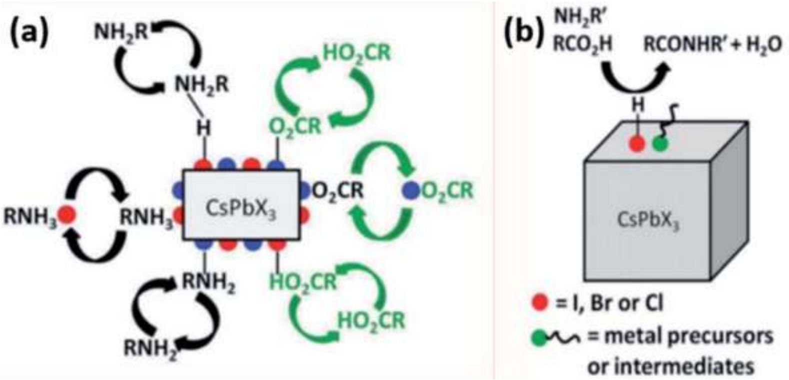

Figure 22. On the left (a) the exchange processes that happen on the surface of the nanocrystals are represented. On the right (b), the formation of amides is illustrated [11].

2.2.2.1 Conventional ligands

Generally speaking, long-chain organic acids and bases are chosen as capping ligands in all-inorganic perovskite nanocrystals' synthesis as both of them have been proven necessary to stabilize the crystals [2; 1]. The amines used as base ligands are fundamental to control the crystallisation process and are apparently more important to obtain high PLQYs [37; 11]. On the other hand, carboxylic acids are more important to avoid the aggregation of nanocrystals in the solution [11]. In the following picture (Figure 23) a representation of surface passivation is reported. Cationic ligands such as ammonium ions substitute caesium cations on the surface, while Lewis bases (e.g., ionic halide sources), neutral molecule and X-type ligands position themselves into halide vacancies and coordinate to lead cations [33].

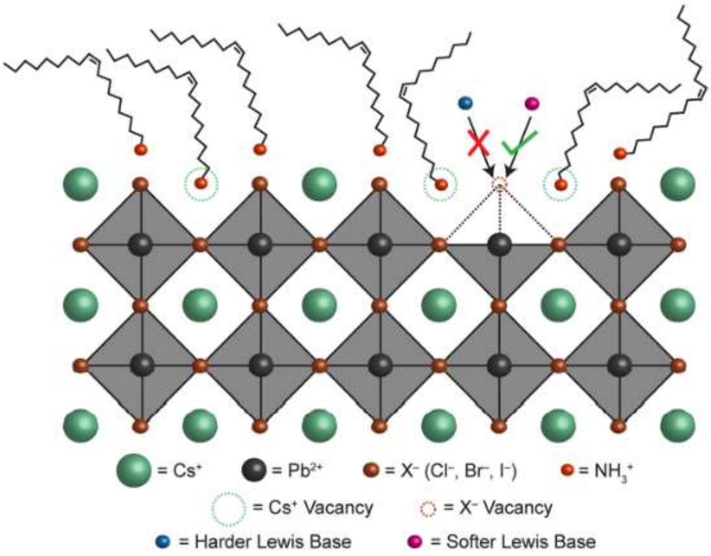

Figure 23. Schematic representation of surface passivation in caesium lead halide perovskites [33].

Oleic acid ($C_{18}H_{34}O_2$) and oleylamine ($C_{18}H_{35}NH_2$) are the most used long-chain ligands and they bond to the surface as oleylammonium bromide or oleylammonium carboxylate, which are X-type ligands, and as unprotonated oleylamine, which is an L-type ligand [37; 11]. It has been shown that oleate ions often do not bind the surface. This can be explained considering that lead is a soft cation, while carboxylates are hard anions, so their interaction is not favourable [33]. In Figure 24 the conventional amine/carboxylic acid combination is used to saturate the surface. For instance, oleylamine can react with hydrobromic acid to form oleylammonium bromide and with the oleic acid, leading to the latter's deprotonation and to the formation of oleylammonium oleate [37].

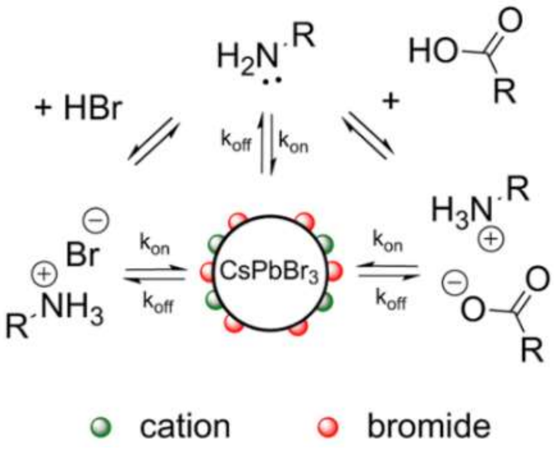

Figure 24. Dynamic acid/base equilibria which happens on the surface of the nanocrystals between the amine, carboxylic acid and hydrobromic acid [37].

This leads to surfaces passivated by carboxylate and alkylammonium ligands, which can detach quite easily during the purification stage, as already outlined [2; 1]. In particular, it has been shown that ammonium cations are bounded less strongly to the surface compared to carboxylate, and the firsts tend to dissociate from the surface during purification methods where more polar solvents are used [2; 11; 1]. These different stabilities can be explained considering that these two ligand types are differently bonded to the surface. While carboxylates interact with surface lead atoms in a metal-ligand coordination, alkylammonium establishes a pseudo-hydrogen bond with the surface halide anions. The latter, $[Br \sim H - N^+]$, results weaker than the first and tends to weaken even more in a polar solvent, explaining why alkylammonium ligands detach more easily from the surface [2; 5].

It is important to highlight the fact that, while the coordination of amines to the surface has been discussed in detail, the coordination of carboxylic acids is still debated. Some articles report that the carboxylate group does not bind to the surface and only interacts with the cationic ligands, while some others report that a coordination of the carboxylic acid can happen when an excess of oleylammine is added (in this case, the capped ligand is oleylammonium oleate) [37; 33; 34]. These two points of view have been described into this paragraph. A third possibility has also been suggested: the carboxylic acid molecules might substitute the halides on the surface, completing the coordination of lead and passivating the defect states [34]. This third hypothesis is shown in Figure 25. This picture also includes the coordination of the discussed ammonium salts on the surface and shows some other types of ligands that will be discussed in the following paragraph.

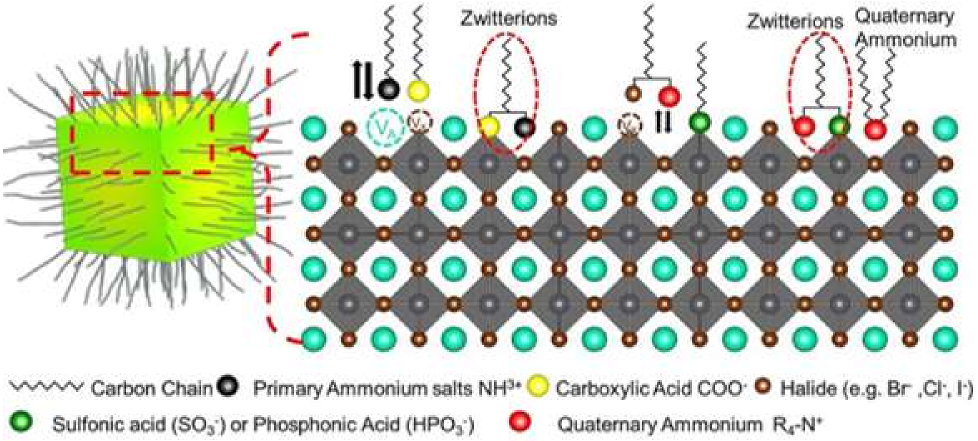

Figure 25. Schematic representation of surface passivation in caesium lead halide perovskites [34].

2.2.2.2 Alternative ligands

To achieve a more stable surface-ligands interaction, ligands possessing more than one anchoring group are a good alternative. For examples, zwitterionic compounds with both quaternary ammonium cations and anionic portions (such as carboxylate, sulphonate or phosphonate groups) are ideal to create a more stable structure [23; 34]. This species can bind both the cationic and anionic sites at the same time, resulting in a bidentate or multidentate coordination, and this allows to use a smaller amount of ligands to obtain a single monolayer on the surface instead of needing an excess as tends to happen with conventional ligands [37]. Figure 26 shows how zwitterionic species are more tightly bound to the surface with respect to the conventional ligands.

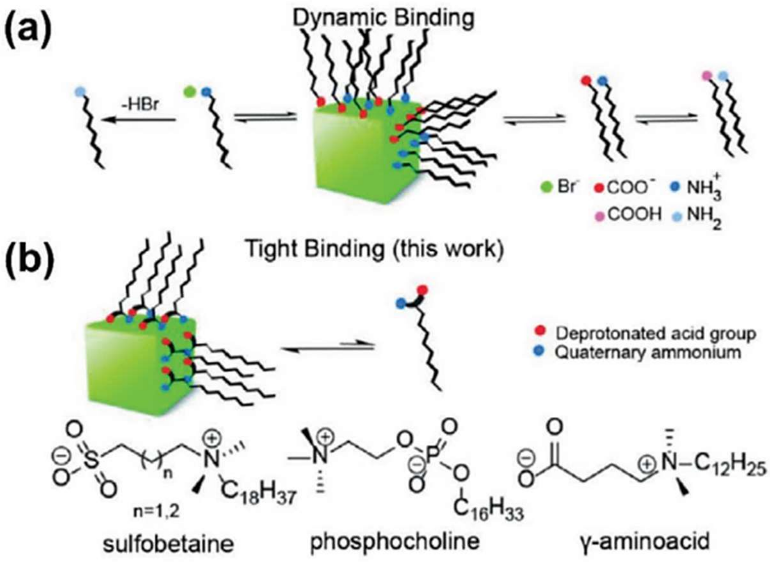

Figure 26. Schematic comparison between conventional amine-carboxylic acid binding and the zwitterionic species binding to the surface of the nanocrystals [4].

Beside this type of ligands, some alternatives to the conventional ones have been explored. Quaternary ammonium halides can be considered as the better version of the conventional primary amines; they possess the same binding functionality, but the formers do not participate in proton exchange. These capping ligands bind both to the anionic and the lead sites with the ammonium cations and the halide anions respectively. Better alternatives to carboxylic acids can be found too. Specifically, the instability of the interaction between the conventional carboxylic acids and the surface is generally attributed to an incompatibility in the hard/soft character of the ligands and the lead cations involved. This can be solved by using ligands presenting electron-withdrawing substituents, as aromatic or fluorinated aliphatic groups. Other options to conventional carboxylic acids are phosphonic and sulfonic acids. The formers present a phosphonyl and two hydroxyl functions, so they can both bond on a lead site with an anionic extremity (one of the deprotonated hydroxyl groups) and form a hydrogen bond with the remaining portions (Figure 27). These hydrogen bonds are particularly important because they can establish between ligands, favouring nanocrystals' binding [4].

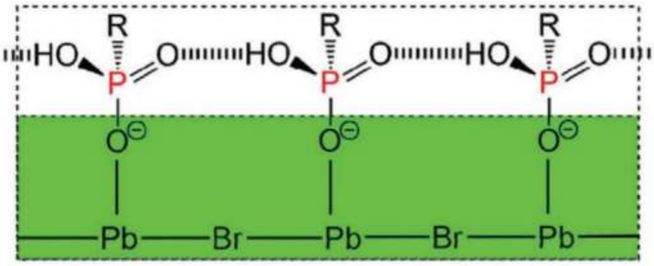

Figure 27. Interaction of phosphonic acids with the surface of lead halide perovskite nanocrystals [4].

On the other hand, sulfonic acids bind to the nanocrystals through the anionic portion of a sulfonate group and they can passivate the halide vacancies present on the surface [4].

2.2.3 Stability

As previously introduced, metal halide perovskite nanocrystals are particularly attractive because of their properties, which make them particularly useful in various optoelectronic applications. However, the main downside is their tendency to deteriorate due to their poor stability, which is influenced by intrinsic characteristics, related to their structures and interfaces, and by environmental factors such as light, heat and moisture [1]. Indeed, it has been shown that material stoichiometry, light exposure, temperature, moisture and pressure can lead to the formation of defects, which in turn may give rise to trap states [35]. As a result, it is necessary to apply some protection strategies to guarantee long term durability and the conservation of efficient performances [24; 1]. Generally speaking, both organic-inorganic and inorganic perovskites present some stability issues, but the firsts tend to be more problematic when it comes to both intrinsic and thermodynamic stability because the organic cations located in the A sites are volatile. Even when they are not subjected to external factors, organic-inorganic perovskites have a tendency to decompose into the binary halide compounds AX and BX_2, since such process has been shown to be exothermic and independent from the environmental agents. This tendency toward decomposition decreases once the organic A cations are substituted by Cs^+, for a variety of reasons. The caesium cation is spherical, so the system is symmetric and is not particularly influenced by entropic factors. Moreover, the structure of inorganic perovskites is more rigid, since they do not present the mobility of both A cations and halide anions [10].

2.2.3.1 Crystal structural stability

As described in Paragraph 2.1.2, the main symmetrical cubic structure of perovskites may undergo some distortions which render the structure orthorhombic or tetragonal. Such distortions are often connected with the ions' radii, which also influence the crystal structural stability. Two main parameters can be used to evaluate a structure's stability [3; 11; 1]:

- the Goldschmidt's tolerance factor → $t = \frac{r_A + r_X}{\sqrt{2}(r_B + r_X)}$;
- the octahedral factor → $\mu = \frac{r_B}{r_X}$.

(Where r_A, r_B and r_X are the radius of A, B and X respectively)

The octahedral factor defines the stability of the BX_6 octahedra [3]. In particular, it states that a perovskite structure is stable once the calculated value varies in the range 0,41 – 0,89 [3; 10; 11]. For example, this parameter rationalizes the fact that the tetrahedral coordination is favoured over the octahedral one if small cations are coordinated to large anions [7]. On the other hand, the Goldschmidt parameter defines the fitting of monovalent A cations in the spaces present between the BX_6 octahedra [24; 7]. Depending on the dimensions of the A cation, the structure can be more or less stable. Accordingly, caesium(I), methylammonium and formamidinium can be readily included in the structure, while sodium, potassium and rubidium cations are too small and imidazolium, ethylamonium and guanidinium are too large (Figure 28) [3].

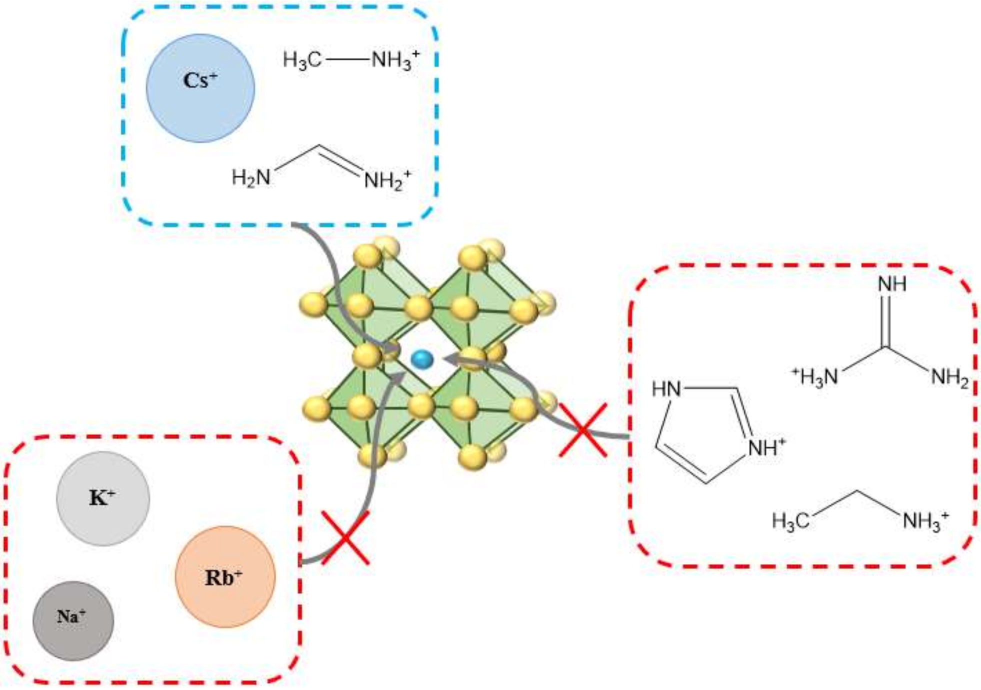

Figure 28. Schematic representation of the cations that can and cannot be included in the A-sites of lead halide perovskites.

When the Goldschmidt's tolerance factor is close to 1, the structure tends to be perfectly cubic, while when such value differs greatly from this number, the structure is either orthorhombic or tetragonal because the octahedra are partially tilted [11]. At times, in order to reach the ideal value of this tolerance factor (meaning the structure is perfectly cubic) a mixture of different monovalent A cations can be used. This leads to more stable structures, but it generally modifies some optoelectronic properties and the final shape of the nanocrystals [1]. The incorporation of different A cations in the structure could also lead to phase segregation if the cations inserted in the structure do not have similar sizes to the A cations already present. This constitutes a limit for all-inorganic perovskites, because caesium is the biggest nonradioactive element of Group 1, so it is difficult to find a different appropriate cation to add in the structure. Alternatively, in order to improve the tolerance factor, some of the anions in the structure may be substituted with different ones to form mixed lead halide perovskites. However, this leads to a variation in the optical properties and, sometimes, to phase segregation [10].

The importance given to the stabilization of the cubic structure is mainly found in bulk perovskites, since nanocrystals present some differences concerning the crystal structural stability. Especially for perovskite nanocrystals, the large surface energy can stabilize the cubic phase, which can be maintained for months even when the compound is exposed to air [1].

2.2.3.2 Interface-induced stability

As remarked in Paragraph 2.2.2, the interaction between the surface and the capping ligands is highly dynamic and this leads to instability and consequent degradation of the materials' optical properties. In particular, it has been observed that ligands easily dissociate from the surface during the isolation and purification steps, leading to the deterioration of the structural integrity [17; 5; 1]. There are a series of strategies that can be carried out to stabilize the nanocrystals' surface. For instance, lead halide perovskites can be encapsulated in an inert shell or in a matrix as can be seen in the following picture (Figure 29) [23].

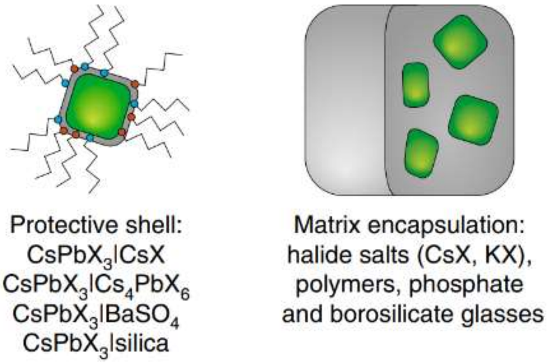

Figure 29. Representation of two distinct way to reduce interface-induced instability [23].

This protection strategy is useful to improve the nanocrystals' stabilization towards heat and environmental factors and can become a fundamental step in the production of optoelectronic devices. A similar protection route consists in the incorporation of the nanocrystals in a Cs_4PbBr_6 matrix, which is known to be more stable [23]. This encapsulation is a good alternative to the conventional production of core-shell structures, which present some difficulties for lead halide perovskites. Indeed, the latter tend to undergo a spontaneous anion-exchange reaction and this process may happen between the core and the shell, leading to the formation of mixed-halide perovskites [38; 39]. The reasons stated for the added stability of these materials are the lessening of the chance of aggregation of $CsPbBr_3$, the protection from moisture and water attributed to the Cs_4PbBr_6 matrix and the fact that the octahedra in a 0D structure (Cs_4PbBr_6) are isolated [39].

2.2.3.3 Environmental stability

Perovskite nanocrystals may deteriorate under the influence of a series of environmental factors: moisture, oxygen, temperature and light exposure [17; 24; 11; 1]. Since these materials are often used as light and photoelectric convertors, their instability to illumination and to heat is particularly problematic [24].

First of all, water has been shown to act as a degradation catalyst in perovskites structures and such influence is not strictly correlated to the duration of the exposure or to the amount of water. For example, a colour change has been observed in organic-inorganic perovskites under moisture exposure and a conversion between different phases has been illustrated for inorganic perovskites [1]. The decomposition of nanocrystals when exposed to water is linked to their ionic character and can happen even in the dark [40]. Water, and more generally polar solvents, can bring to a phase change since, when coming into contact with such mediums, the nanocrystals can experience the insertion or the removal of atoms. Specifically, the ejection of CsBr gives rise to $CsPb_2Br_5$ nanostructures, starting from $CsPbBr_3$ [41]. More generally, water molecules can remove CsBr from the material, leading to the transformation of Cs_4PbBr_6 in $CsPbBr_3$ and consequently of the latter into $CsPb_2Br_5$. This last conversion takes place alongside a change in the coordination number of Pb(II), which goes from six (in the $CsPbBr_3$ structure) to eight (in the $CsPb_2Br_5$) [42]. The mechanism involves the breaking of the bond between A cations (Cs^+) and the octahedra and the transformation of said octahedra into hendecahedral units ($[PbBr_8]^{6-}$) [24]. Accordingly, the original three-dimensional shape cannot be identified in the final two-dimensional structure [3]. The more water content interacts with the material and the more crystals will turn into $PbBr_2$ as the final product [24]. Figure 30 reports the phase change brought up by the aqueous ambient.

Figure 30. Phase transformation observed when the material is exposed to moisture [42].

The second of the cited factors is responsible for the “oxygen boost” effect, which consists in the increase of PL intensity under oxygen atmosphere due to the attenuation of the trap density (oxygen molecules can inactivate deep hole traps) [24; 1]. The mechanism (Equations 1, 2, 3) has been shown for organic-inorganic lead iodide perovskites. According to this mechanism, oxygen can be absorbed on the surface and diffuse in the structure to occupy halide vacancies; at this point, the O_2^- anion can form and lead to the decomposition into PbI_2, H_2O, I_2 and CH_3NH_2 [40].

$$MAPbI_3\ (+\ \text{light}) \rightarrow MAPbI_3^* \tag{1}$$

$$O_2 + MAPbI_3^* \rightarrow O_2^{*-} \tag{2}$$

$$O_2 + MAPbI_3^* \rightarrow CH_3NH_2 + PbI_2 + \tfrac{1}{2} I_2 + H_2O \tag{3}$$

During this process the electric structure is modified through the repairing of the trap states [24]. This effect is only temporary and, as shown, it finally results in a degradation mechanism, which can be associated to the nanocrystals' colour change [1]. In Figure 31 the process is illustrated to provide a better understanding.

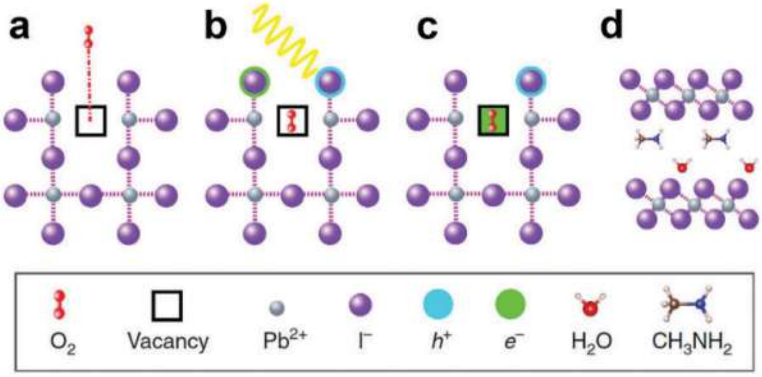

Figure 31. Representation of the degradation process that affects lead halide perovskites in the present of oxygen [40].

In this photo-oxidation mechanism light and oxygen interact at the same time with the material. This is particularly harmful for organic-inorganic perovskites, since the organic A cation (methylammonium) contains acid protons that are not present if the A cation is the inorganic caesium(I) [10]. The same mechanism cannot be unambiguously applied to inorganic perovskites and a specific decomposition route is still not defined and confirmed [40].

Light exposure by itself can affect perovskites' stability and it is more problematic than the first two because it cannot be avoided through an encapsulation process [1]. Nanocrystals are negatively affected by light exposure because it leads to the desorption of surface ligands and the consequent aggregation of adjacent crystals. Such aggregation is detrimental because it increases the number of trap states due to the absence of a part of the capping ligands [40]. The described process is schematically represented in Figure 32.

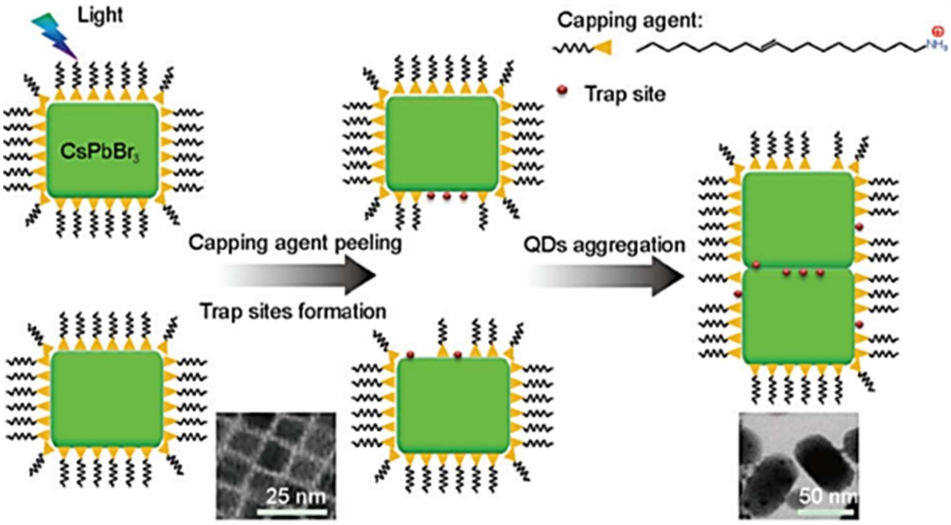

Figure 32. Representation of the influence of light exposure on perovskite lead halide perovskite nanocrystals [43].

Temperature can induce a degradation in perovskite materials, which might be attributed to the decomposition of the organic capping ligands [24; 1]. The influence of temperature on the nanocrystals can also accelerate the degradation originated due to moisture and oxygen [24; 40; 1]. Generally speaking, the influence of temperature on the deterioration differs between organic-inorganic and all-inorganic perovskites, with the latter being more stable [1]. Perovskite nanocrystals' decomposition at high temperature modifies irreversibly their optical properties, leading to a pronounced attenuation. The loss of luminescence may be attributed to aggregation and to the loss of capping ligands, which leads to defect formation [24]. Finally, an increase in the temperature can also facilitate the transformation from the 0D to the 3D structure through the removal of CsBr and then it can lead to the formation of the 2D structure starting from the three-dimensional one due to a decomposition process that starts from the desorption of the weakly bound ligands [3].

2.3 Synthetic routes

The interest in the synthesis of metal halide perovskite nanocrystals started to spread starting from 2011, when a TiO_2 matrix was used to produce nanocrystals by spin-coating the perovskite precursor solution [44; 5]. Following this first experience, in 2014 colloidal lead halide perovskite nanocrystals have been synthesized by solvent-induced reprecipitation, using specific capping ligands to control the crystallization process [45; 5]. Right after this, in 2015, lead halide nanocrystals have been obtained by a hot-injection technique and this was the first consistent step toward a shape-controlled synthesis, since it enabled to regulate nanocrystals' size by changing the temperature of the process

[46; 5]. Another relevant step in the shape-controlled synthesis field is the production of organic-inorganic hybrid perovskites nanoplatelets with thickness control down to a monolayer. This control over the shape was achieved by varying the ratio of long and short-chain ligands during the reprecipitation phase [47; 5].

Recently the synthesis of perovskite nanocrystals has been obtained mostly by the hot-injection (HI) approach and the ligand-assisted reprecipitation (LARP) technique, the latter of which has been introduced by Zhang in 2015 [48; 49; 5]. However, these are not the only methods available to synthesize metal halide nanoperovskites. Depending on the growth process, approaches can be divided into bottom-up and top-down, where the first includes heat-up, precipitation and *in situ* synthesis and the latter consist of bulk to nano processes [3; 5]. Overall, bottom-up strategies consist of a gas- or liquid-phase chemical reactions starting from molecules or ions; for example, the hot-injection and the ligand assisted reprecipitation methods fall into the liquid-phase chemical reaction category. On the other hand, top-down approaches involve a chemical or mechanical fragmentation and structuring of macroscopic solids [3].

2.3.1 Hot-injection technique

In the hot-injection method the steps of nucleation and growth happen at high temperature (often above 100°C and up to 200°C), following the injection of a precursor in a hot mixture containing a high boiling solvent, surfactants and other precursors [29; 3; 49; 5]. The reaction is generally carried out in an inert atmosphere [3]. In Figure 33, the typical reaction system is schematically represented.

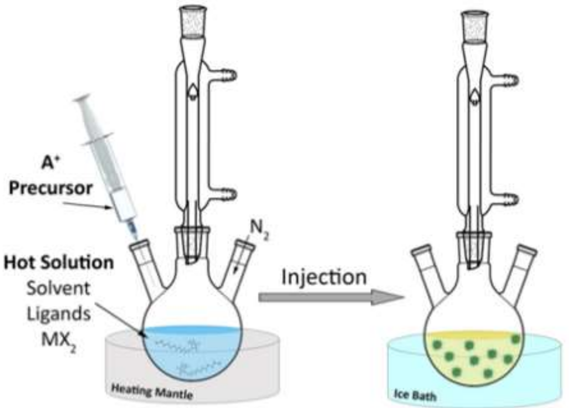

Figure 33. Schematic representation of the hot-injection approach [3].

This method has been proved to produce high quality monodisperse lead halide perovskite nanocrystals and can be used to synthesize lead-free perovskite nanocrystals too [5]. The obtained nanocrystals are small and follow a narrow size distribution because the method allows a theoretical separation between nucleation and growth. The first of these stages happens right after the injection and it finishes once there are no more monomers available [3; 11]. At this point the crystals grow, but there should not be any more nuclei formation. In practice, separation in time between the growth and nucleation stages is not easily obtained, since the formation of ionic crystal in the solution is fast and occurs without difficulty [3].

This synthesis makes it possible to control the size of the nanocrystal, their size distribution and their shapes by varying experimental parameters, such as the temperature of injection, the ratio of surfactants to precursors, the reaction time and the precursors concentration [26; 3; 5]. This important fact will be discussed thoroughly in the next paragraph.

Despite the advantageous possibility of finely tuning the properties of the final product, the hot-injection method is often not economically sustainable and it does not allow a facile up-scaling, since it requires high temperatures and inert atmospheres [3; 5]. Another problem encountered in metal halide perovskites nanocrystals' synthesis is the stability of the resulting products. These compounds are highly soluble in polar solvents, so they are not particularly stable under atmospheric conditions and a PLQY drop is generally observed. A solution to this issue might be the use of a halide excess during the synthesis, but the classical approach cannot achieve this condition because it uses metal halide salts both as a cation and an anion precursor. An alternative route is the "three-precursors" hot-injection approach, which starts from two distinct compounds as sources of cation and anion precursors. However, this alternative approach has a series of drawbacks too. First of all, the synthesis reported for this method have been used to produce only a limited range of compounds, indicating a poor reactivity of the halide precursors under the selected reaction conditions. Then, some of the reported synthesis also produce a variety of by-products [29; 3].

2.3.1.1 Features-tuning in hot-injection synthesis

As previously introduced, the hot-injection route is optimal to obtain nanocrystals with specific sizes or shapes, since it allows to tune some of the characteristics by modifying certain reaction parameters such as the amount of capping ligands, the temperature and so on. In particular for the capping ligands modulation, the following picture (Figure 34) shows how the chain length of both the alkyl chain acids and amines can affects the shape and size, making the distinction between higher and lower temperatures routes. The information used to delineate such schematic representation has been summed up from [2; 11; 1]. The highlighted parts correspond to the experimental conditions which will be followed in the experimental section of this thesis.

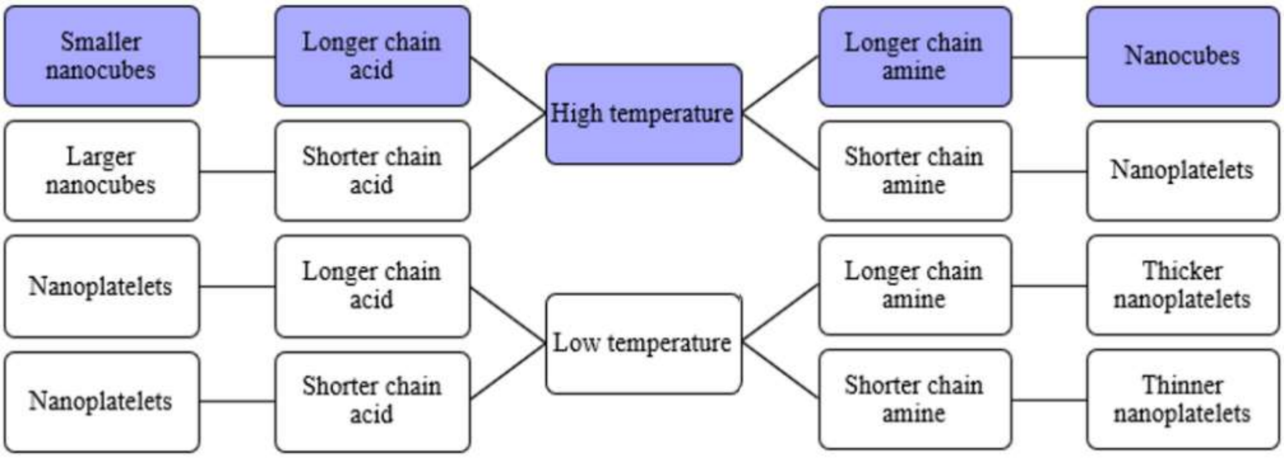

Figure 34. Schematic description of the influence of capping ligands on size and shape of the crystals during a hot-injection synthesis.

As can be observed from the schematic representation, the chain length of carboxylic acids has a less significant influence on shape selectivity, compared to amines chain length, but the first has a bigger influence over the size of the final product as opposed to the latter [2; 11]. Said shape selectivity is in fact a kinetically controlled process where the growth of high energy facets results faster than the low-energy ones. Surface energy is dependent on the selective bindings to certain facets of capping ligands and this binding is a dynamic process strongly influenced by temperature. Therefore, the conclusions reported in the figure can be explained by considering that shorter chain amines can get faster exchange mechanism on the surface since they are able to diffuse more rapidly than the long chain ones and this leads to a more evident shape anisotropy and to thinner nanoplatelets. Moreover, an increasing in the temperature results in weaker bonds between the amines and the surface, ending up in thicker nanoplatelets or nanocubes [2].

Beside the influence over the nanocrystals' size, the reaction temperature can affect the resultant product of the reaction in terms of quality, since a too high reaction temperature may lead to the formation of by-products and to the precipitation of some of the precursors, while a too low temperature may bring to an asymmetric growth of the nanocrystals [1]. Additionally, the reaction temperature can influence the final crystal geometry, which in turn impacts some major properties. Notably, all-inorganic lead halide perovskites can undergo phase transitions from cubic to tetragonal, from tetragonal to orthorhombic and from orthorhombic to monoclinic at specific temperatures; for example, the first two phase transition temperatures from the cited ones correspond to 130°C and 88°C respectively for $CsPbBr_3$ [50; 26].

2.3.2 Other heat-up techniques

Beside the hot-injection approach, this category comprises single-step bottom-up methods, such as the solvothermal approach, tip sonification, microwave irradiation and the microfluidic method, which work by applying heat to a mixture at atmospheric conditions. Said mixture is prepared by mixing the precursors and ligands in a solvent and the reaction is promoted by a temperature raise in the medium brought by a variety of heating up techniques [5]. The main advantage of these approaches is that they can work in atmospheric conditions, contrarily to the hot-injection one, and this makes the process more cost-effective and it makes it possible to scale up the production [3; 5]. In particular, the main advantages of the microwave heating are the low energy cost, the high heating rate and the excellent photophysical properties of the resulting products. On the other hand, the solvothermal method allows a better kinetic control over the nucleation and growth process, since the reaction is slower due to the experimental conditions (relatively high temperature and increased pressure). Lastly, the microfluidic method allows to work with both homogeneous temperature and reagents on ultrashort time scales, since it is suitable for rapid mass and energy transfer [1]. However, these alternative heat-up techniques maintain some of the problems encountered into the hot-injection approach; for one, it is not possible to tune the ratio of the halide precursor and the metal and a heat source is still required. Moreover, these methods do not offer the same level of size and shape control that can be obtained with the hot-injection technique [3].

2.3.3 Ligand-assisted reprecipitation technique

The ligand-assisted reprecipitation technique entails the dispersion of precursors in a good solvent (generally polar) and then the injection of this mixture in a poor solvent (generally nonpolar) containing surfactants. The conventionally used good solvents are dimethylformamide and dimethyl sulfoxide, while toluene and hexane are generally employed as poor solvents [29; 3; 49; 5]. The issues arising from the use of these reaction medium will be amply discussed in Paragraph 2.5.2.
A schematic illustration of the process is shown in Figure 35.

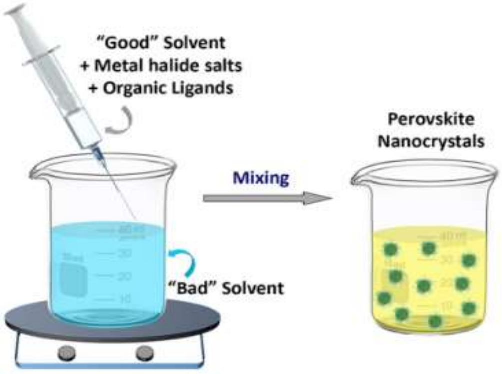

Figure 35. Schematic representation of the LARP approach [3].

In this case, the phenomenon occurs at low temperature (generally between room temperature and 60°C) and ambient atmosphere and the nucleation and growth are spontaneously brought up by a condition of supersaturation, because in such condition the system tries to go back to an equilibrium state [29; 3; 49; 5]. The supersaturated state can be accomplished in different ways: by lowering the temperature, by adding a solvent in which the substance has low solubility or by solvent evaporation [3; 5; 11]. Beside working at room temperature and in atmospheric conditions, contrarily to the hot-injection approach, this technique allows a scale up of the process [3]. Another perk of this technique is the possibility to control the nucleation and growth processes and to tune the size of nanocrystals by varying the temperature [5]. Furthermore, the sizes and shapes of the obtained nanocrystals are influenced by the chosen ligands and solvents [1]. In particular, it has been shown that carboxylic acids are necessary to avoid agglomeration, while amines allow to control the crystallization process and consequently the size of the nanocrystals [11].

On the other hand, this approach can achieve a lower level of shape control when confronted with the hot-injection method. The main morphologies obtained with this technique are spherical or nanoplatelets [5]. The following table (Table 1) sums up the influence of capping ligands on the final morphology obtained from a reprecipitation method and its information are collected from [51; 50].

Table 1. Influence of the capping ligands on the final products of the synthesis.

Acid chain	Amine chain	Final morphology
Hexanoic acid	Octylamine	Spherical quantum dots
Oleic acid	Octylamine	Nanoplatelets
Oleic acid	Dodecylamine	Nanocubes
Oleic acid	Oleylamine	Quantum dots; face to face stacking nanoplatelets; 2D flat-lying nanosheets
Acetic acid	Dodecylamine	Nanorods

Lastly, the employment of polar solvents can prove to be an issue, since it entails a reduction of the production yield and it might bring to the formation of defective nanocrystals. DMF, for example, may bring to the degradation and to the aggregation of the produced nanocrystals [4; 1].

The LARP approach belongs to the precipitation bottom-up methods and in this same category is also included the emulsion LARP technique which helps purify the nanocrystals by precipitation into solid-state light-emitting powder form [5].

2.3.4 Other reprecipitation techniques

Along with the LARP approach there are two other methods that involve a precipitation step: the emulsion LARP and the microemulsion. The first of these synthetic routes is based on the use of a demulsifier in an emulsion system created by mixing nonmiscible solvents, such as DMF and n-hexane [26; 3; 1]. The demulsifier leads the system through a supersaturated state, which sets off the crystallization process and, consequently, its quantity is quite influential over the size of the resulting products [3; 1]. Figure 36 report a schematic description of the emulsion process.

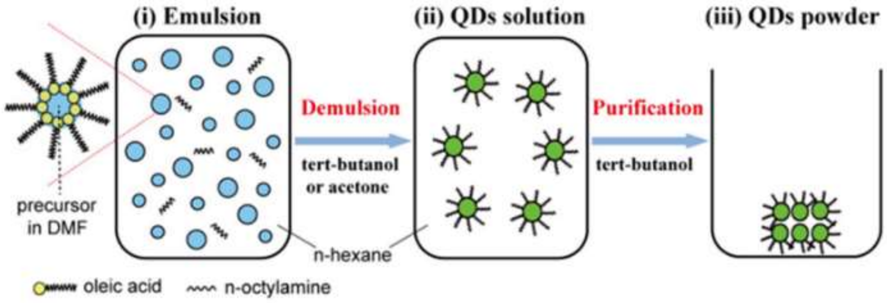

Figure 36. Schematic representation of the emulsion method [52].

The microemulsion technique involve the re-organization of the polar – nonpolar system in micelles. These ordered structures act as nanoreactors where the nanocrystals are formed, so the nucleation and growth stages are controlled by the diffusion process of the precursors from the main phase to the micelles. This method also involves a demulsifier, but this substance is here used to precipitate the already formed product and not to start the reaction. The microemulsion route can be divided into two groups: the conventional one where the micelles form in a polar phase and stabilize the nonpolar phase inside thanks to their hydrophobic carbon chains, and the reverse microemulsion approach where the ordered structures form in a nonpolar phase and stabilize the polar phase on the inside by turning inward the hydrophilic head groups [3].

2.4 Post-synthetic treatments

The ionic character of lead halide perovskite nanocrystals and their intrinsic instability can be exploited to modify such materials after the synthesis. These variations can be conducted while maintaining the original crystal structure or by disposing the atoms in a different configuration and can be used to obtain perovskites with specific compositions which cannot be produced by direct synthesis [23; 5]. For instance, post-synthetic treatments are often used to dope the obtained nanocrystals with the aim of making them more structurally, chemically and photochemically stable [5]. However, the cited intrinsic instability is also detrimental during some of the post-synthetic treatments; the purification step generally ends up removing the ligands weakly bonded to the surface and this leads to the deterioration of the materials' optical properties and, at times, to the loss of structural integrity [11].

2.4.1 Purification and separation

Beside the synthetic portion of nanocrystals' preparation, the purification steps are particularly important to achieve perovskite nanocrystals with satisfactory quantum yields [37]. Especially when the nanocrystals are to be used in optoelectronic devices, it is important to purify the products to remove the excess ligands on the surface [4; 11]. Indeed, such compounds are generally organic and consequently, poor conductors, so they may limit the current flow leading to a reduction in the performance of the devices. Moreover, the solution's physical properties may be affected by the viscous consistency of the capping ligands present in excess [4].

The method generally used to purify perovskite nanocrystals consists of a solvent/nonsolvent procedure, where the nanocrystals are precipitated and redispersed using solvents such as acetone, ethanol, methanol, acetonitrile and ethyl acetate. The main problem of this technique is that it may lead to loss of colloidal and structural integrity in the final product, due to the use of excessive amounts of polar solvents [37; 11]. Such polar solvents can, in fact remove part of the capping ligands, as shown in Figure 37.

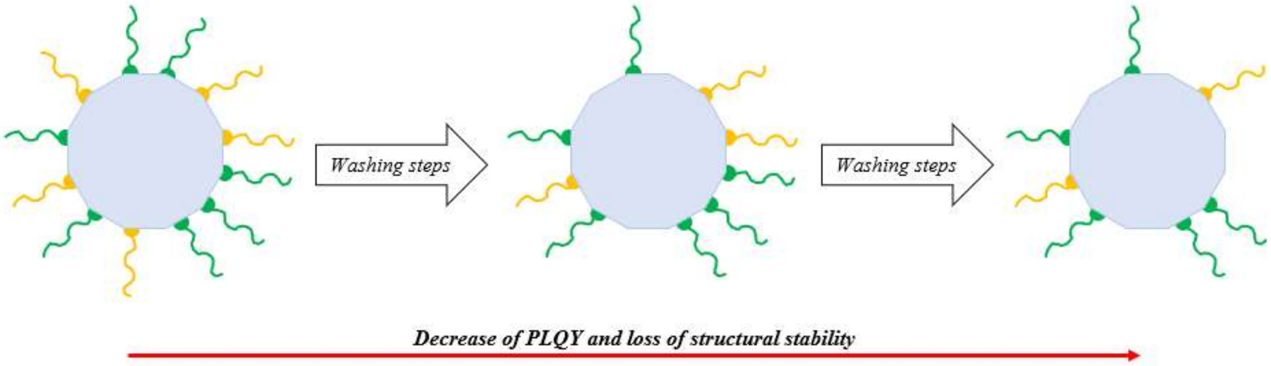

Figure 37. Description of the loss of capping ligands during the purification steps.

The reason such mediums lead to reduced stability and to a loss of photoluminescence quantum yield lies in the halide deficiency that rises from the interaction with the polar environment [41]. It has been shown that the addition of little amounts of the compounds used as ligands in the crystals' solution, prior to the precipitation step, can help stabilize the structure and maintain the photoluminescence of the product. However, the addition of the capping ligand does not prevent completely the dissolution of the materials and, for example, an excess of amine can decompose the nanocrystals too [37]. The alternative way to reverse the reaction consists in adding more halide salts in the solution [41].

Therefore, the solvent should preferably have a medium polarity to allow the precipitation of the nanocrystals while avoiding the removal of bound ligands or the degradation of the crystals. Moreover, aprotic solvents are to be favoured since, contrarily to the protic ones, they do not promote the removal of lead cations from the structure [4].

2.4.2 Anion exchange

As introduced in paragraph 2.2.1.1, anion exchange is particularly interesting because it allows to tune the nanocrystals' optical properties, such as the photoluminescence colour, since lead halide perovskites' band gap is mostly dependent on the halide present in the structure. This allows to adapt them to the chosen application [5; 1].

Owing to the ionic character of metal halide perovskites, the halide exchange process is generally quite fast and it can be applied by using an external source of halide anion or by employing perovskite nanocrystals with different anionic components. Such post-synthetic modification can be applied more easily compared to cation exchange, so the reaction can even be conducted at low temperature and can be used to operate both a partial or a complete substitution [50]. Anion exchange is an easier reaction in lead halide perovskites because of the ample concentration of halide vacancies, which makes it possible for such anions to possess a rather high mobility [53; 17; 23]. A general description of anion exchange in caesium lead bromide perovskites is reported in Figure 38.

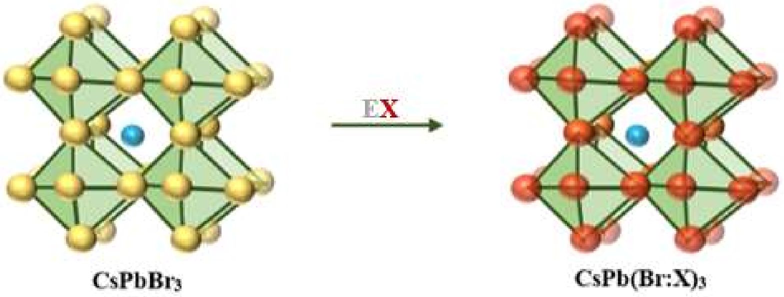

Figure 38. Description of a complete anion exchange. Br anions are yellow, while Cs cations are light blue and Pb cations are green. The inserted X anions are red.

The choice of halide precursor to operate the exchange with is particularly important, since such compounds should not contain a cationic portion that may exchange with the A cation already present in the structure. So, for example, methylammonium halides should be avoided since the cation may exchange with Cs^+ in all-inorganic perovskites [53; 50]. Furthermore, such precursors should be soluble in nonpolar solvents, since polar medium may damage perovskites structures and negatively affect their properties [50]. The exchange with compounds which are not amply soluble in the nonpolar solvent of choice can still happen, but it may remain incomplete or it may require a longer period of time under stirring in order to reach a specific emission wavelength [53]. When other perovskite compounds are used as halide precursors, a homogeneous distribution is obtained, and the achieved emission is an intermediate between the ones in the starting perovskite nanocrystals [53; 5]. Figure 39 sums up the possible anion exchange reactions that may be applied to all-inorganic lead halide perovskite nanocrystals.

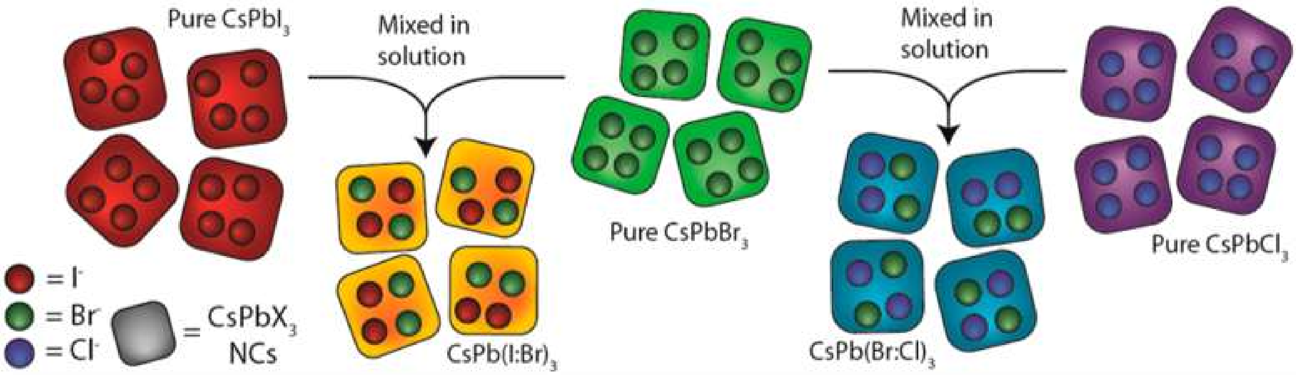

Figure 39. Anion exchange between different perovskite nanocrystals [53].

It has been observed that this compositional modulation does not modify the final nanocrystals' phase, meaning that the starting cubic phase is maintained throughout the process. In spite of this, a fluctuation in the size of the nanocrystal is expected due to the new anions' size. In particular, the size increases when a bromide ion is substituted with an iodide one and the size decreases when the same anion is substituted with a chloride ion [53; 50]. Another thing to consider is that the reverse reactions for halide exchange are not always possible. Thus, it is not possible to exchange a bromide anion with a chloride one and an iodide ion with a bromide ion if tetrabutylammonium halide is used as a precursor. This specific example can be explained by soft/hard acid-base interactions [50]. The theory of hard and soft acids and bases has been introduced by R. G. Pearson, who categorised acids and bases as hard or soft, mainly based on their polarizability, and stated that hard compounds prefer to interact with each other and so do soft compounds (hard acids – hard bases; soft acids – soft bases) [54].

2.4.3 Cation exchange

Cation exchange can be used to dope perovskite nanocrystals, meaning that a different cation is introduced in the structure in a controlled way to modify the properties of the material [17]. Both the A-site and B-site cations can be modified. For example, the caesium present in all-inorganic perovskites can be substituted fully or partially by organic cations such as methylammonium [$CH_3NH_3^+$] or formamidinium [$CH(NH_2)_2^+$], to produce hybrid organic-inorganic perovskites [23; 4]. It has been seen that cation exchange is possible when going from caesium(I) to methylammonium, which is a large cation, even if this transformation leads to lattice expansion. On the other hand, the exchange from Cs^+ to smaller cations, such as K^+ or Rb^+, results in the decomposition of the nanocrystals or succeeds only partially. These observations indicate that cation sublattice might be more rigid in halide perovskites than it is in other compounds [5]. The picture (Figure 40) describes the modification of the cation in the A-site.

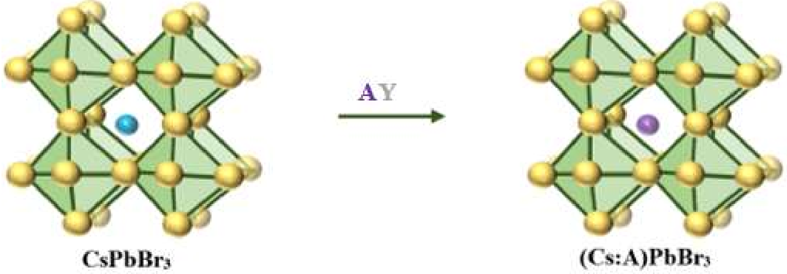

Figure 40. Description of the A-cation exchange. Br anions are yellow, while Cs cations are light blue and Pb cations are green. The inserted A cation is purple.

Instead, the bivalent cation Pb^{2+} can be partly exchanged with tin, zinc or cadmium cations [23]. Some other transition metal ions have been studied and they showed a better thermodynamic stability and improved PLQY. Beside the previously listed ones, between these smaller ions, Ni^{2+}, Cu^{2+} and Al^{2+} are worth mentioning [4]. Figure 41 reports the general change seen when B-cation exchange is applied.

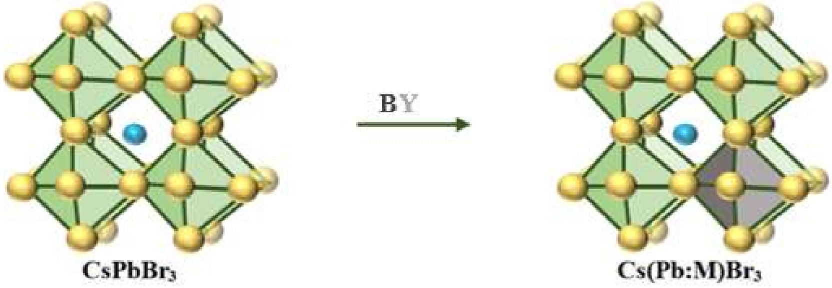

Figure 41. Description of the B-cation exchange. Br anions are yellow, while Cs cations are light blue and Pb cations are green. The inserted B cations are grey.

The B-cation exchange is generally limited by the low diffusion rate of the cations themselves in the perovskite's lattice. Moreover, replacing lead(II) cations with smaller ones gradually produces compressive strain in the lattice, which makes the process less favourable the more cations are substituted into the structure. However, it has been shown that the rate of cation exchange can improve if anions are exchanged at the same time [5].

2.4.4 Restructuring

It is also possible to modify the main structure by adding or removing one or more ions from the original material in order to obtain low-dimensional structures. A 0D perovskite structure, where the $[PbX_6]^{4-}$ octahedra are disconnected one from the other, can be obtained starting from $CsPbX_3$ perovskites through the removal of PbX_2 molecules [23; 3; 5]; in particular, Pb(II) can be removed by adding a bigger amount of amines, as these can act as bases [3; 41]. This structure is described by the formula Cs_4PbX_6 and it can also be the starting point to re-obtain the original structure $CsPbX_3$ by adding back the PbX_2 molecules, through the addition of more acid which serves to increase the ammonium concentration to then stabilize the original phase [23; 41]. Such conversions can be easily identified thanks to the colour change which happens due to the large band gap energies difference between the structures [23]. At times, the transformation from $CsPbX_3$ to Cs_4PbX_6 is considered to be a useful post-synthetic process since the latter is said to present higher photoluminescence quantum yields (more than two orders of magnitude higher). The increase in PLQY is sometimes explained considering that the lower dimensional structure possesses a higher exciton binding energy and the generated excitons remain confined in the single octahedra [55]. This statement is not universally recognized. The information regarding the photoluminescence of different perovskite forms is not uniform, as some other scientific articles suggest that the Cs_4PbX_6 structure is non-luminescent [42; 41]. This second hypothesis is justified by recent studies, which reported that its band gap is too wide to see a photoluminescence emission [42]. Beside these two distinct ways of thinking, a third explanation has also been given. It is possible that the zero-dimensional structure does not emit as a pure compound, but only when the $CsPbBr_3$ phase is also present. In this case the non-luminescent structure would act as a host for the other conventional perovskite materials [25]. However, this hypothesis is at least partially invalidated by the fact that luminescence has been detected for Cs_4PbBr_6 perovskites even when the other phase is not present. Moreover, the independence of Cs_4PbBr_6 emission from the presence of $CsPbBr_3$ has been demonstrated and discussed in a published article [56]. In this work the possibility of detecting photoluminescence in Cs_4PbBr_6 nanocrystals is instead attributed to the effect the hydroxyl groups from the dispersing solvent has on the material's band gap [56].

These contrasting opinions over the photoluminescence of different structures is referred, not only to Cs_4PbX_6, but also to $CsPb_2X_5$ [42]. This third phase is a caesium-deficient two-dimensional structure and it generally forms in polar mediums, when CsX molecules are removed from the structure $CsPbX_3$. The latter can be in turn achieved from Cs_4PbX_6 with one of the previous methods or by removing CsX, using water as a solvent, since caesium halides are easily soluble in such medium. This transformation mediated by water has already been described in Paragraph 2.2.3.3. Moreover, the 2D structure can also be obtained through the addition of PbX_2 to the original structure [3; 41]. Figure 42 summarizes the restructuring processes that lead to the formation of Cs_4PbX_6 and $CsPb_2X_5$ phases starting from the three-dimensional $CsPbX_3$.

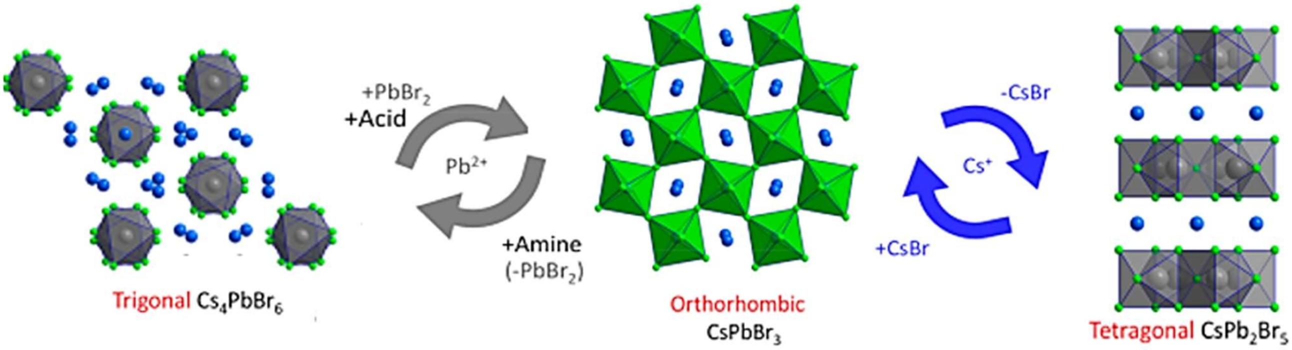

Figure 42. Representation of the restructuring processes that can be obtained post-synthesis. The picture has been modified from reference [41]. In the picture: A cations = blue; B cations = grey; X anions = green.

2.5 Toxicity and environmental issues

The toxicity problem evidenced in lead halide perovskites is a cause of concern and it often hinders the commercialization of devices containing these nanomaterials, as will be explained in Paragraph 2.6. Despite the outstanding performances of these compounds, alternatives are being studied in order to avoid the damages that the employment of lead could cause to human health and to the environment [58 ;1]. Nevertheless, the presence of lead in perovskite structures is not the only aspect that needs improving. Frequently, the large amount of solvents used during the preparation of such nanomaterials constitutes as much of a problem and should be taken into account when aiming at improving the production of nanoperovsites-based devices [58].

2.5.1 Lead

The main problem with the compounds studied in this thesis is the toxicity of lead, since lead halide perovskites can undergo degradation processes to produce water-soluble lead ions, which may interact negatively with the organism [5; 1]. Lead bivalent cations can in fact substitute a series of polyvalent cations in the organism, such as calcium, zinc and iron [57; 58]. Cells are not able to apply a selection mechanism to block lead because it is not an ordinary ion present in the organism and it tends to mimicry the characteristics of other ions present, such as the forementioned ones. The main problem is that the type of cations that can be substituted by lead have numerous functions and can travel on a great variety of binding sites, so it is quite difficult to identify one specific consequence of lead interactions in the blood flow and, in particular, with proteins [57]. Lead has been shown to have genotoxic properties and its poisoning targets the Central Nervous System, causing important damage to the genetic material in the brain through oxidative processes. Moreover, it can accumulate in the bones as lead phosphate, and it can lead to neurological disorders. Between the other consequences of lead's assumption, decreased fertility, cataracts, hypertension and cardiovascular and renal diseases are worth mentioning [58]. A general mechanism of its interactions in the organism can be defined. Lead cations are more affine for the protein sites compared to calcium and zinc, but it possesses an inert electron pair which leads to an irregular charge distribution that does not happen with Ca and Zn cations. This irregularity alters the structure and the function of the coordinated protein [57]. In Figure 43, a comparison between the charge distribution of calcium and lead is represented.

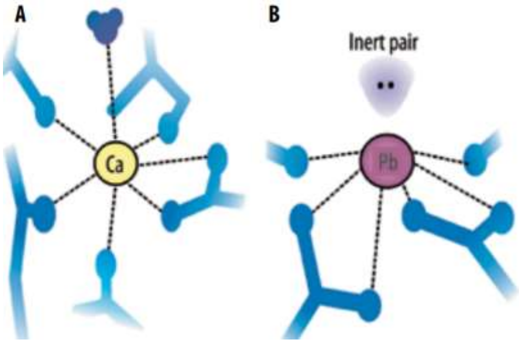

Figure 43. On the left: conventional binding of a calcium cation in the protein site. On the right: irregular charge distribution which arises from lead subtituting calcium or zinc in the proteins' sites [57].

When it comes to the possibility of using lead in optoelectronic devices, some limits have been imposed by the European Restriction of Hazardous Substances Directive (RoHS). These guidelines restrict the amount of lead that can be present in any continuous solid component of the device to 1000 ppm [23].

Alternatively, other metals could be studied as replacements for lead. Tin or germanium could be considered, since they both belong to Group 14 and possess the same properties of lead when it comes to coordination and charge and tin, especially, has a suitable band gap [1]. Moreover, tin(II) has a radius comparable to lead(II) and it can be used to form pure tin perovskites or to incorporate it in lead perovskites to improve the Goldschmidt's tolerance factor [10]. Considering the similarity between lead and these elements, the crystal structure of the obtained lead-free perovskites is the same as the one observed in the ones containing lead [5]. However, tin and germanium result problematic because of their tendency to oxidate from the oxidation state 2+ to the 4+ one [5; 1]. As a case in point, in tin halide perovskites this oxidation leads to the formation of perovskites' derivative described by the composition Cs_2SnX_6, with a zero-dimensional structure [5]. Antimony and bismuth are two other alternatives which would avoid the oxidation problem observed with the elements from Group 14. However, they would be used as trivalent ions, so the halide perovskite nanocrystals would assume the composition described by the formula $A_3B_2X_9$ [5; 1]. Perovskites obtained from elements belonging to Group 15 tend to have two- or zero-dimensional structures [5]. Indium, silver and tellurium have also been considered as alternative B-site cation in lead-free halide perovskites. In particular, indium and silver can be used as monovalent cations in combination with trivalent cations such as Bi(III), giving rise to $A_2BB'X_6$ structures [58]. Manganese can be used too, but it is mainly employed along with lead to modify the tolerance structure. Its main problem is the fact that it has quite an important size difference with respect to lead and this favours phase separation [10].

In general, lead-free perovskites formed from these alternative elements still require a lot of work to overcome the oxidative instability, to obtain satisfying properties and to gain a deeper understanding on their structure’s thermodynamic equilibria [11]. For now, as can be seen in Figure 44, their efficiencies do not reach similar values to the ones obtained for lead perovskites solar cells.

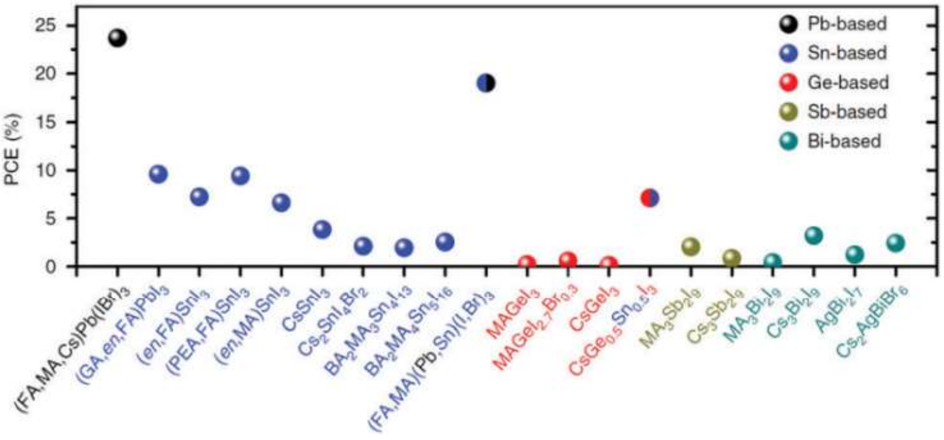

Figure 44. Comparison between the efficiencies of different perovskite materials used for solar cells. In the picture PCE stands for Process Cycle Efficiency [58].

Then again, it can be argued that, despite lead being a toxic and non-environmentally friendly resource, its alternatives are often more expensive and less available, since in most cases they are obtained as by-products from the extraction and production of other metals. Moreover, the alternatives studied are not always completely safe for human health and the environment. For instance, tin’s acute toxicity has been documented and, in particular, SnI_2 can be more problematic than the correspondent lead compound since the first is less stable [58].

2.5.2 Solvents

It has been shown that in some synthesis, lead precursors constitute only a small percentage of the human toxicity potential when compared to other precursors which are more concerning due to the larger amount of energy and solvents required to produce them [58]. Thus, safety and sustainability in the production of lead halide perovskites should also be guaranteed as much as possible in the choice of the precursors and during the synthetic process. To this end, it is imperative to study alternative solvents to the ones conventionally used during the synthesis pf lead halide perovskites, so to find the most suitable and most sustainable reaction medium. Indeed, the room temperature synthetic methods tend to employ dimethylformamide and dimethyl sulfoxide as polar solvents [4]. The first is classified as a reproductive toxicity hazard and the second is considered problematic in the matter of safety issues [59]. In particular, DMF is toxic for the liver and is at the moment classified as a probable carcinogen. Moreover, it is generally eliminated through an incineration process, which leads to the formation of NO_x, responsible for some environmental issues [4]. In fact, while the direct greenhouse effect (meaning the absorption of longwave radiation) of nitrogen oxides is negligible, they can present an indirect greenhouse effect, causing an increase in the temperature of the atmosphere. This second phenomenon is due to the fact that above a certain concentration value, NO_x can act as catalysts in the production of ozone (O_3) in the troposphere [60]. In some synthetic approaches it is not possible to completely avoid the use of polar solvents, so substitutes for the conventional ones should be found [4]. Cyrene (dihydrolevoglucosenone) and isopropanol have been proposed as more sustainable solvents. All in all, the first is a green alternative, since it is produced from cellulose waste and does not present mutagenicity or a high toxicity; however, it is quite expensive [4]. In this thesis water has been chosen as a greener alternative to the conventional polar solvents. This liquid is not used in perovskites' production, since it leads to degradation and some other instability problems that have been addressed in paragraph 2.2.3.3. However, it is the green solvent par excellence [61]. Water is in fact environmentally friendly and safe and it is not expensive or toxic [62]. Additionally, it is naturally abundant on Earth and, unless it is contaminated by toxic substances, it can be directly discharged once the reaction is terminated [61]. The solvents cited here are represented in Figure 45.

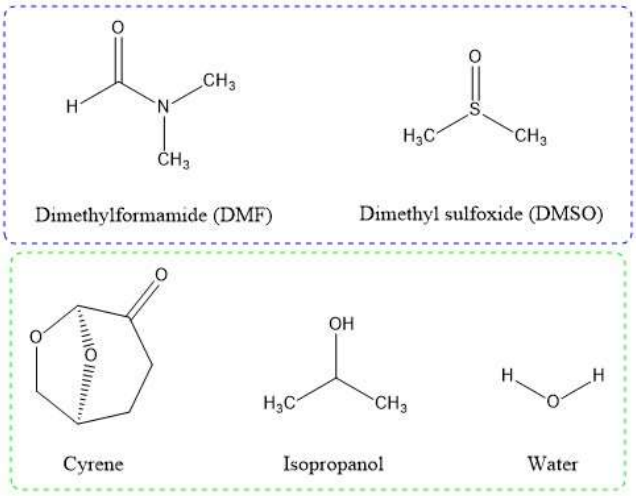

Figure 45. Top part: conventional polar solvents used in room temperature synthesis. Bottom part: more susteinable alternatives to conventional polar solvents.

Nonpolar solvents are also vastly used in most synthetic routes for lead halide perovskites and for these materials' dispersion. The most commonly used is toluene, which has been proven to be a health hazard, affecting negatively organs and fertility [4]. The green replacements to this solvent would be limonene and p-cymene, which are not toxic and can be obtained from citrus waste. These solvents can be used as reaction mediums, but different alternatives should be defined for the dispersion of the nanocrystals, since this second process requires liquids with more specific properties so not to interfere with possible optoelectronic applications and to guarantee the chance to correctly deposit the materials in thin-films. The most promising solvents to disperse lead halide perovskite nanocrystals are quaternary ethers, such as 2,2,5,5-tetramethyloxolane (TMO), and some esters like methyl pivalate, methyl butyrate, and ethyl isobutyrate [4]. All the solvents described as alternatives to toluene in this paragraph are represented in Figure 46.

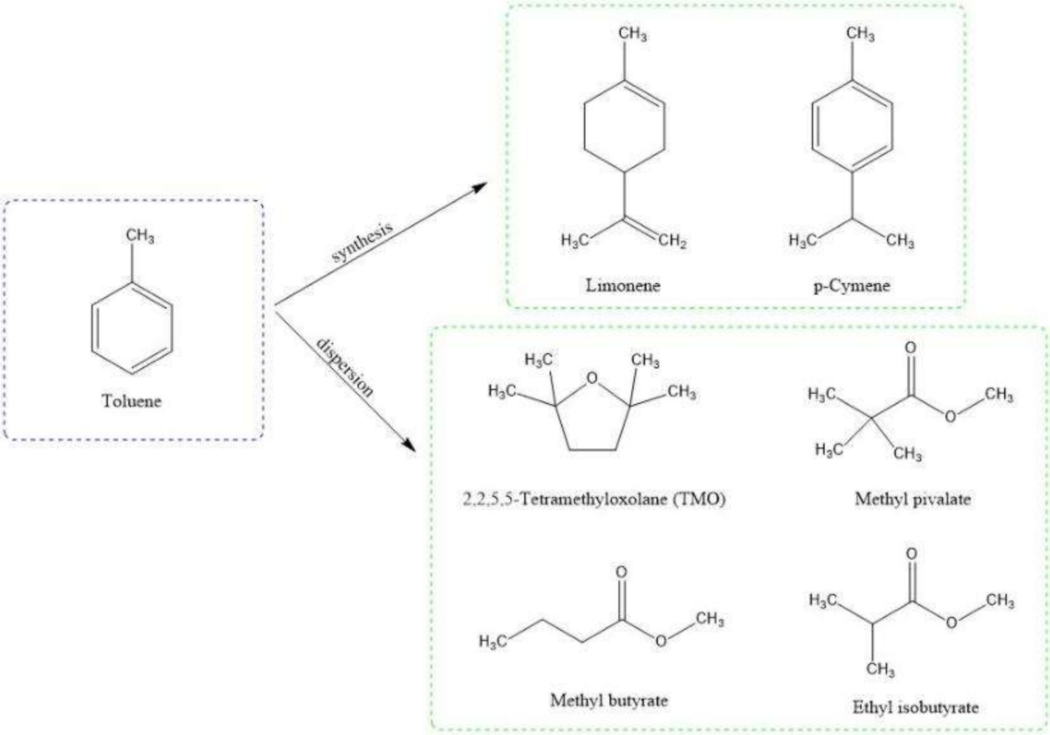

Figure 46. On the left: the most common nonpolar solvents used both as a reaction and a dispersion medium. On the right: alternative aplar solvents for the synthesis (top) and the dispersion (bottom) of lead halide perovskite nanocrystals.

2.6 Optoelectronic applications

There are several applications that make use of perovskite nanocrystals, taking advantage of their cost-effectiveness and of their remarkable properties (for instance, band gap tunability over visible range and easy and cost-effective solution processability) [26; 4; 58]. Their solution-processing can be operated in ambient conditions thanks to the high defect tolerance that these materials present [4; 58]. The optical and electronic properties can be tuned by changing one or more of the three ion types in the structure or by modifying the size, shape and structural dimensionality of these materials or again by altering the ratio between the long chain amine (capping ligands) and the precursors [26].

However, the device performance might be influenced by the density of traps per unit volume and by the energy of those traps and in lead halide perovskites such density depends mostly on post-processing procedures. Consequently, this may be an issue and it should be taken into consideration to improve the optoelectronic properties of these materials [35] Then, lead halide perovskites have some stability problems both intrinsic and linked to external factors such as moisture, light, heat and oxygen [35; 5; 58; 1]. Lastly, as explained in Paragraph 2.5.1, the presence of lead in the structure is problematic since it constitutes a risk to human health and to the environment [5; 58]. The main perovskite nanocrystals applications will be summarized into this paragraph.

Perovskite photovoltaic technology has recently sparked the interest of both the industrial and the academic world, since it involves a low-cost solution-processed fabrication [12; 58; 1]. Furthermore, perovskites are extremely versatile, given that all the of the component ions can be changed or modified [58; 1]. The devices fabricated to this day as perovskite solar cells can have different architectures, but they are generally made up by a first layer of transparent conductive oxide (TCO), an n-type semiconductor and a p-type semiconductor acting as the electron-transport layer (ETL) and a hole-transport layer (HTL) respectively and a black electrode. The perovskite absorber layer in this structure is positioned between the ETL and the HTL [63]. Depending on the order of the two semiconductors, two main configurations can be observed: formal (n-i-p) and inverted (p-i-n) [12; 63]. Figure 47 summarizes these structures.

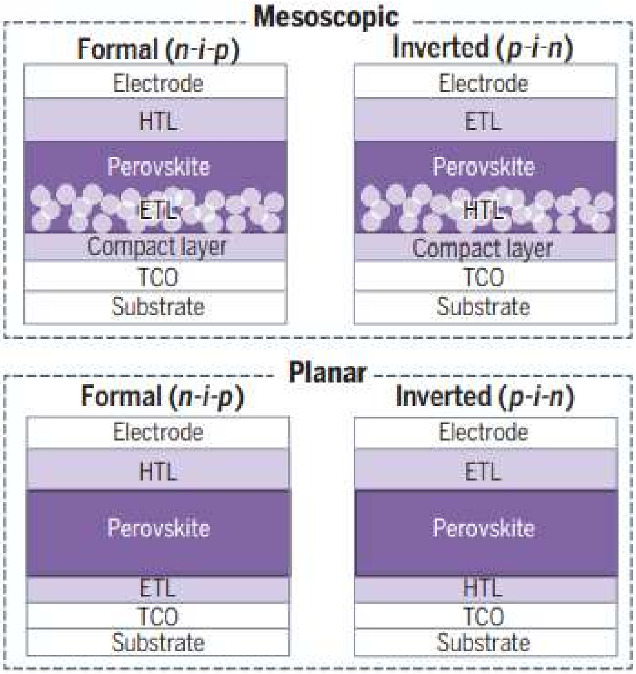

Figure 47. Representation of the different device configurations that may be observed in perovskites' solar cells [12].

In the last years this technology has seen a rapid growth, to the point of reaching efficiencies of light-to-electricity power conversion of around 25% [64; 11; 58]. Moreover, they are particularly interesting sustainability-wise because their expected Energy PayBack Time (EPBT) is shorter compared to the one of silicon solar panel (only a few months for perovskites versus 1.5 – 4.4 years for the conventional materials) [12; 58]. The Energy PayBack Time is the time of production that a renewable energy system (in this case a perovskites solar cell) needs to produce the same amount of energy that was required in order to fabricate the energy system itself [65]. However, as it has been remarked in this work, these materials present some problems stability-wise, which are often correlated with environmental factors, and the perovskite nanocrystals used nowadays for photovoltaic performances are the ones including lead(II) in the structure, an ion known for its toxicity [64; 5; 1]. The stability could be achieved by determining the best ligands' density on the surface of the nanocrystals, while the answer to the toxicity and environmental problems stands in the study of different metals to include in the B-sites of metal halide perovskites. Lately, this last idea has been considered and studied, by fabricating materials that include tin, germanium, bismuth or antimony in place of lead in the materials. Nevertheless, tin-based nanocrystals solar cells are the only ones with high enough efficiencies and they are also affected by great instability [5].

A different application sees perovskites as substitutes to the conventional materials used as light-emitting diodes. They are considered promising because of their superior optical performances, in addition to their facile synthesis methods. In particular, they are characterized by a tunable band gap, exceptional defect tolerance, high brightness and colour purity and they are compatible with the existing manufacturing technology [64; 5; 1; 14]. The two main configurations of perovskites LED are schematically represented in Figure 48. Once again HTL and ETL stand for hole-transport layer and electron-transport layer respectively; EML is the emitting layer.

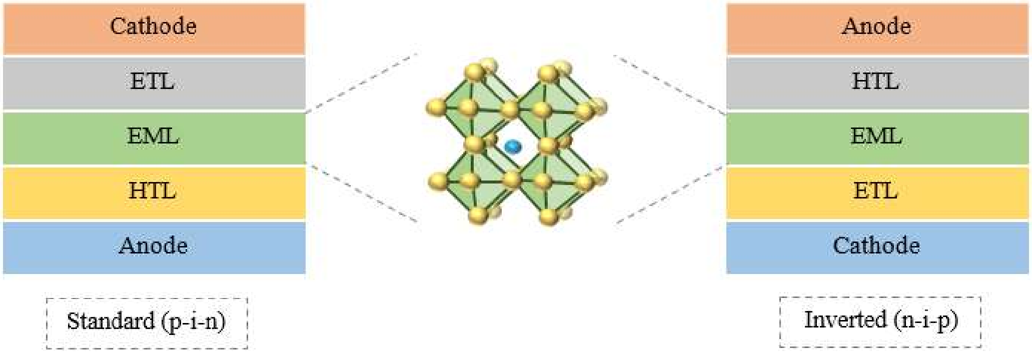

Figure 48. Representation of the typical perovskites LED.

Economically speaking they are better than the existing devices, because the cost of both their raw materials and the production is lower than the one observed in inorganic light-emitting diodes (ILEDs) and organic light-emitting diodes (OLEDs). In particular, the process results less expensive thanks to their high defect tolerance, which allows to carry out fast solution-based processes, causing an improvement on the overall production efficiency [14]. However, there is still the need for an improvement in perovskite LEDs' stability and it is important to achieve a scale-up to shift from the mm-level to large area displays with nanometre uniformity [5; 14]. Their instability to environmental factors can somehow be solved by using the same procedures typically applied to OLEDs, but their intrinsic instability cannot be reduced, and it might be accelerated due to the applied electrical current [5]. Another challenge in the use of perovskites in LED devices is the fact that blue emission in these materials is not as efficient as the green or the red ones and the first is necessary in this applicational field [14].

Lead halide perovskites are also good candidate for cost-effective solid-state lasers, since the possibility to tune their emissions wavelength is once again quite useful. Just like in the other applications described, perovskites' stability issues need to be solved in order to make progress in the production of lasing materials and it is necessary to word on lead-free alternatives to avoid lead's toxicity [5].

Perovskite materials can be used in photodetectors, where a different set of their properties makes them particularly appealing. These properties include high optical absorption coefficients, long charge carrier diffusion lengths, ambipolar charge transport and strong attenuation of visible and high-energy photons [5; 1]. In particular, perovskite nanocrystals are suitable for narrowband photodetectors, meaning those photodetectors which can only sense a narrow range of light [1]. This field of application requires some improvements too. The distribution of organic ligands should be controlled so to reduce dark current while avoiding an increase in the response times due to a reduction of charge extraction. Moreover, the interaction at the interfaces between the crystals and the contacts should be perfected and ion migration in perovskites should be reduced through the diminishing of vacancies' density [5]. More in general, these last required improvements are also referred to perovskite solar cells.

3. EXPERIMENTAL SECTION

3.1 Hot-injection

First, a conventional hot-injection method will be discussed to evaluate its well-known characteristics and establish a comparison with the approach developed in the following section (Paragraph 3.2).

3.1.1 Preparation

This section will contain the description of both the synthetic procedure, followed to obtain the desired nanomaterials, and the post-synthetic treatments applied in order to purify them. Before that, all the compounds used during the preparation are listed: lead acetate trihydrate ($Pb(OAc)_2 \cdot 3H_2O$), ≥99,99%, Sigma-Aldrich; caesium acetate (CsOAc), 99,9%, Sigma-Aldrich; trimethylsilyl chloride (TMS-Cl), ≥98%, Sigma-Aldrich; 1-octadecene (ODE), 90%, Sigma-Aldrich; oleylamine (OAm), 70%, Sigma-Aldrich; oleic acid (OA), 90%, Alfa Aesar; ethanol 96% vol, VWR Chemicals BDH; hexane, >99%, Sigma-Aldrich; ethyl acetate ≥99,5%, Sigma-Aldrich. All the chemical employed were used without further purifications.

3.1.1.1 Synthesis

The hot-injection synthesis for lead halide perovskite nanocrystals has been vastly studied and is mostly consolidated. The reaction process here described has been defined starting from the synthetic route proposed by Gamelin et al. [66].

The procedure used to synthesize the nanocrystals started with the addition of 0,2 mmol of $Pb(OAc)_2 \cdot 3H_2O$ to a 50 mL round bottom flask, containing 0,28 mmol of CsOAc in 28 mL of ethanol, along with 5 mL of the solvent (ODE) and the organic capping ligands (1 mL of OA and 0,5 mL of OAm). This mixture was stirred and degassed at room temperature for 5 minutes until the solution appeared transparent. At this point the solution was heated at 110°C for 60 minutes, while also stirring and degassing. Then the solution was heated to a higher temperature and a solution of TMS-Cl in octadecene was instantly injected in the flask. The chosen temperature has been varied between 160°C and 230°C from one synthesis to another to evaluate the influence of the heating conditions on the final nanocrystals. Right after the injection the solution became turbid and the flask was moved away from the heating system and cooled to room temperature using a water bath. Said solution appeared to have a different colour depending on the heating temperature chosen, but it was generally on a yellow or beige tone, and it presented a certain amount of precipitate on the bottom of the flask (Figure 49).

Figure 49. Aspect of the mixture obtained at the end of the heating step.

Afterward, the solution was centrifuged at 13000 rpm for 20 minutes at room temperature and the supernatant (characterized by a yellow or orange tone) was removed. The precipitate was generally dark white or had some darker parts (with a beige tone) towards the centre.

The following table sums up the conditions that differ between the samples that have been synthesized (Table 2). The amounts of $Pb(OAc)_2$, CsOAc, solvents and capping ligands are the same for each sample and they correspond to the ones described in this paragraph.

Table 2. The amount of TMS-Cl used in each preparation and the heating temperature at which the TMS-Cl solution was injected are reported.

Sample	TMS-Cl (mL)	T (°C)
HIP_1	0,2	229
HIP_2	0,2	229
HIP_3	0,2	233
HIP_4	0,2	200
HIP_5	0,2	200
HIP_6	0,2	200
HIP_7	0,3	200
HIP_8	0,2	160
HIP_9	0,2	160

3.1.1.2 Separation and purification

The obtained solid was resuspended in hexane and washed with 5 mL of ethylacetate for three times. Then it was centrifuged once again at 13000 rpm for 20 minutes and the supernatant was removed to leave a white solid.

Especially when working at lower temperatures (160°C), after centrifuging the precipitate resuspended in hexane, no solid was observed on the bottom of the centrifuge tube. As suggested by an article focused on capping ligand dynamic binding to the surface [37], a small amount of oleylamine and oleic acid was added to the solution (5 and 6 drops respectively) aiming at improving the nanocrystals' stability. After that, acetone was added dropwise until the solution appeared turbid. Then it was centrifuged at the conditions previously stated in this section and a precipitate was obtained. The main problem with this precipitation procedure is the aspect of the final product. It always had a sticky consistency and it was often transparent. Due to these unwanted characteristics, the sample required more the one washing with ethylacetate, until a white, crumbly solid was obtained.

3.1.2 Characterization

The samples have been characterized by X-Ray powder diffraction (XRPD) by means of a Philips diffractometer with a PW1319 goniometer with Bragg-Brentano geometry. The instrument is equipped with a focusing graphite monochromator and a proportional counter with a pulse-height discriminator. The characterization was conducted with a Nickel-filtered Cu Kα radiation and by the employment of a step-by-step technique. The latter considered steps of 0,05° in 2θ and a collection time of 30 s per step.

Their size and morphology have been analysed by scanning electron microscopy and the images have been acquired with a Sigma Zeiss VP Field Emission Scanning Electron Microscope (FE-SEM) working in high vacuum mode with an operating EHT voltage of 20 kV.

Since more than one sample has been obtained with the same exact procedure, we chose to analyse only some representative solids: one at each of the selected temperatures and one obtained by the injection of a solution presenting a higher quantity of TMS-Cl. However, the sample synthesized at lower temperature (160°) and the one containing a higher amount of TMS-Cl were obtained in a very small amount, due to the necessity of washing them repeatedly. This resulted in the impossibility of characterizing them. Consequently, only samples HIP3 an HIP4 were studied.

3.1.2.1 X-Ray diffraction

The white solid obtained at the end of the synthetic route has been analysed by X-ray diffraction and all the samples' diffractograms show peaks which can attributed to lead chloride perovskite nanocrystals with the general formula $CsPbCl_3$. The comparison of the achieved diffractogram with $CsPbCl_3$ peaks reported in the ICSD database [67] is reported in Figure 50.

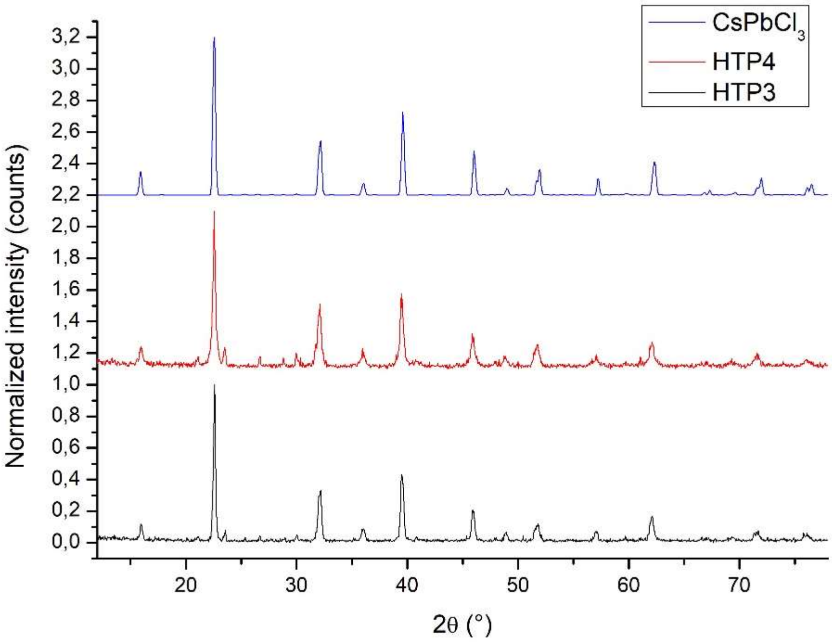

Figure 50. Comparison between the diffractograms of sample HIP3, HIP4 and the $CsPbCl_3$ diffractogram between 5° and 80°, reported in the ICSD database.

This picture shows that both the analysed samples present the characteristic peaks ascribable to $CsPbCl_3$ with an orthorhombic crystal system.

The orthorhombic crystal structure of $CsPbCl_3$ is represented in Figure 51.

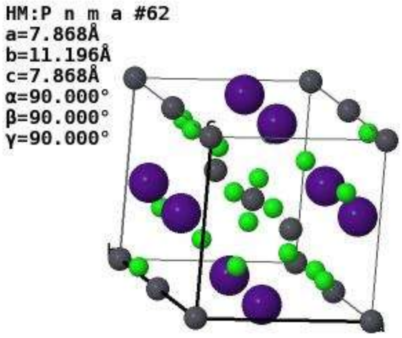

Figure 51. Crystal system of $CsPbCl_3$ [67].

3.1.2.2 Scanning electron microscopy

Prior to the SEM characterization the solids have been dispersed in hexane.
All the samples analysed show that the obtained crystals are nanocubes and the temperature variation does not modify such shape. In the following figures some of the SEM images are reported (Figure 52 and 53).

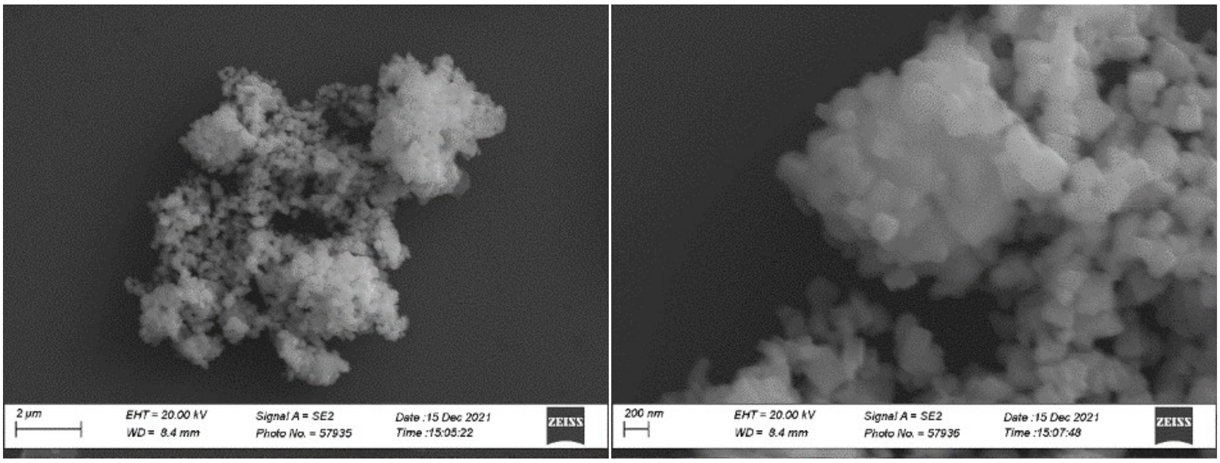

Figure 52. SEM images of sample HIP_3.

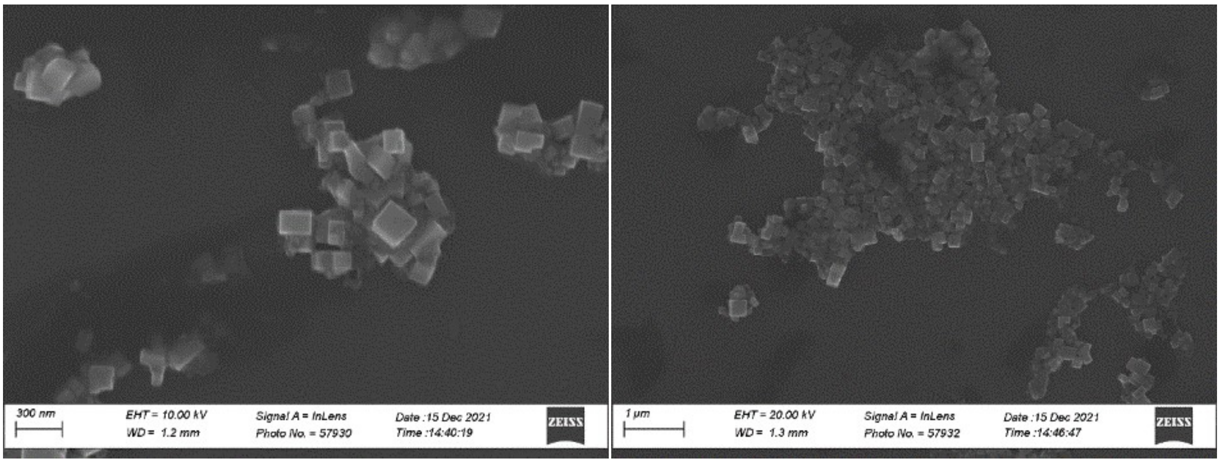

Figure 53. SEM images of sample HIP_4.

SEM micrographs evidence that the shapes are quite regular for all the samples, but the nanocubes present some size distribution for samples HIP3 and HIP4. It has been found that sample HIP3 present particles of dimensions in the range 76 – 460 nm with a mean value of 210 nm. On the other hand, sample HIP4 contains nanocrystals characterized by smaller sizes, in the range 20 – 245 nm and the calculated mean value is 113 nm. This difference between samples obtained at different reaction temperature is illustrated in the graph reported in Figure 54.

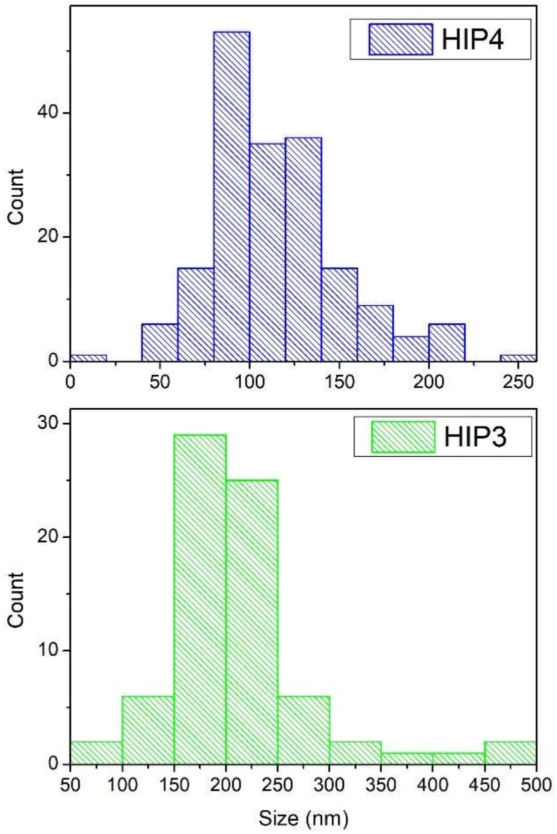

Figure 54. Graphical representation of particle size measurements of samples HIP4 (top) and HIP3 (bottom).

3.1.3 Discussion

During the preparation TMS-Cl was used as the source of halide anions because it has been shown that using a dedicated compound as halide source has a positive influence on some of the materials' properties. Indeed, it has been reported that having two distinct sources of lead cations and halide anions guarantees the chance to control the composition of the nanocrystals, since it allows to tune independently the amount of these constituents. This generally results in better optical properties, such as higher PLQYs, and greater stability under atmospheric conditions thanks to the possibility of working with a halide excess [29; 3]. Moreover, one of the samples (HIP_10) has been obtained by using a bigger amount of TMS-Cl in order to verify if the presence of an excess of halide in the solution may improve the nanocrystals stability during the purification stage. However, it was not possible to characterize this sample because of the amount of solid obtained, which was not sufficient for any kind of analysis.

The white precipitate obtained at the end of the process did not show any emission under an ultraviolet light with a wavelength of 365 nm. However, further characterizations should be conducted to verify if a small degree of luminescence can be detected. On the other hand, the supernatant showed a blue emission under the forementioned UV light, which might lead to think that the desired perovskite nanocrystals are suspended in the solvent. To check for this possibility, the compounds used as capping ligands in the synthesis (oleylamine and oleic acid) have been observed under the UV lamp where they showed the same luminescence. This may confirm that the purification steps with hexane and ethyl acetate are useful to remove the capping ligands that are present in excess in the final product.

These observations are focused on the synthetic part of this section, but some more information can be deduced from the characterization of two of the obtained samples as well. The characterized samples showed that only one perovskite phase was formed at the end of this synthetic pathway. As expected, the temperature variation did not bring to the formation of different shapes of the final nanocrystals, since all the considered range (160 – 230 °C) is included in the high temperature reactions and the influence on the shape is mainly due to the chosen capping ligands and in particular to their chain length. A shape change could be expected if temperatures below 100 °C were used because, when moving to lower temperatures, a shift in the shape from nanocubes to nanoplatelets should happen, as explained in Paragraph 2.3.1.1. On the other hand, as described by the schematic representation reported in that same paragraph, the nanocubes shape is in accordance with the capping ligands used in the reaction. Both oleylamine and oleic acid possess, in fact, longer chains. Considering this, the size of the obtained perovskite nanocrystals should be contained as longer chain acids at high temperatures should provide smaller nanocubes. As it can be seen from the SEM images, the obtained materials present average dimensions of 100 – 220 nm and in the same sample a variety of sizes can be distinguished. Seeing as the acid chain is the most influential between the two types of capping ligands when it comes to size control, it is possible that such size variations are to be attributed to the fact that the oleic acid added in the reaction medium is not enough to allow an adequate interaction with the species. Temperature changes have a bigger impact on the size of the nanocrystals rather than on their shapes. On average, a decrease in the reaction temperature led to the formation of smaller nanocrystals as can be seen from the comparison of the dimensions of samples HIP3 and HIP4, obtained by SEM technique.

3.2 Room temperature

As anticipated, an innovative method, developed with the purpose of improving some critical aspects of other well-established synthetic approaches, will be here discussed. Said discussion will include the description of the procedure employed to obtain the nanocrystals, the analysis of the information acquired through a variety of characterization techniques and the examination of the achieved results.

3.2.1 Preparation

The synthesis and the post-synthetic steps of separation and purification are reported in the following paragraph. The compounds employed during both procedures are here reported: lead acetate trihydrate ($Pb(OAc)_2 \bullet 3H_2O$), ≥99,99%, Sigma-Aldrich; caesium acetate (CsOAc), 99,9%, Sigma-Aldrich; potassium bromide (KBr), ≥99%, Sigma-Aldrich; citric acid (CA) anhydrous, Sigma-Aldrich; milli-Q water; acetone, J.T.Baker; ethanol 96% vol, VWR Chemicals BDH. All the chemical employed were used without further purifications.

3.2.1.1 Synthesis

The synthetic procedure described in this section has been ideated and developed as an alternative to the hot-injection method reported in the previous chapter and to the conventional room temperature approaches.

In a 50 mL round bottom flask, 0,4 mmol of lead acetate trihydrate ($Pb(OAc)_2 \bullet 3H_2O$) are dissolved in 10 mL of water and 1,6 mmol of potassium bromide are added with the purpose of producing lead bromide ($PbBr_2$). The solution immediately turns cloudy once KBr is inserted in the flask, forming the lead bromide. The solution was then centrifuged at 13000 rpm for 15 minutes and the transparent supernatant was discarded aiming to reduce the amount of impurities. The white solid was resuspended in 10 mL of water and a variable amount of citric acid was added to the turbid solution. After 5 minutes, a solution of 0,28 mmol of caesium acetate (CsOAc) in 5 mL of water was added. This led to the formation of a white precipitate. Figure 55 shows how the reaction medium turns cloudy after the addition of caesium acetate.

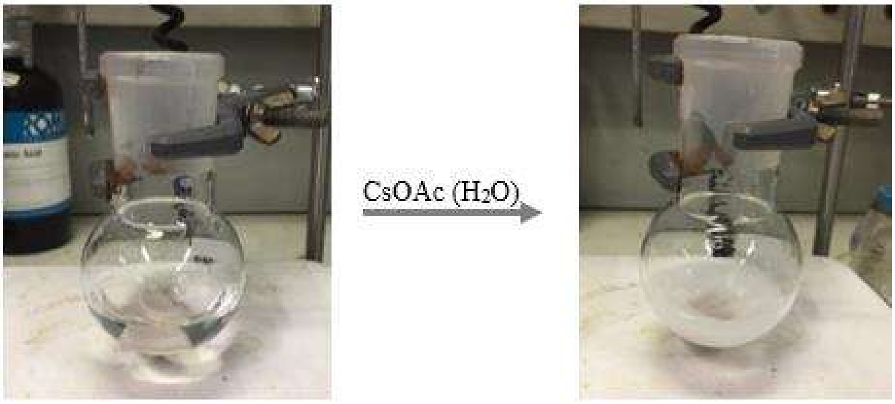

Figure 55. Addition of caesium acetate to the reaction medium.

After some time (between 15 and 120 minutes depending on the sample), the solution was centrifuged using the same conditions previously described. The white solid (Figure 56) and the supernatant were isolated and stored for further characterization. These white solids are labelled as RTPx, where x correspond to an identification number.

Figure 56. White solid obtained at the end of the synthetic procedure.

The synthetic process has been studied by varying the reaction temperature, the reaction time right after the addition of caesium acetate and the amount of citric acid introduced in the solution. The following tables (3, 4 and 5) report the experimental parameters used for three groups of samples. In the following tables CA/Pb(OAc)$_2$ stands for the ratio between citric acid and lead acetate.

Table 3. Information on the samples obtained throughout the study on the influence of the reaction temperature over the final product.*

Sample	**CA/Pb(OAc)$_2$**	**Temperature**	**Reaction time**
RTP13	5,20	20	15
RTP14	3,94	30	15
RTP15	6,49	40	15
RTP16	4,37	50	15
RTP17	5,20	60	15
RTP18	5,57	70	15

* These samples do not have a regular amount of citric acid because some trials where needed to identify the best quantity of this compound. The samples reported in the next tables will present a controlled amount of this reagents as they have been obtained after the aforementioned trials.

Table 4. Information on the samples obtained throughout the study on the influence of the reaction time over the final product.

Sample	CA/Pb(OAc)$_2$	Temperature	Reaction time
RTP27	8,02	18	0
RTP28	8,01	18	5
RTP29	7,91	18	10
RTP21	8,00	18	15
RTP22	7,98	18	30
RTP23	8,00	18	45
RTP24	8,02	18	60
RTP25	8,00	18	90
RTP26	8,01	18	120

Table 5. Information on the samples obtained throughout the study on the influence of citric acid's content over the final product.

Sample	CA/Pb(OAc)$_2$	Temperature	Reaction time
RTP36	0	18	15
RTP37	1,09	18	15
RTP38	2,47	18	15
RTP43	4,01	18	15
RTP44	5,53	18	15
RTP45	7,01	18	15
RTP42	8,57	18	15
RTP41	9,95	18	15

3.2.1.2 Separation and purification

The solvent in the supernatant was removed by rotary evaporation at 40°C, 144 rpm for 2 hours, leaving a white crystalline solid and an oily portion, attributed to the excess of citric acid. At the beginning, this solid did not emit and, even when it dried completely and switched colour from white to orange, it still did not emit. The time span for the drying up was variable, depending on the sample treated and on the environmental conditions. Sometimes, this colour changing did not happen or at least happened in a longer time interval; this has been attributed to a higher degree of moisture in the air. For instance, sample RTP38 did not turn orange after 5 days, even if on average the time necessary for the colour change ranges between 5 hours and 2 days. This might be due to the fact that their washing process was taken care of during particularly humid days. The final obtained orange powders were washed with acetone five times, discarding the cloudy transparent liquid each time and eventually obtaining a mixture of light orange and yellow powders. The separation of the two components was done by way of acetone thanks to the fact that the yellow solid remains suspended in the solvent, while the orange one precipitated at the bottom of the flask. The solids were washed three other times with acetone, using an ultrasonic bath to make sure all the lighter portion was suspended. Each time, right after taking the flask out of the ultrasonic bath, the liquid containing the lighter solid was removed and transferred into a 50 mL beaker. After letting the solid in the beaker sediment, the supernatant was discarded and both this solid and the one left in the round bottom flask were left to dry out at ambient conditions. Then they were both stored and then characterized. In Figure 57 the two different types of solid obtained at the end of the purification step are shown. From now on the darker solids will be labelled as RTPx-1, while the lighter ones will be RTPx-2.

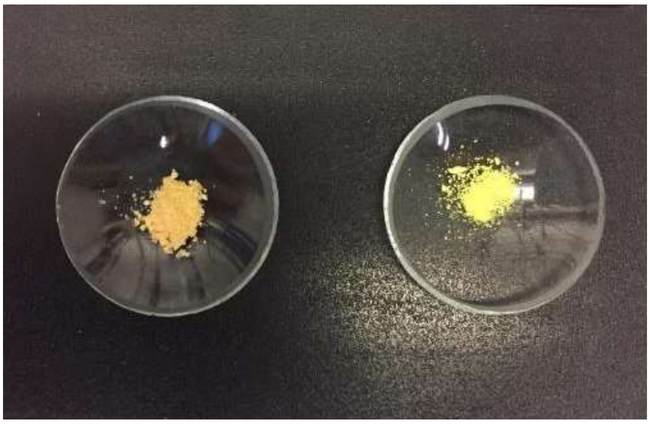

Figure 57. Two types of solid obtained at the end of the purification stage. On the left (darker one, RTPx-1), the solid left in the round bottom flask can be observed, while on the right (lighter one, RTPx-2) the solid remained at the bottom of the beaker is shown.

3.2.2 Characterization

All the samples have been characterized by XRD, SEM and PL and PLE spectroscopy. An Empyrean Panalytical diffractometer equipped with a Theta/Theta goniometer with Bragg-Brentano geometry has been used to determine the phases present in the samples. The sample has been spined during the analysis and a Cu Kα radiation was employed. The PIXcel3D-Medipix3 1x1 detector operates on a continuous scanning mode. A Sigma Zeiss VP Field Emission Scanning Electron Microscope (FE-SEM) working in high vacuum mode at 20 kV has been used to collect some images of the nanocrystals where the morphologies and dimensions can be deducted. This last characterization was coupled with an energy-dispersive X-ray spectroscopy (EDS) analysis, which was necessary to determine the composition of the different crystals observe d in the samples. The optical properties of the nanocrystals were studied by the acquirement of PL and PLE spectra by means of a Jasco FP-750 spectrophotometer. The instrument uses a 150W Xenon lamp, a silicon photodiode as a detector and holographic concave monochromators. Lastly, infrared spectroscopy has been used to determine if a coordination of citric acid can be identified; for this last investigation a Perkin-Elmer SpectrumOne spectrometer was used, and the sample was prepared in KBr.

3.2.2.1 X-ray diffraction

The characterization of the white solid that precipitates right after the caesium precursor addition allows to conclude that such compound is lead citrate monohydrate ($Pb(C_6H_6O_7)\cdot H_2O$) [68; 69]. In Figure 58 a comparison with literature's diffractograms is reported, while Figure 59 reports some of the measured diffractograms.

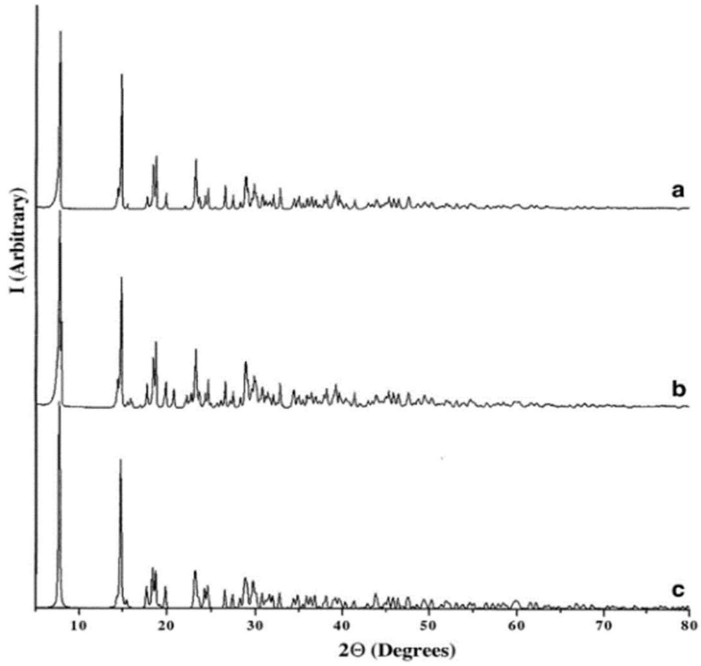

Figure 58. Diffractograms of lead citrate monohydrate reported by Kourgiantakis et al. (a) and Sonmez et al. (b and c) [68;69].

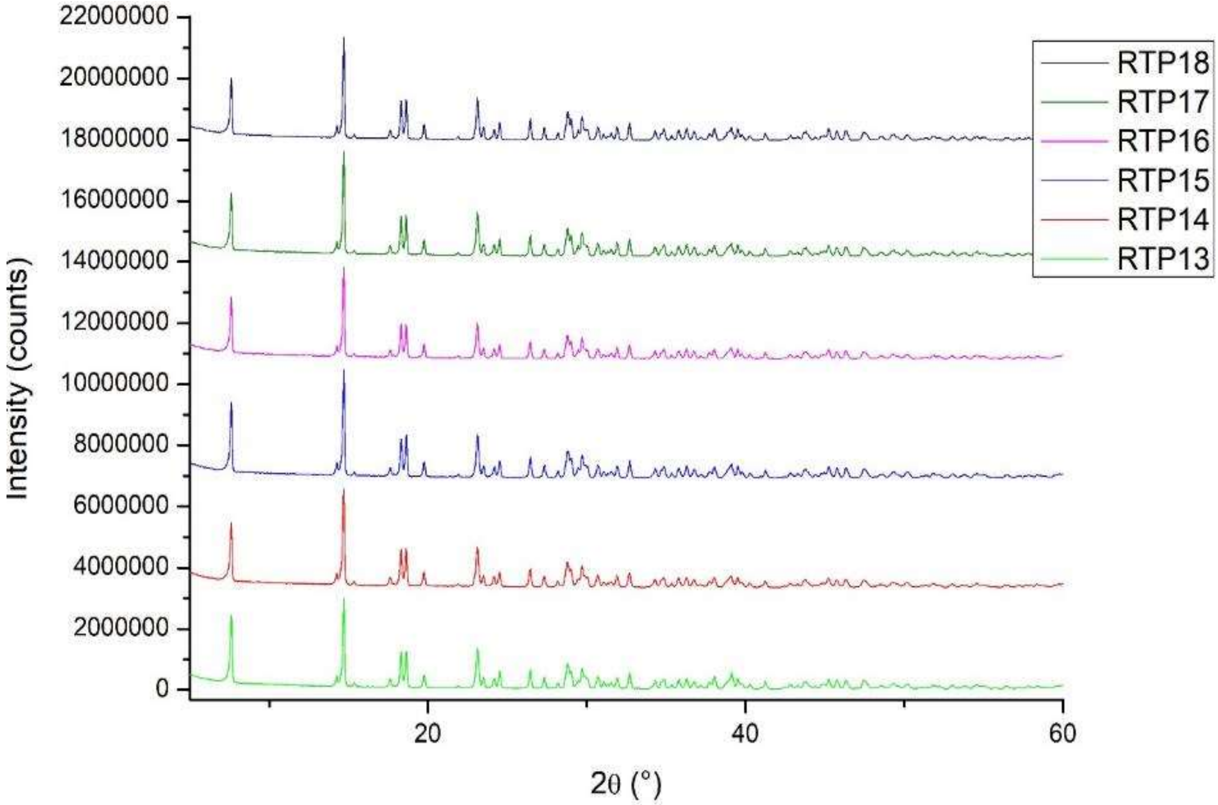

Figure 59. Diffractograms of samples RTP13 - RTP18 between 5° and 60°.

The characterization of the solids previously listed in Tables 3, 4 and 5 can be summarized by mainly attributing the orthorhombic $CsPbBr_3$ and the tetragonal $CsPb_2Br_5$ phases to the orange specimens. On the other hand, the generally lighter coloured specimens crystallized in the trigonal form Cs_4PbBr_6. In Figure 60 the crystal structures of these three perovskite phases are shown.

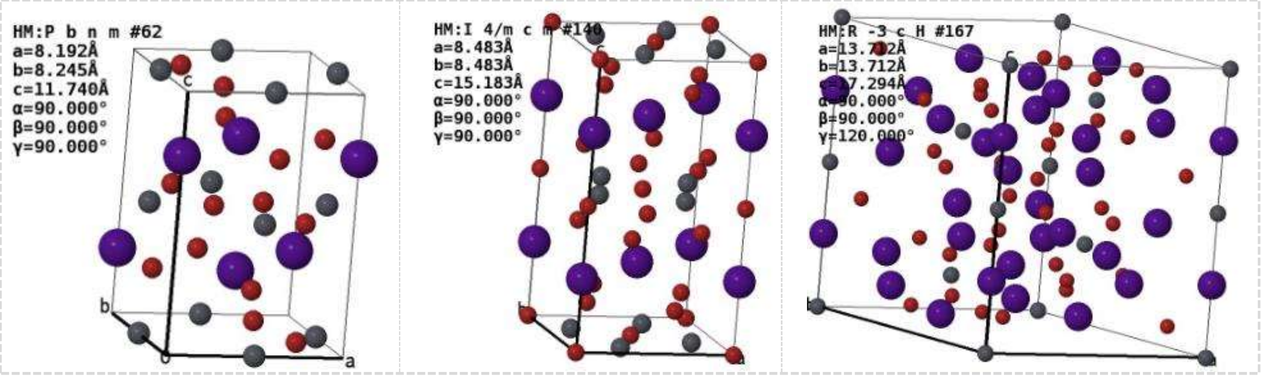

Figure 60. Crystal structures of $CsPbBr_3$ (left), $CsPb_2Br_5$ (centre) and Cs_4PbBr_6 (right).

3.2.2.1.1 Reaction temperature

Table 6 summarizes the effect of the reaction temperature on the phases formed in each sample.

Table 6. Summary of the phases detected in each sample analysed during the temperature study of this work.

Sample	**Phases detected from the diffractogram**				
	$CsPbBr_3$	***$CsPb_2Br_5$***	***Cs_4PbBr_6***	***CsBr***	***Unidentified***
RTP13-1 (20°C)	x		x	x	
RTP13-2 (20°C)			x	x	
RTP14-1 (30°C)	x	x	x		x
RTP14-2 (30°C)			x	x	x
RTP15-1 (40°C)	x	x	x		
RTP15-2 (40°C)			x	x	
RTP16-1 (50°C)	x	x	x	x	
RTP16-2 (50°C)			x	x	
RTP17-1 (60°C)	x	x	x	x	
RTP17-2 (60°C)			x	x	
RTP18-1 (70°C)			x	x	
RTP18-2 (70°C)	x			x	

The samples in this table are ordered from the lowest to the highest temperature (20°C – 70 °C).

The $CsPbBr_3$ and $CsPb_2Br_5$ phases are only present in RTPx-1 type of samples. However, these samples present the Cs_4PbBr_6 phase as well, even if this structure mostly characterizes the RTPx-2 specimens. The presence of this last phase in both type of solids might indicate that they were not washed thoroughly and, consequently, that more washing steps with acetone were needed.

Figure 61 reports the diffractograms of the RTPx-1 samples.

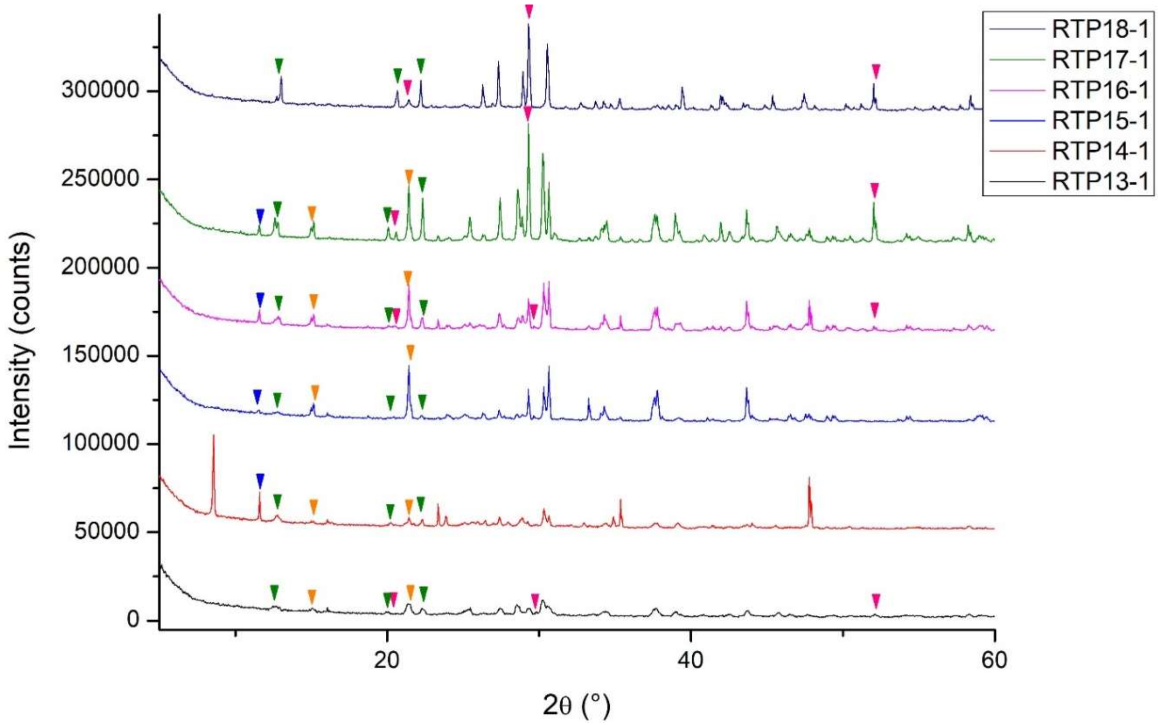

Figure 61. Diffractograms of samples RTPx-1 (between 5° and 60°) obtained in order to study the influence of the reaction temperature over the final products. In the picture the different compounds have been identified with coloured triangles: orange corresponds to $CsPbBr_3$, blue to $CsPb_2Br_5$, green to Cs_4PbBr_6 and magenta to CsBr.

The diffractograms share some common peaks, but they differ one from the other in a way that is not easily correlated to temperature variation. All the samples, beside RTP18-1, contain the $CsPbBr_3$ phase and its peaks are generally the most intense. The Cs_4PbBr_6 phase is present in all the analysed solids, but its signals have a lower intensity when compared to the ones of $CsPbBr_3$. The conventional $CsPbBr_3$ is the only perovskite structure present RTP18-1, where the peaks appear to be quite narrow. Moreover, starting from sample RTP15-1 until sample RTP18-1 the intensity of the peaks with maxima positioned at 12,7° and 12,9° (attributed to Cs_4PbBr_6) grows. Lastly, the $CsPb_2Br_5$ structure can be observed in the four intermediate samples, but not in the ones obtained at low (20°C) and high (70°C) temperature (RTP13-1 and RTP18-1 respectively). Then there are peaks that cannot be identified as perovskite phases, such as the one at 8,5° and the one at 52,1°. Most of the samples present in fact signals ascribable to CsBr and sample RTP14-1, which does not seem to contain this halide salt, present narrow peaks of a compound that was not univocally identified. The qualitative analysis of the diffractograms has been done by comparison of the experimental patterns with the ones obtained from the ICSD database [67]. In Figure 62, the comparison between the diffractogram of a sample and the ones of the contained phases is reported. The other comparisons will be reported into the appendix (Paragraph 6.1) of this thesis.

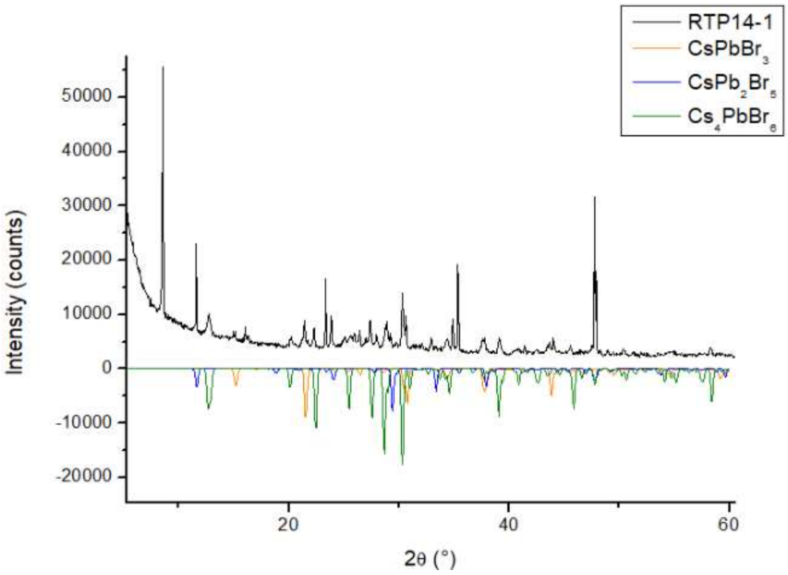

Figure 62. Diffractogram of sample RTP14-1 between 5° and 60°.

Figure 62 reports the entire pattern for the specimen RTP14-1 together with the calculated intensities for the three crystalline phases derived from the ICSD database.

As to the RTPx-2 samples, their diffractograms are reported in Figure 63.

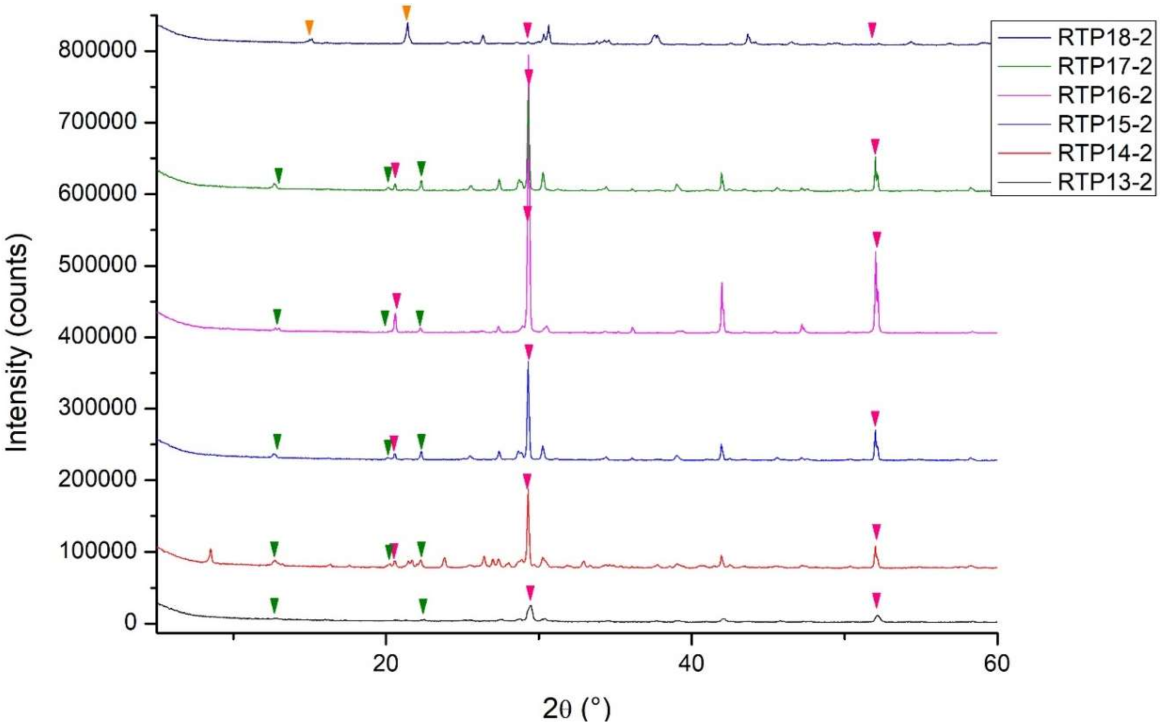

Figure 63. Diffractograms of samples RTPx-2 (between 5° and 60°) obtained in order to study the influence of the reaction temperature over the final products. In the picture the different compounds have been identified with coloured triangles: orange corresponds to $CsPbBr_3$, blue to $CsPb_2Br_5$, green to Cs_4PbBr_6 and magenta to CsBr.

Compared to RTPx-1 sample, RTPx-2 ones are more homogeneous. Their diffractograms evidence the presence of Cs_4PbBr_6 and CsBr. This group too has some exceptions; sample RTP14-2 contains once again peaks ascribable to the unknown lead compound and sample RTP18-2 shows signals that can be associated with the $CsPbBr_3$ phase instead of the Cs_4PbBr_6 one. The diffractogram of RTP14-2 is reported in Figure 64.

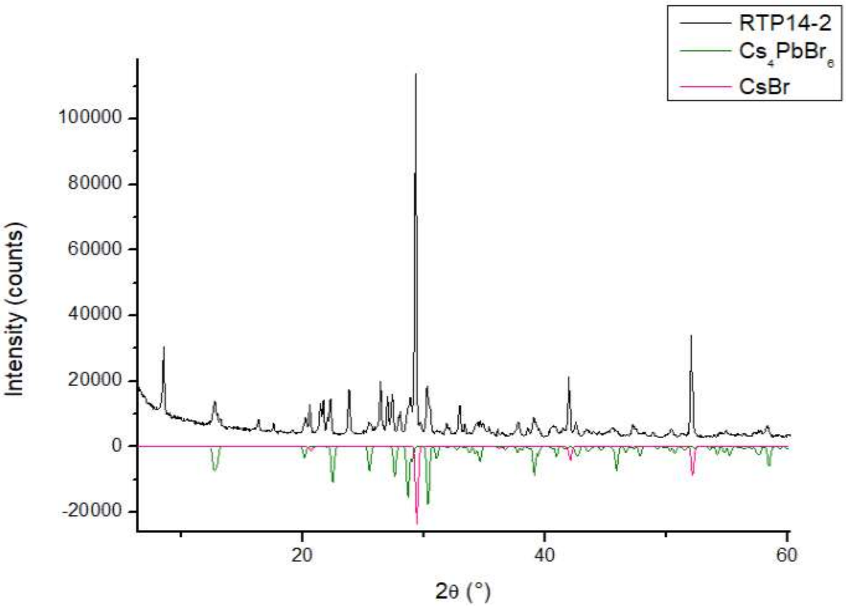

Figure 64. Diffractogram of sample RTP14-2 between 5° and 60°.

As anticipated, this sample present the characteristic signals of the Cs_4PbBr_6 phase, of caesium bromide and of the unknown compound.

In order to complete the qualitative description, the diffractograms of sample RTP18 are shown in Figure 65.

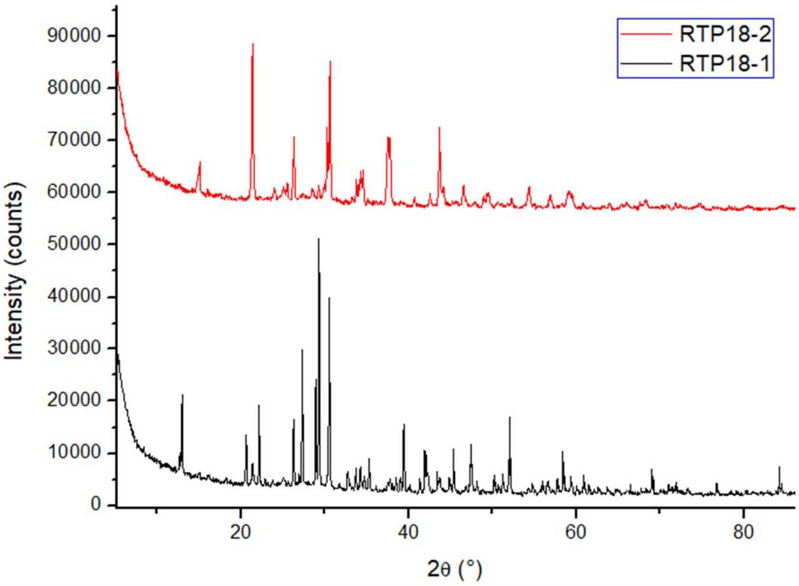

Figure 65. Diffractogram of samples RTP18-1 and RTP18-2 between 5° and 85°.

In these last diffractograms, the respective samples differ greatly from the others of their group. RTP18-1 present a single perovskite phase, Cs_4PbBr_6, and this incredible difference might be a consequence of the higher reaction temperature, or it might be due to different factors that were not controlled during the process, such as the humidity in the air at the end the washing process or the ambient temperature in this same drying step. On the other hand, sample RTP18-2 only shows peaks attributable to the $CsPbBr_3$ phase. This can be explained with more certainty. After the solid was separated and left to dry in the beaker, a small amount of water was added, which inverted the process applied during the washing steps. This will be better explained in Paragraph 3.2.3.

3.2.2.1.2 Reaction time

The second group of samples that will be analysed is the one including the compounds obtained after different reaction times. In Table 7 the phases observed in each sample are schematically reported (RTPx-1 compounds represent the solid left on the bottom of the flask, while RTPx-2s are the solids separated into a beaker).

Table 7. Summary of the phases detected in each sample analysed during the reaction time study of this work.

Sample	**Phases detected from the diffractogram**				
	$CsPbBr_3$	***$CsPb_2Br_5$***	***Cs_4PbBr_6***	***CsBr***	***Unidentified***
RTP27-1 (0 min)	x		x	x	x
RTP27-2 (0 min)	x		x		x
RTP28-1 (5 min)	x	x			
RTP28-2 (5 min)			x	x	
RTP29-1 (10 min)			x	x	x
RTP29-2 (10 min)			x		x
RTP21-1 (15 min)	---	---	---	---	---
RTP21-2 (15 min)			x	x	
RTP22-1 (30 min)	x		x	x	x
RTP22-2 (30 min)			x	x	x
RTP23-1 (45 min)	x	x	x		
RTP23-2 (45 min)			x	x	x
RTP24-11 (60 min)	x	x			
RTP24-12 (60 min)	x	x	x		
RTP25-1 (90 min)	x	x	x	x	
RTP25-2 (90 min)	x		x		
RTP26-1 (120 min)	x	x	x	x	x

In this table the samples are ordered from the lowest time interval (0 min) to the highest one (120 min) and there does not seem to be a regular trend between them. The phase most frequently detected is Cs_4PbBr_6, followed by the $CsPbBr_3$ and then by the $CsPb_2Br_5$. Beside these perovskite structures, impurities ascribed to CsBr and to the previously cited unknown compound are present.

Differently to what has been observed in the samples from Paragraph 3.2.2.1.1, the diffractograms of samples RTPx-1 are very variable. Figure 66 reports a comparison among these samples. This figure does not report the diffractogram of sample RTP21-1 since it was obtained in such a limited quantity that it was not possible to acquire the X-ray diffraction data.

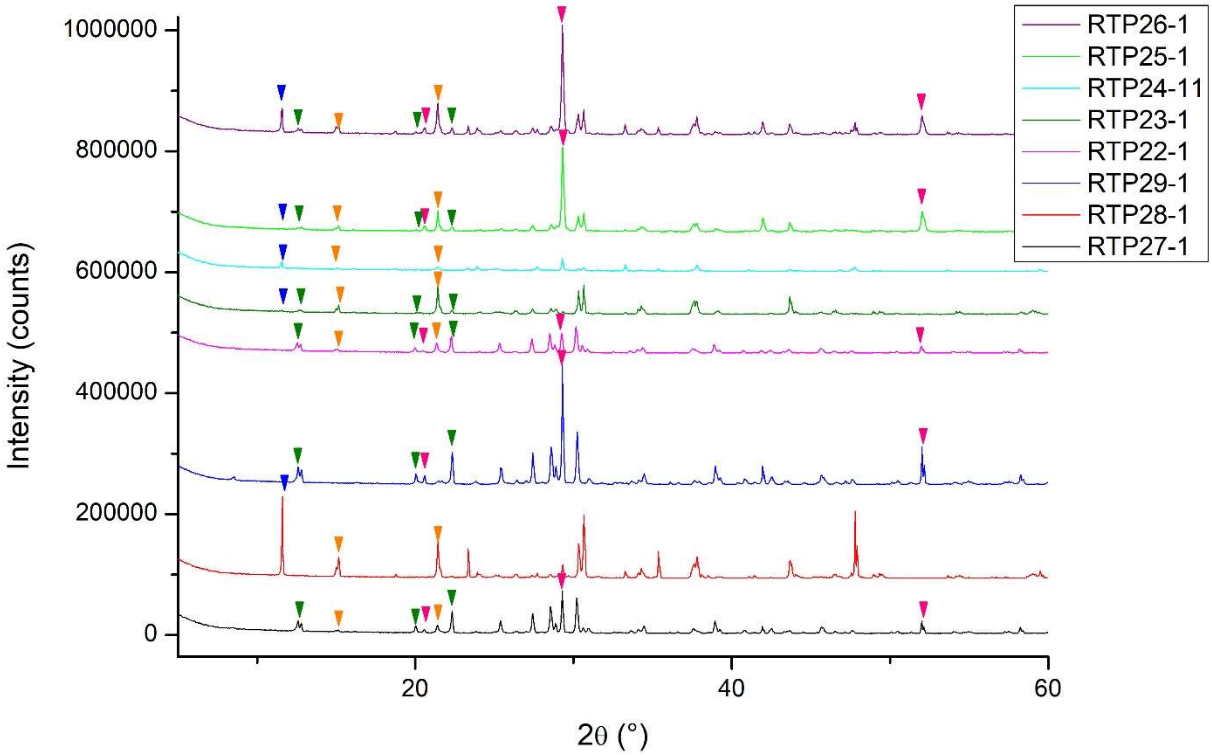

Figure 66. Diffractograms of samples RTPx-1 (between 5° and 60°) obtained in order to study the influence of the reaction time over the final products. In the picture the different compounds have been identified with coloured triangles: orange corresponds to $CsPbBr_3$, blue to $CsPb_2Br_5$, green to Cs_4PbBr_6 and magenta to CsBr.

The most frequent phase identified is $CsPbBr_3$, which can be observed in all the samples beside RTP29-1. All these solids, beside the ones obtained at 0 minutes (RTP27-1) and 30 minutes (RTP22-1), also present the $CsPb_2Br_5$ phase which, once again, is not detected in RTP29-1. Like for the samples analysed in the previous paragraph, most of the RTPx-1 samples of this group present the Cs_4PbBr_6 phase and this does not seem to be somehow linked to the time change, since its detection does not follow a regular pattern. Lastly, these solids present the same impurities as observed in the samples RTP13 – RTP18. Caesium bromide was found in five out of the eight samples and four out of these specimens present the unidentified compound.

Samples RTPx-2 have also been analysed and their diffractograms can be observed in Figure 67. Sample RTP26-2 is not present since, during the washing and separation process, only one solid was obtained and it was described along with the RTPx-1 samples.

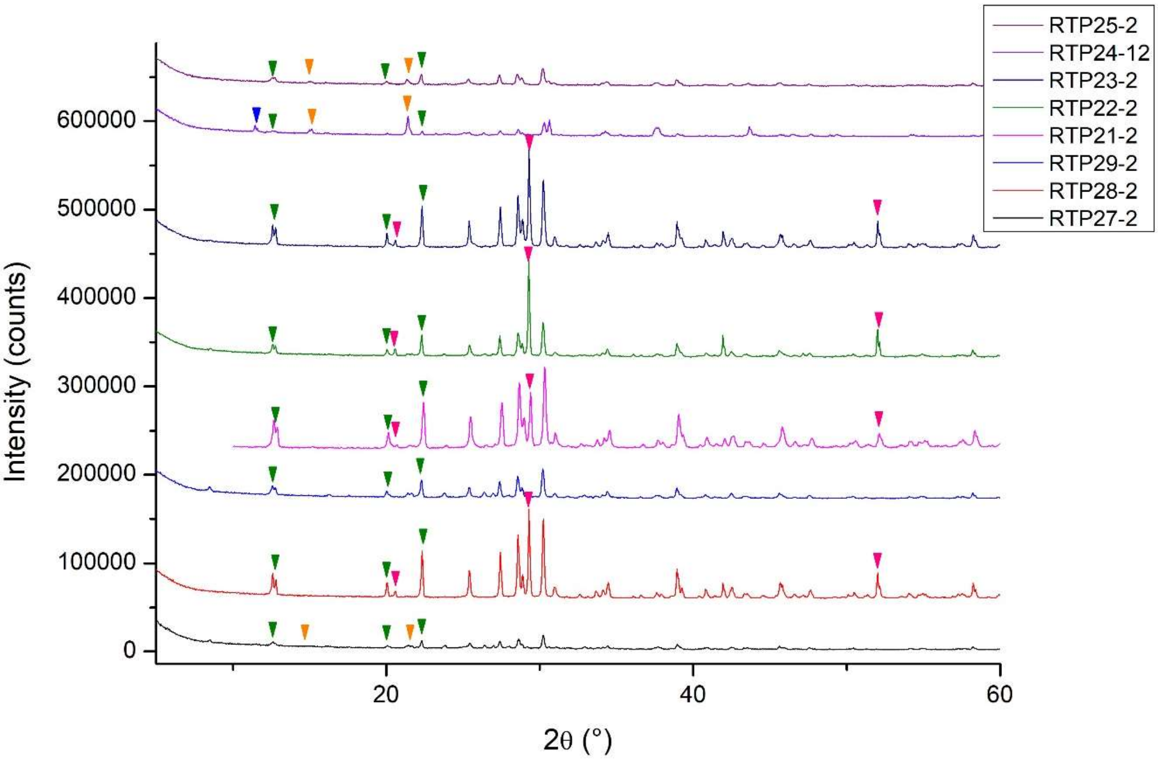

Figure 67. Diffractograms of samples RTPx-2 (between 5° and 60°) obtained in order to study the influence of the reaction time over the final products. In the picture the different compounds have been identified with coloured triangles: orange corresponds to $CsPbBr_3$, blue to $CsPb_2Br_5$, green to Cs_4PbBr_6 and magenta to CsBr.

It can be observed that these diffractograms are slightly more reproducible as they all present the same peaks ascribable to the Cs_4PbBr_6 structure. Nevertheless, some of the samples also present the $CsPbBr_3$ phase and in one of them (RTP24-12) the $CsPb_2Br_5$ can also be identified. Lastly, part of these sample present CsBr or the unknown compound or both.

The variability observed in these two groups of samples, produced in order to study the influence of the reaction time over the final product, may be attributed to the fact that they have been washed with different methods, since the standard procedure described in Paragraph 3.2.1.2 was developed through a series of trials operated on these same samples.

3.2.2.1.3 Amount of citric acid

In order to determine how the amount of citric acid influences the final product, some samples have been obtained and studied. Table 8 highlights the compounds detected in each of these samples. As was specified for the other tables, the samples that remained at the bottom of the flask after the purification process are denoted with the RTPx-1 acronym. Instead, RTPx-2 samples are the solids left in the beaker.

Table 8. Summary of the phases detected in each sample analysed during the study on the amount of citric acid.

Sample	**Phases detected from the diffractogram**				
	$CsPbBr_3$	***$CsPb_2Br_5$***	***Cs_4PbBr_6***	***CsBr***	***Unidentified***
RTP36-11 ($CA/Pb(OAc)_2 = 0$)	---	---	---	---	---
RTP36-12 ($CA/Pb(OAc)_2 = 0$)	---	---	---	---	---
RTP37-1 ($CA/Pb(OAc)_2 = 1{,}0$)			x	x	x
RTP37-2 ($CA/Pb(OAc)_2 = 1{,}0$)			x	x	x
RTP38-1 ($CA/Pb(OAc)_2 = 2{,}5$)	x	x	x	x	x
RTP38-2 ($CA/Pb(OAc)_2 = 2{,}5$)			x	x	x
RTP43-1 ($CA/Pb(OAc)_2 = 4{,}0$)	x		x	x	x
RTP43-2 ($CA/Pb(OAc)_2 = 4{,}0$)	x		x	x	x
RTP44-1 ($CA/Pb(OAc)_2 = 5{,}5$)	x	x	x	x	x
RTP44-2 ($CA/Pb(OAc)_2 = 5{,}5$)			x	x	
RTP45-1 ($CA/Pb(OAc)_2 = 7{,}0$)	x		x		x
RTP45-2 ($CA/Pb(OAc)_2 = 7{,}0$)	x		x		x
RTP42-1 ($CA/Pb(OAc)_2 = 8{,}6$)	x		x	x	x
RTP42-2 ($CA/Pb(OAc)_2 = 8{,}6$)	x		x	x	x
RTP41-1 ($CA/Pb(OAc)_2 = 10{,}0$)	x	x	x		x
RTP41-2 ($CA/Pb(OAc)_2 = 10{,}0$)	x		x	x	x

This table does not include the data referred to samples RTP36-1 and RTP36-2 because the obtained solid appears to be highly hygroscopic. Such solid is white and it might be some caesium bromide that did not react to form perovskites. The other samples are ordered by increasing amounts of citric acid in the sample.

The table shows that all the analysed samples contain the Cs_4PbBr_6 phase and that almost all of them present the peaks attributed to the unknown compound. The other impurity, CsBr, is not present in some of the samples that contain a higher amount of citric acid (RTP45-1, RTP45-2 and RTP41-1). Lastly, the other two perovskite structure are not as regularly distributed. $CsPbBr_3$ can be detected in most of the samples, both in the RTPx-1 and the RTPx-2 samples and the solids where this phase cannot be identified are the ones characterized by lower amounts of citric acid (RTP37-1, RTP37-2, RTP38-2 and RTP44-2). Structures ascribable to the $CsPb_2Br_5$ phase are rarely found and the only three samples where they can be identified are of the RTPx-1 type.

The comparison between the diffractograms of the RTPx-1 samples is shown in Figure 68, while the one for RTPx-2 is shown in Figure 69.

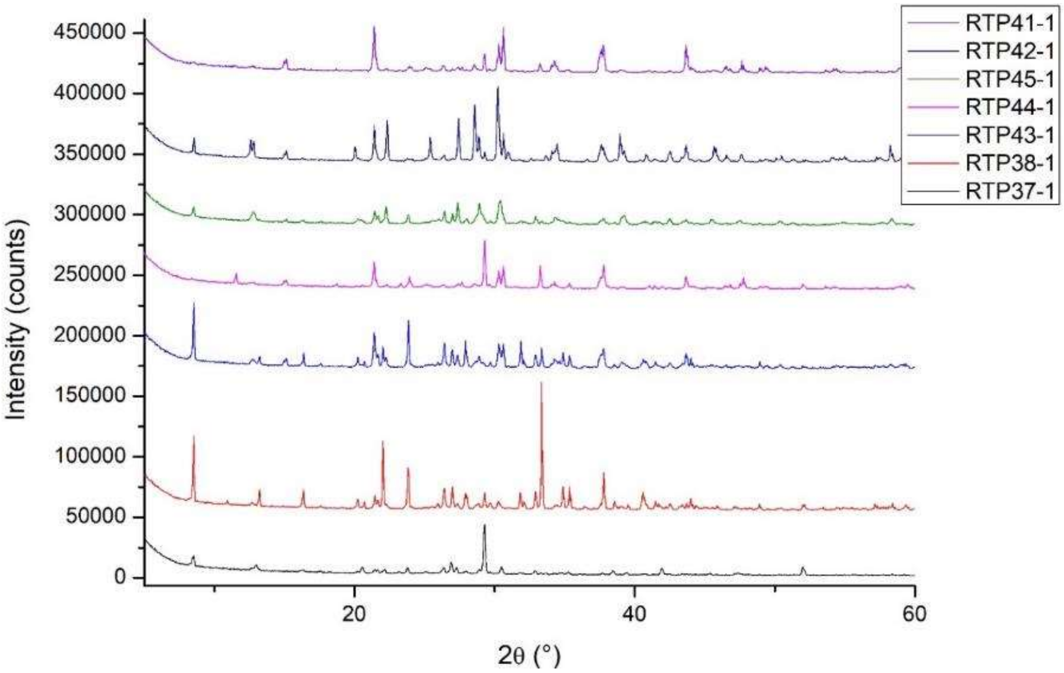

Figure 68. Diffractograms of samples RTPx-1 (between 5° and 60°) obtained in order to study the influence of the amount of citric acid over the final products.

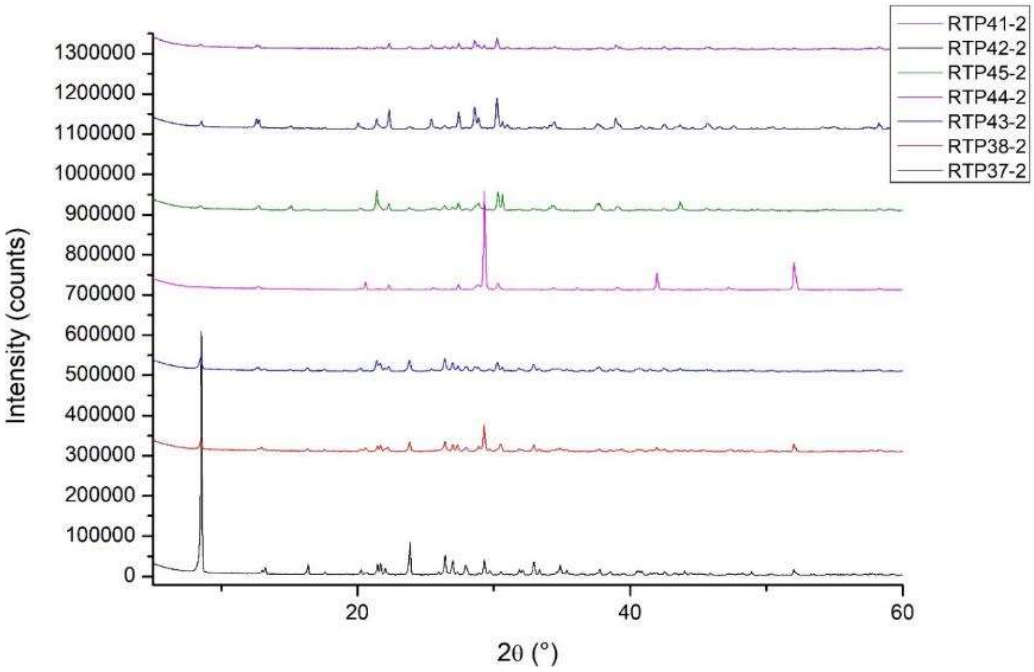

Figure 69. Diffractograms of samples RTPx-2 (between 5° and 60°) obtained in order to study the influence of the amount of citric acid over the final products.

Figure 70 shows the collected diffractogram of samples RTPx-1 in the range 5° - 25°, evidencing the assigned crystallographic phases: they are denoted by symbols of different colours (orange: $CsPbBr_3$; blue: $CsPb_2Br_5$; green: Cs_4PbBr_6; magenta: CsBr).

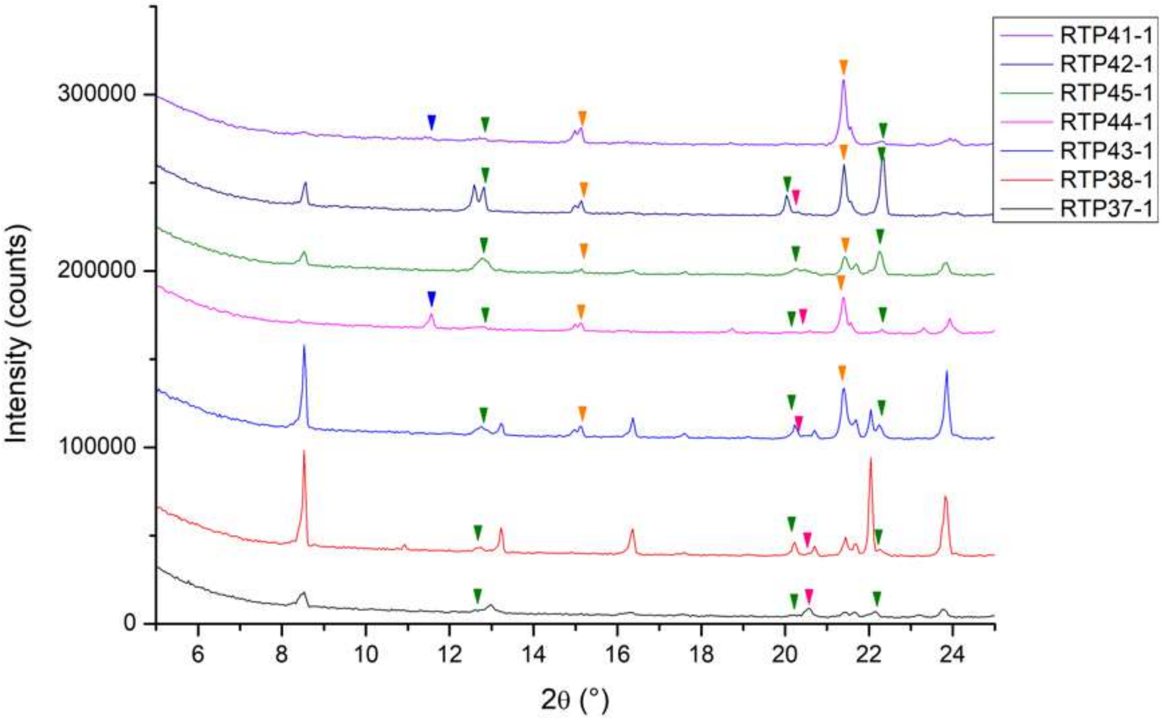

Figure 70. Diffractograms of samples RTPx-1 obtained in order to study the influence of the amount of citric acid over the final products, restricted to the region 5° – 25 °. In the picture the different compounds have been identified with coloured triangles: orange corresponds to $CsPbBr_3$, blue to $CsPb_2Br_5$, green to Cs_4PbBr_6 and magenta to CsBr.

As is evident from the figure, the samples do not have many similarities, since both the peaks position and their intensities are quite different. All the samples show a peak at 8,52° which was attributed to the unknown compound. The intensity of this peak seems to diminish in relation to an increase in the amount of citric acid added during the synthesis. This observation is denied by samples RTP37-1 and RTP44-1, where the considered peak results less intense than what would be anticipated. Another compound that can be observed in all the reported diffractograms is the Cs_4PbBr_6 perovskite phase (green triangles), but once again, the intensity of the corresponding peaks does not appear to follow a pattern. The $CsPbBr_3$ structure (orange triangles) has been identified in the solids that contain a higher amount of citric acid ($CA/Pb(OAc)_2 > 2{,}5$). Next, only two samples present the $CsPb_2Br_5$ phase (blue triangles), but they do not have similar characteristics; the first (RTP44-1) has a medium amount of citric acid, while the second (RTP41-1) contains the highest amount of citric acid. Lastly, caesium bromide (magenta triangles) can be observed in some samples and the ones that do not present its peaks contain higher quantities of citric acid.

The diffractograms relative to the second group of samples (RTPx-2) are shown in Figure 71.

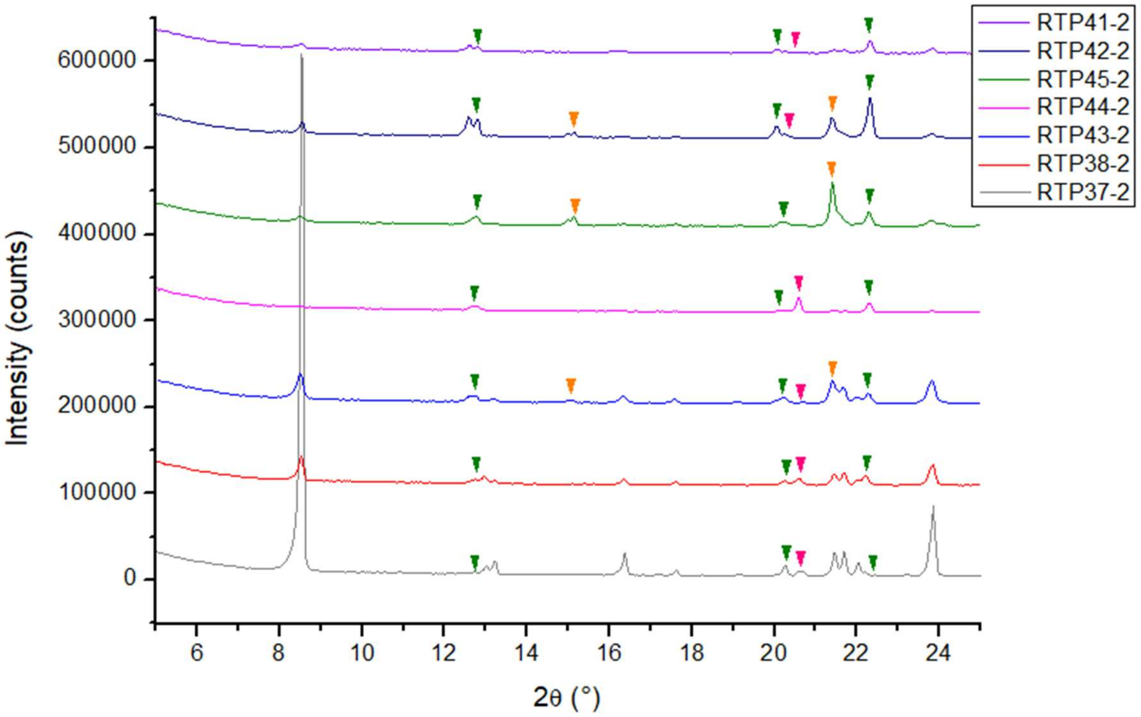

Figure 71. Diffractograms of samples RTPx-2 obtained in order to study the influence of the amount of citric acid over the final products, restricted to the region 5° – 25 °. In the picture the different compounds have been identified with coloured triangles: orange corresponds to $CsPbBr_3$, green to Cs_4PbBr_6 and magenta to CsBr.

The RTPx-2 samples are not very different from the RTPx-1 one that have just been described in the sense that a clear patter cannot be evidenced and that they all present peaks ascribable to the unknown compound (beside RTP44-2) and to the Cs_4PbBr_6 perovskite structure. Differently from the RTPx-1 samples, caesium bromide can also be found in almost all the samples. Of the other two perovskite phases, only $CsPbBr_3$ has been observed and it is present only in the diffractograms of three samples containing an intermediate amount of citric acid.

3.2.2.2 Scanning electron microscopy

In preparation to the SEM and EDS characterization the solids have been dispersed in ethanol through sonication. It has been observed that this solvent does not completely disperse the samples and part of them often stays on the bottom of the vial.

SEM characterization reflects what has been observed from the X-ray diffraction data and a variety of morphologies and sizes can be observed in accord to the presence of multiple phases and compounds in the same sample. In general, the shapes that can be often identified in the analysed samples are cubic, hexagonal and spheric, but most nanocrystals do not present well defined shapes and some of the samples also present other morphologies that are not as frequent as the cited ones. Figure 72 includes some representative samples containing each shape.

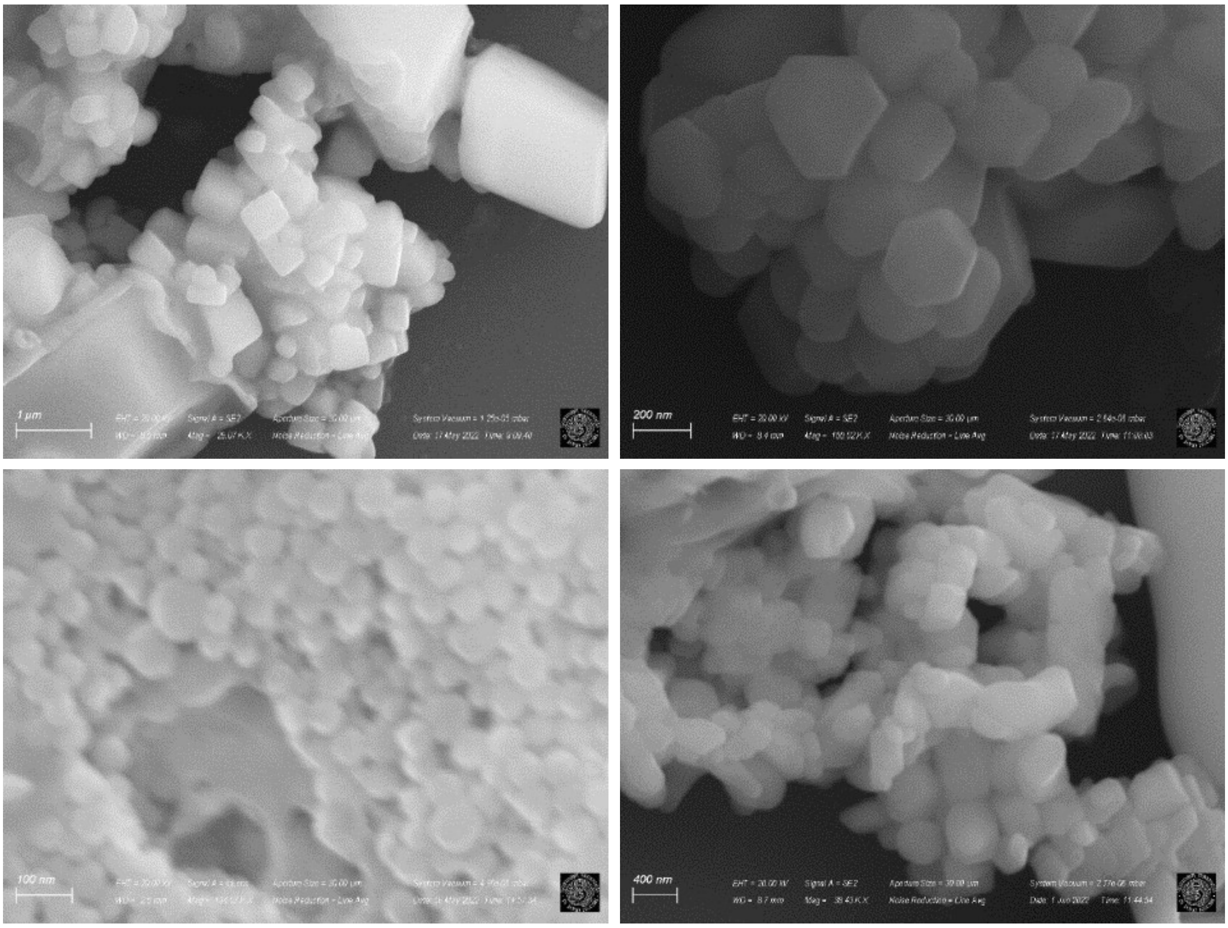

Figure 72. Examples of cubic crystals from sample RTP21-2 (top left), hexagonal crystals from sample RTP27-1 (top right), spheric crystals from sample RTP26-1 (bottom left) and a not-defined shape from sample RTP41-2 (bottom right).

It is possible to hypothesise which shape belongs to which perovskite phase thanks to the observations reported by de Weerd et al. [70]. The cubic nanocrystals are probably the $CsPbBr_3$ nanoperovskites, as was also determined in the previous experimental section (Paragraph 3.1). Hexagons and spheres can be ascribable to the presence of the Cs_4PbBr_6 phase in the sample. As shown in the cited article, the pure Cs_4PbBr_6 phase assumes the first of these two shapes, while the combination of such a phase with $CsPbBr_3$ gives rise to spherical nanocrystals. This observation cannot however be used to unequivocally identify which perovskite phases are present in the sample. The analysed solids often contain other phases such as caesium bromide and an unknown compound and it is possible that one of these species have one of the same morphologies ascribable to perovskite nanocrystals. For instance, it has been observed through SEM analysis that RTP21-2 contains cubic crystals, but the X-ray diffraction characterization led to identify Cs_4PbBr_6 and CsBr as the only phases present in the sample. Consequently, caesium bromide may also have a cubic shape and the confirmation to this observation can only be done through EDS analysis. For example, sample RTP44-2 present two types of regular shapes (squares with rounded vertex and spheres), which have been identified as CsBr by means of EDS analysis. Figure 73 shows the image of this sample acquired through SEM analysis and Figure 74 reports the results of the EDS investigation of these two regularly shaped crystals.

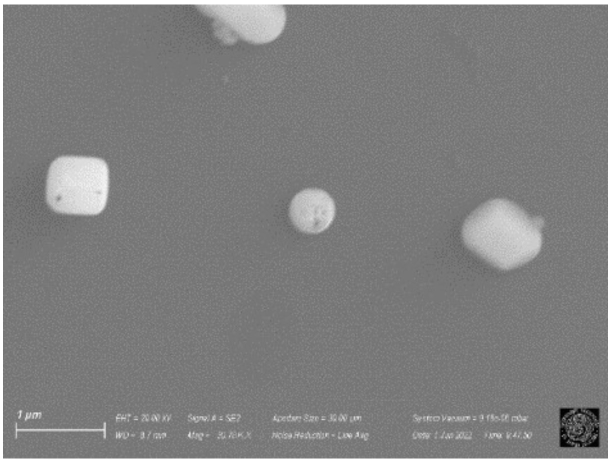

Figure 73. SEM image of sample RTP44-2.

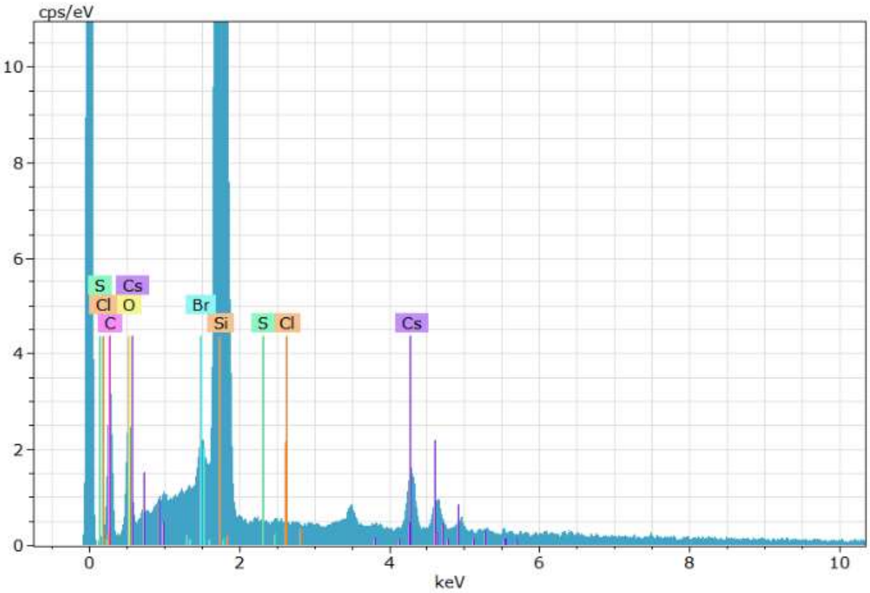

Figure 74. EDS report obtained for sample RTP44-2.

As can be seen from Figure 74, the most intense peak is the one attributed to silicon, which correspond to the support where the sample was deposited. Lead has not been detected, while caesium and bromine present relatively high peaks. Consequently, it has been concluded that these regular shapes cannot be associated with perovskite nanocrystals, but rather with caesium bromide.
In the following paragraphs some representative samples are going to be discussed, but only some SEM images will be reported. The other images can be observed in the appendix (Paragraph 6.2)

3.2.2.2.1 Reaction temperature

First samples RTP13-2, RTP14-2 AND RTP18-1 will be discussed, since they all present the same phases detected from the diffractograms. We expect to observe the hexagonal crystals ascribable to Cs_4PbBr_6 and the regular shapes associated with caesium bromide. Sample RTP14-2 also present the unknown compound, so a morphology uniquely present in this sample may be identified as that compound itself.
Sample RTP13-2 shows crystals with cubic shapes characterized by a variety of sizes. These crystals have been identified as perovskite phases through EDS analysis. Spheres are also present, and they are identifiable as CsBr. Sample RTP14-2 presents a greater variety compared to RTP13-2 and all these structures can be distinguished in Figure 75.

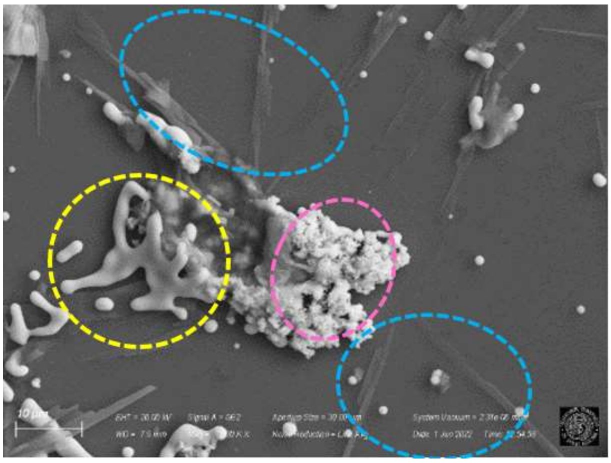

Figure 75. SEM image of sample RTP14-2.

Crystals with non-regular shapes (circled in pink) can be recognized, along with a substance that does not possess a well-defined morphology (circled in yellow) and another compound with a more transparent aspect (circled in light blue). The latter can be associated with the unknown compound, since it has not been detected in any other of the three analysed samples. Its shape can be seen as an array of needle-like structures and its composition mainly consist of caesium as verified by means of EDS. On the other hand, the one possessing an unclear morphology corresponds to an excess of citric acid.

The nanocrystals observed in sample RTP18-1 are more similar, but they still present a variety of shapes. This sample presents cubic, hexagonal and spherical crystals, which can be associated with the perovskite phase. The identification of the perovskite phases has been conducted through EDS, as reported in Figure 76.

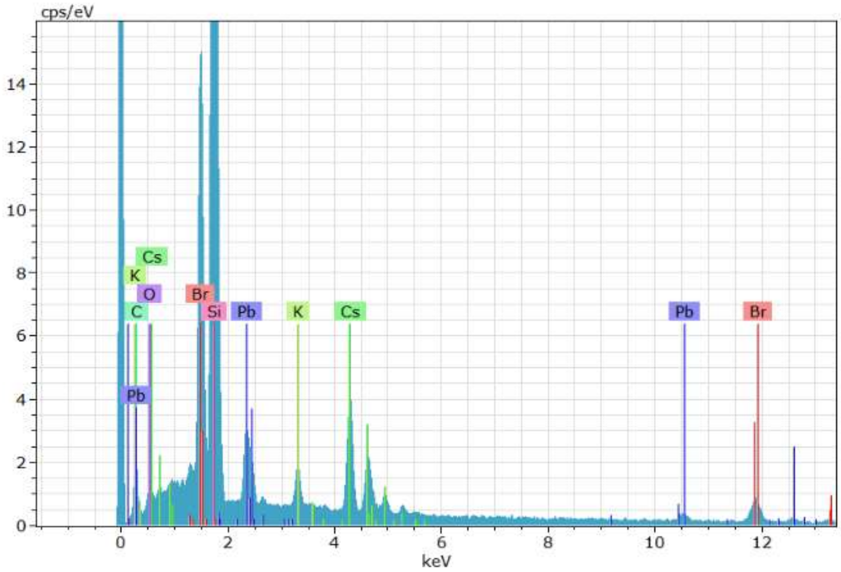

Figure 76. EDS report obtained for sample RTP18-1.

Contrarily to what has been observed in the EDS report previously reported for the identification of CsBr, lead has also been detected in this sample, leading to conclude that the analysed crystals can be attributed to perovskite phases.

In general, the comparison between the SEM images acquired for these three samples shows that multiple morphologies can be identified even in a single sample. The hexagonal nanocrystals expected for Cs_4PbBr_6 have only been observed in sample RTP18-1, while all three samples contain cubic crystals even if their diffractograms do not present peaks associated to the $CsPbBr_3$ phase. Figure 77 reports a micrograph obtained from sample RTP15-1, where the nanocrystals seem to form a bigger cubic shape.

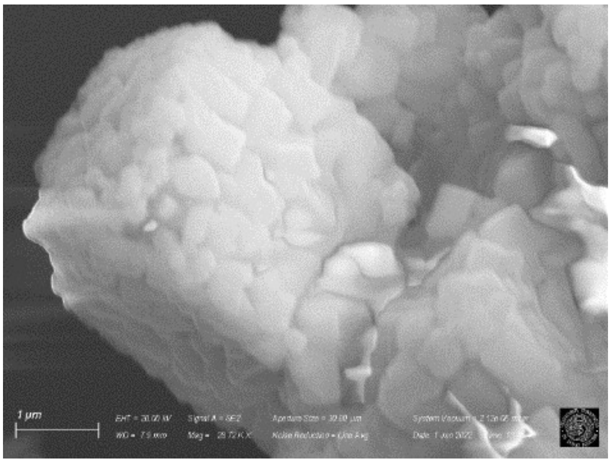

Figure 77. SEM image of sample RTP15-1.

Figure 78 reports two representative images of sample RTP18-2, which is made of $CsPbBr_3$ perovskite phase (along with caesium bromide).

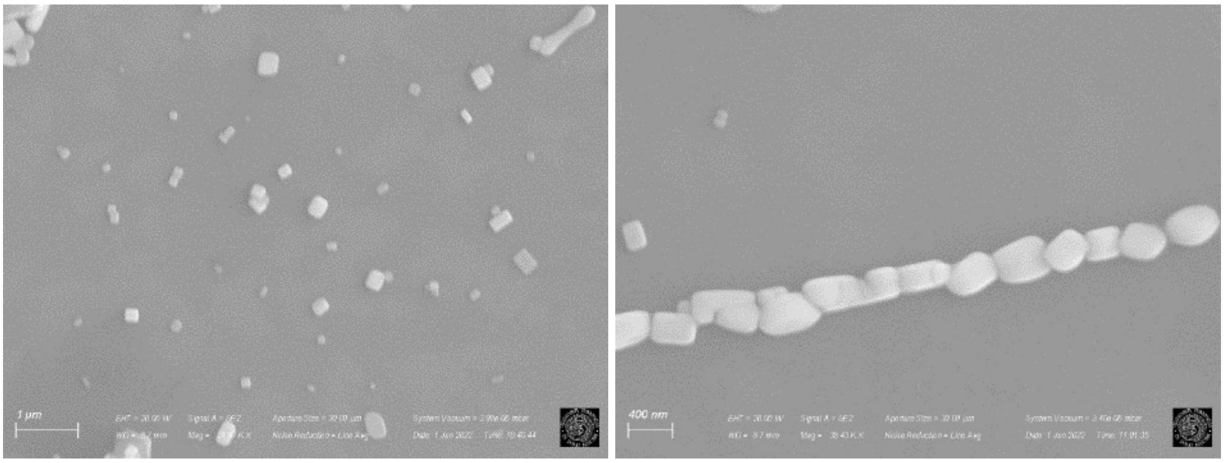

Figure 78. SEM images of sample RTP18-2.

As expected, this sample present the cubic nanocrystals ascribable to $CsPbBr_3$ and the regular squared shapes associable with CsBr.

3.2.2.2.2 Reaction time

Three samples were characterized in order to investigate the effect of the reaction time on morphology. Samples obtained at a reaction time of 0, 15 and 60 minutes are here discussed, starting from sample RTP27-2 (0 min). The X-ray analysis revealed that this sample contains two perovskite phases, $CsPbBr_3$ and Cs_4PbBr_6, and the unknown compound. The images acquired during the SEM characterization are in agreement to what has been reported by the fore-mentioned article, where hexagonal shapes are attributed to Cs_4PbBr_6, cubic shapes to $CsPbBr_3$ and spherical ones to a hybridization of the two phases [70]. SEM images of the perovskite nanostructures are reported in Figure 79.

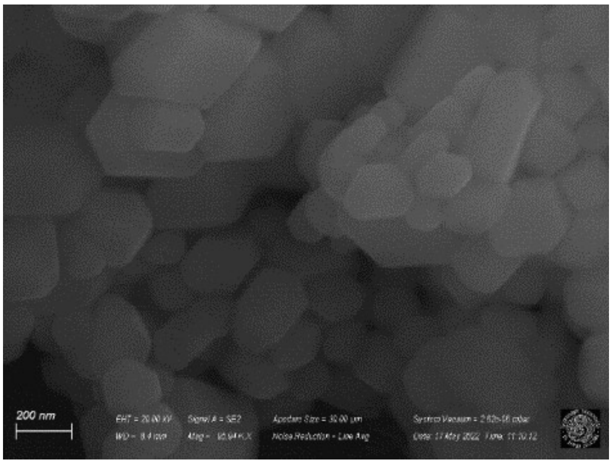

Figure 79. SEM image of sample RTP27-2.

The shapes in these pictures are mainly hexagonal and, following the previously explained observation, they may be attributed to the Cs_4PbBr_6 phase. However, some parallelepipeds can also be observed and they could be seen as cubic structures that did not grow the same way along all directions. These may correspond to the $CsPbBr_3$ phase. Spheres have also been observed in the samples. These may confirm the presence of a hybridization between $CsPbBr_3$ and Cs_4PbBr_6. Beside the three perovskite phases, this sample also contains the unknow compound and, in accordance with what has been described for sample RTP14-2, this specie can be ascribed to the almost transparent structure observed. Such structure has bigger dimensions compared to the nanocrystals that have been identified as perovskite phases and, once again, it seems to be composed of an array of needle-like structures. In this case as well, the EDS analysis determined that their composition mostly consists of caesium.

At a slightly longer reaction time (15 min) only the Cs_4PbBr_6 phase and CsBr have been identified from the diffractograms of the sample RTP21-2. However, the SEM images show cubic, hexagonal and non-defined shapes and these crystals also present very different dimensions. Finally, the last sample obtained at a higher reaction time is RTP24-12 and its diffractogram shows some peaks ascribable to all three perovskite phases ($CsPbBr_3$, $CsPb_2Br_5$, Cs_4PbBr_6). In the acquired images most of the nanocrystals present irregular shapes, but hexagons and cubes can also be identified. All of these structures are relatively small, in accordance with the fact that no compound can be detected in the X-ray analysis beside the three perovskite phases. A characteristic phenomenon in this sample is the aggregation of these small crystals to form long and narrow structures. Such elongated structures can be seen in Figure 80.

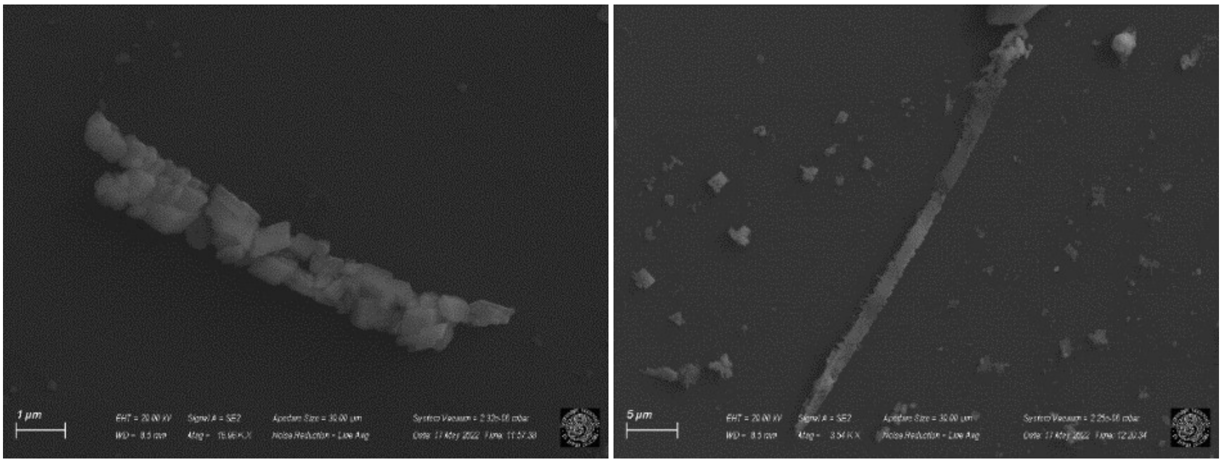

Figure 80. SEM images of sample RTP24-12.

This aggregation cannot be observed in sample RTP24-11 (Figure 81), so it might be a consequence of the removal of some capped citric acid that was avoiding the assembling of the formed perovskite nanocrystals.

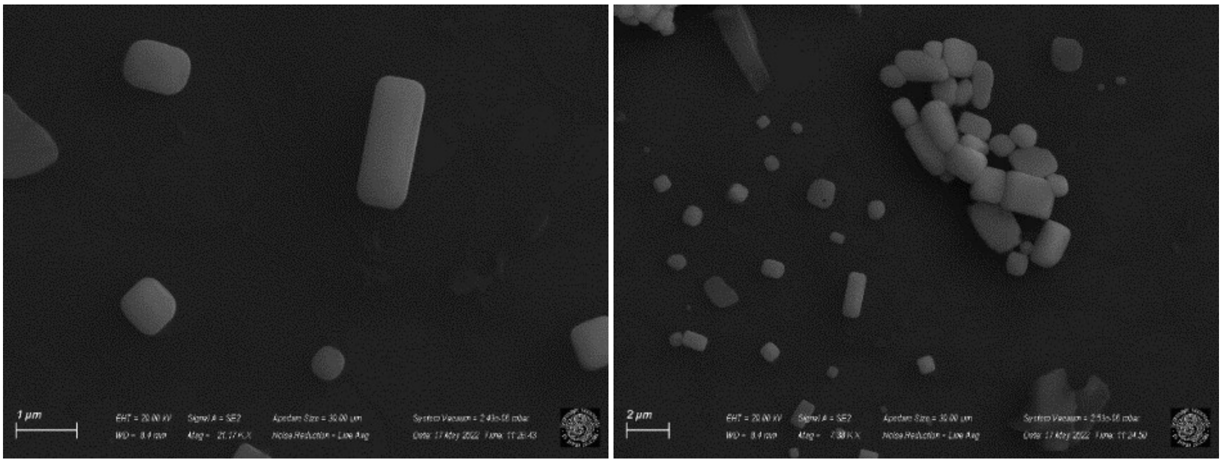

Figure 81. SEM images of sample 24-11.

3.2.2.2.3 Amount of citric acid

Three of the samples have been characterized in this group, two at the extremes (RTP37-2, with one of the lowest quantity of CA, and RTP41-2, with the highest amount of CA) and one containing a medium amount of citric acid (RTP44-2). Even if the X-ray analysis indicates that the sample are quite similar, since they all present common phases, their aspect observed at the scanning electron microscope is not that comparable. As a reminder, all these three samples present Cs_4PbBr_6, CsBr and the unknown compound, beside RTP44-2 that only contains the first two cited compounds. Despite not presenting a distinct patter, some observations are in accordance with the amount of citric acid that was added in each sample. RTP37-2 is characterized by a CA/$Pb(OAc)_2$ ratio of about 1, so the formation of perovskite structures is expected in a very limited quantity. Its SEM images are reported in Figure 82.

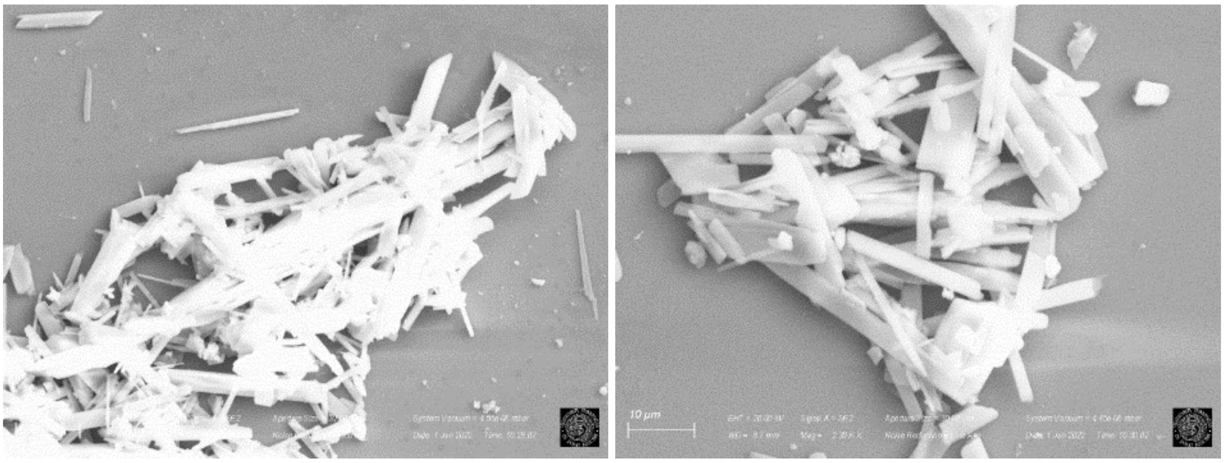

Figure 82. SEM images of sample RTP37-2.

It can be observed that most structures have big dimensions and present a rod-like morphology. These may be attribute to the CsBr contained in the sample, which is expected to be present in bigger amount compared to samples where a bigger quantity of citric acid is added. Smaller structures are present too, but their exact shape cannot be identified. From the EDS analysis of this sample no nanocrystals ascribable to perovskite phases have been identified.

On the other extremity there is sample RTP41-2, characterized by the highest amount of citric acid (CA/$Pb(OAc)_2 \approx 10$). The crystals observed in the images of this sample have variable sizes and most of them do not present a well-defined shape. It is possible that they constitute a mixture of perovskite nanostructures and caesium bromide, where the second compound would correspond to the bigger species. These structures are not the only ones that can be observed in this sample. The following figure (Figure 83) shows two other images acquired during the SEM analysis.

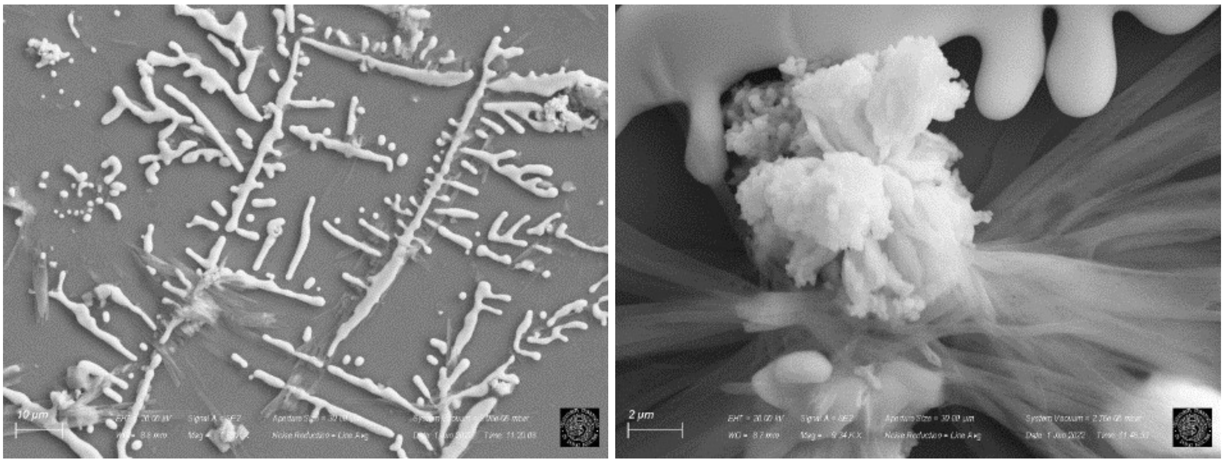

Figure 83. SEM images of sample 41-2.

The picture on the left may represent the excess of citric acid that can be expected considering that it was added in such a high quantity. On some portions of the same picture, beside the almost liquid-looking compound, an almost transparent structure can be identified. This same structure can be better observed in the picture on the left, where its colour, more transparent than the other compound present, is highlighted. This second structure could be ascribed to the unknown compound, as its characteristics are the same as observed in samples RTP14-2 and RTP27-2.

Lastly, sample RTP44-2, including a medium amount of citric acid, was characterized. As expected, the SEM analysis did not lead to the identification of structures that may be attributed to an excess of this compound. The sample mostly contains two types of species, the ones with regular shapes (generally squares with smoothed out vertexes) and the ones with a not-defined morphology. The second ones can probably be identified as the perovskite phase Cs_4PbBr_6, while the first one might be caesium bromide.

In conclusion, the group of samples used to rationalize the influence of the amount of citric acid on the final products is the only one where some type of pattern can be distinguished. It is possible to identify where an excess of citric acid is present from the SEM images. Furthermore, the lack of this compound as well as a too small quantity of it is evidenced by the formation of a very limited amount of perovskite structures. The detection of caesium bromide in sample RTP37-2 as the only observed compound can in fact prove the importance of citric acid in the formation of perovskite nanocrystals.

3.2.2.3 Photoluminescence and photoluminescence excitation spectroscopy

The orange solid, obtained after the solid left from the evaporation of the supernatant dried, leaves a lighter orange and a light-yellow powder in the flask after washing them with acetone and these powders present an intense green emission under a UV light of 365 nm (Figure 84).

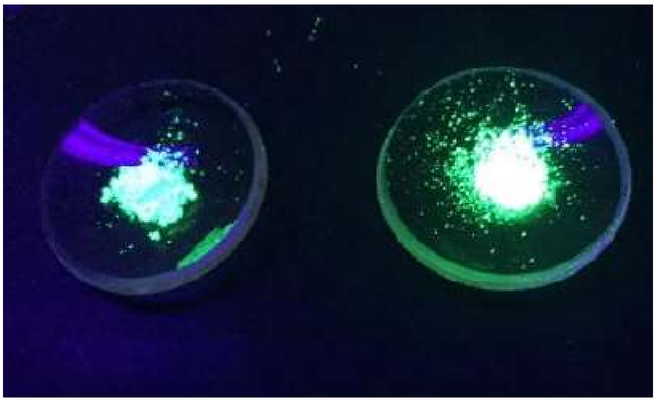

Figure 84. Emission observed under a UV light (365 nm) for the darker (left) and the lighter (right) solids.

In order to study this emission, photoluminescence spectroscopy investigations have been conducted. In preparation to this analysis, the samples were dispersed in acetone. All the intensities of the spectra reported in this section were normalised. Only the emission features of some representative samples from each of the three groups (reaction temperature, reaction time and amount of citric acid) are going to be studied. Before discussing the comparison between spectra belonging to samples of the same group, some observations are necessary. Some of the characterized solids contain in fact more than one perovskite phase, as demonstrated through X-ray diffraction, and all three of them might be photoluminescent since there are some controversies on the topic throughout scientific works. Sample RTP24-12 was first analysed because its diffractogram allowed to determine that all three perovskite structures can be detected in the sample and none of the two impurities are present. Figure 85 shows the photoluminescence (at 330 nm) and photoluminescence excitation (at 590 nm) spectra of this sample.

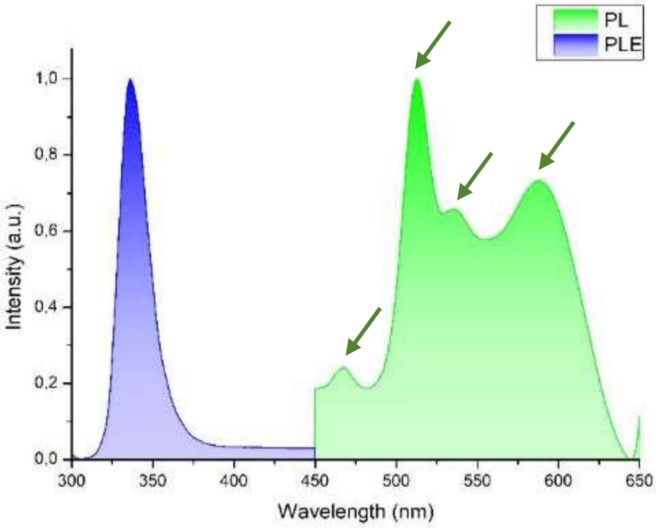

Figure 85. Blue: PLE spectrum of sample RTP24-12 acquired at 590 nm. Green: PL spectrum of sample RTP24-12 acquired at 330 nm.

The PLE spectrum presents one main narrow peak centred at 336 nm, while in the PL spectrum four peaks can be identified, as indicated by the arrows in the picture. The compound responsible for the smaller peak at 468 nm was not identified. The other three peaks could be assigned to the three perovskite phases. In particular, the ones at 513 nm and at 536 nm can be isolated when changing the excitation wavelength. In Figure 86 two spectra are reported, the one on the left was excited with a radiation of 380 nm and the one on the right with one at a wavelength of 300 nm.

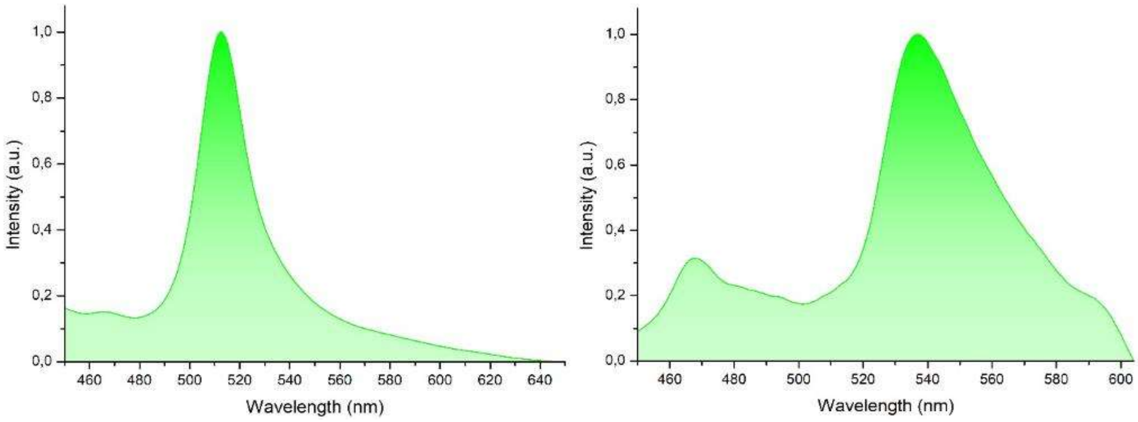

Figure 86. Left: PL spectrum of sample 24-12 acquired at 380 nm. Right: PL spectrum of sample RTP24-12 acquired at 300 nm.

It is possible to determine which of the peaks corresponds to the Cs_4PbBr_6 phase by comparing the photoluminescence spectrum with the one of a sample that only contains this perovskite phase. With this aim, the PL (at 350 nm) and PLE (at 515 nm) spectra of sample RTP42-2 are reported in Figure 87.

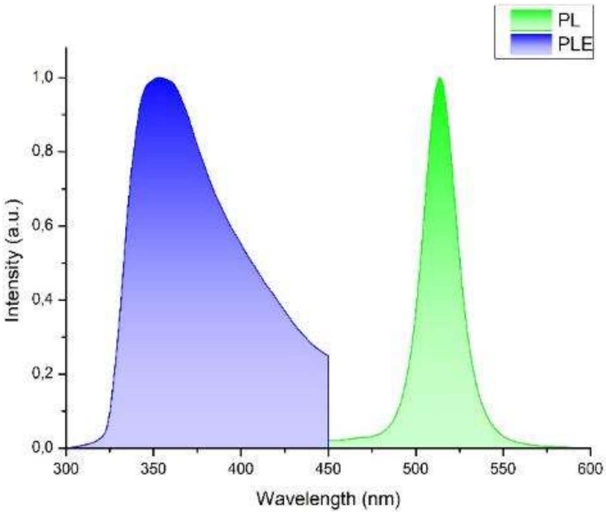

Figure 87. Blue: PLE spectrum of sample RTP42-2 acquired at 590 nm. Green: PL spectrum of sample RTP42-2 acquired at 330 nm.

In this sample, the maximum of the PLE spectrum is centred at 353 nm and its shape is less narrow, compared to the one observed for the PLE spectrum of RTP24-12. In the PL spectra only one peak (514 nm) is present, and it can be attributed to the Cs_4PbBr_6 structure, since it is the only one detected by X-ray diffraction.

The second sample characterized in order to assign the remaining peaks to a specific perovskite phase is RTP18-2. Its diffractogram only presents signals ascribable to the $CsPbBr_3$ phase, but, since the characterization has been conducted in acetone, it is possible that this phase might partially convert to the Cs_4PbBr_6 one. The PL spectra, detected with an incident radiation of 380 nm (left) and of 300 nm (right) can be observed in Figure 88.

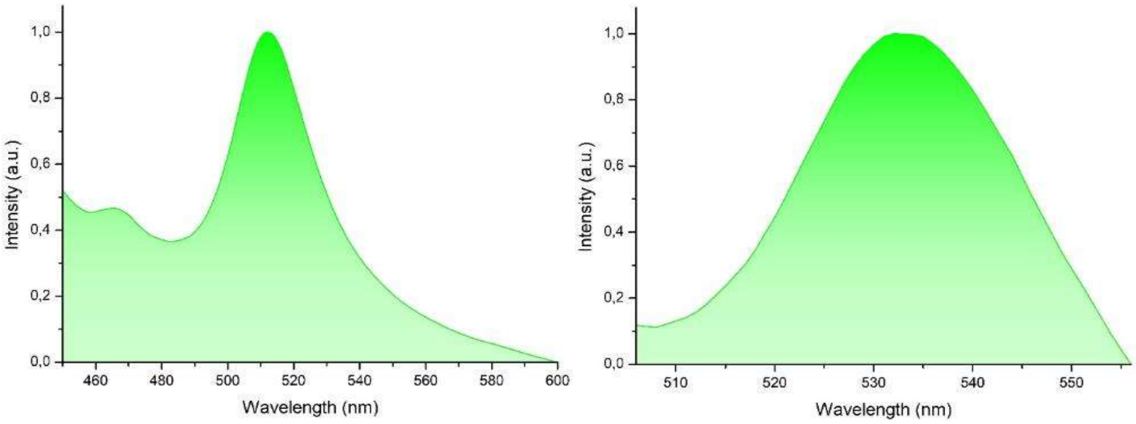

Figure 88. Left: PL spectrum of sample 18-2 acquired at 380 nm. Right: PL spectrum of sample RTP18-2 acquired at 300 nm.

These PL spectra represent the isolated peaks observed in sample RTP18-2. As discussed for sample RTP44-2, the one at 512 nm can be attributed to the Cs_4PbBr_6 phase. Consequently, the second peak (534 nm) is to be assigned to $CsPbBr_3$.

By elimination, in the spectrum of sample RTP24-12 the last peak at 587 nm is due to the presence of the $CsPb_2Br_5$ phase in the sample and this is in accordance with the fact that no other characterized sample shows a signal at this wavelength and these samples do not have the characteristic peaks of $CsPb_2Br_5$ in the diffractogram.

Taking into consideration these observations, some of the other spectra are going to be discussed in the following paragraphs divided into the three main groups (reaction temperature, reaction time and amount of citric acid). The comparison between the intensity of the analysed peaks will not be discussed, since they do not seem to follow a pattern. The spectra that are not showed in this section can be observed in the appendix (Paragraph 6.3).

3.2.2.3.1 Reaction temperature

The representative samples chosen to represent the reactions of this group are RTP13-2, RTP15-2 and RTP17-2 because they give an idea of the characteristics of the product obtained at low, medium and high temperature respectively. All the PLE spectra at 515 nm of these three samples present a maximum at 347 - 350 nm and they have superimposable peaks shape-wise. The PL spectra are also very similar both regarding their shape and to the position of the peak. The comparison of these PL spectra acquired with an excitation radiation of 350 nm is reported in figure 89.

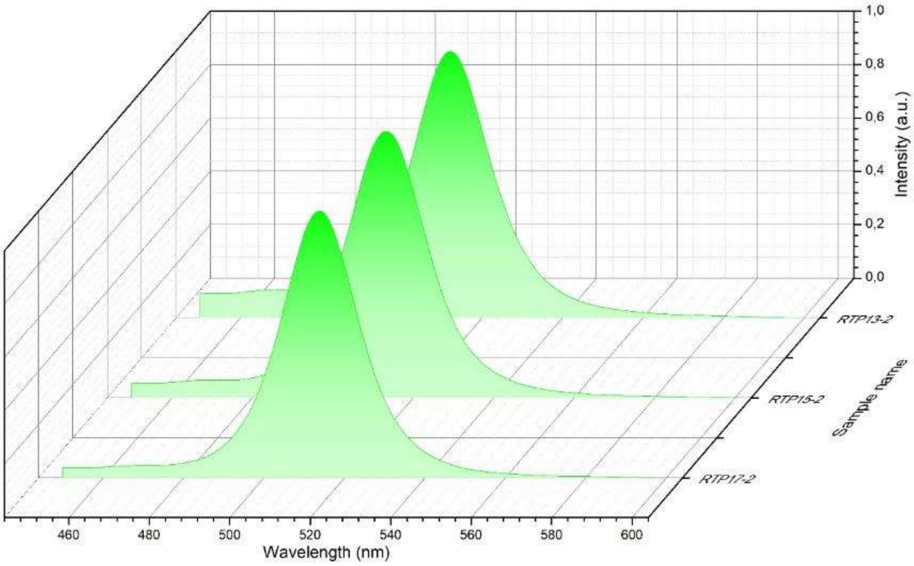

Figure 89. Comparison between the PL spectra of samples RTP13-2, RTP15-2 and RTP17-2, acquired at 350 nm.

They all present one main peak centred at 513 nm, corresponding to the Cs_4PbBr_6 phase. This confirms the identification of this phase as the only one present in the diffractogram of these samples.

3.2.2.3.2 Reaction time

In this group RTP27-2, RTP21-2 and RTP24-12 are discussed as representative of short, medium and long reaction times respectively. The PLE spectra at 515 nm of these three samples present a maximum at about 348 – 350 nm and, once again, their shapes are quite similar, with a tail toward higher wavelengths. On the other hand, the PL spectra are compared in Figure 90.

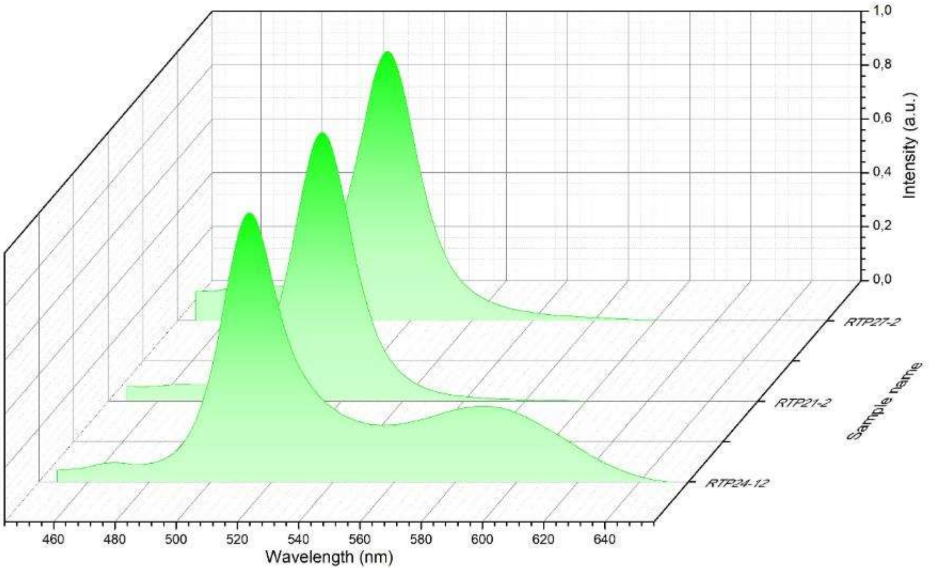

Figure 90. Comparison between the PL spectra of samples RTP27-2, RTP21-2 and RTP24-12, acquired at 350 nm.

The photoluminescence spectrum of sample RTP24-12 presents some differences from the other two and such differences are ascribable to the presence of more than one perovskite phase, as explained before. Nevertheless, its peak at 513 nm is similar to the ones present in the other two samples at the same wavelength value. The width of the peaks in the spectra of RTP27-2 and RTP21-2 is narrower than the one relative to the same peak in the RTP24-12 spectrum, but this might be caused by the presence of the $CsPbBr_3$ in the latter whose peak is located closely to the one of the Cs_4PbBr_6 phase.

3.2.2.3.3 Amount of citric acid

Lastly, the photoluminescence and photoluminescence excitation spectra of three samples containing three different quantities of citric acid are discussed. RTP38-2, RTP43-2 and RTP41-2 represent the sample with the lowest to highest amount of citric acid. In this group of samples, the PLE spectra are very similar both for their shapes and for the position of their maximum. Their peak presents a tail on the right side and its maximum is centred between 347 and 352 nm. The PL spectra are also very similar, and their comparison is shown in Figure 91.

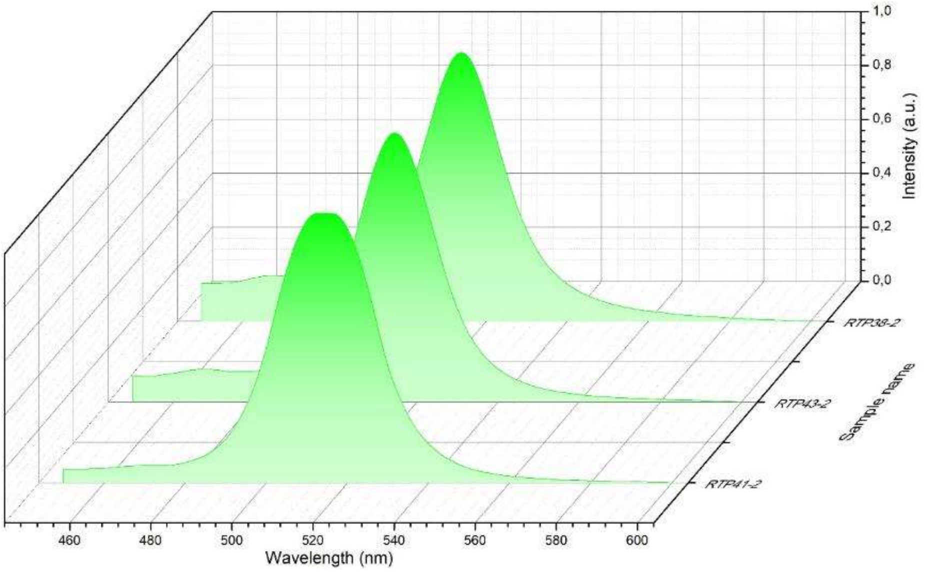

Figure 91. Comparison between the PL spectra of samples RTP38-2, RTP43-2 and RTP41-2, acquired at 350 nm.

The only peak present is positioned at 514 nm and it is narrow in all the specimens. Among these three samples, the one with a slightly larger width is the one pertaining to sample RTP41-2.

3.2.2.4 Infrared spectroscopy

Infrared spectroscopy has been used to study the role of citric acid in the material. A coordination of such compound on the surface of nanocrystals would in fact determine a shift of some characteristic peaks in the spectrum with respect to the position of such peaks in the spectrum of the free compound. This considered, the infrared spectra of pure citric acid and of one of the obtained samples (RTP21-2) have been acquired through Fourier-transform infrared spectroscopy (FTIR). The comparison between these two spectra is reported in Figure 92.

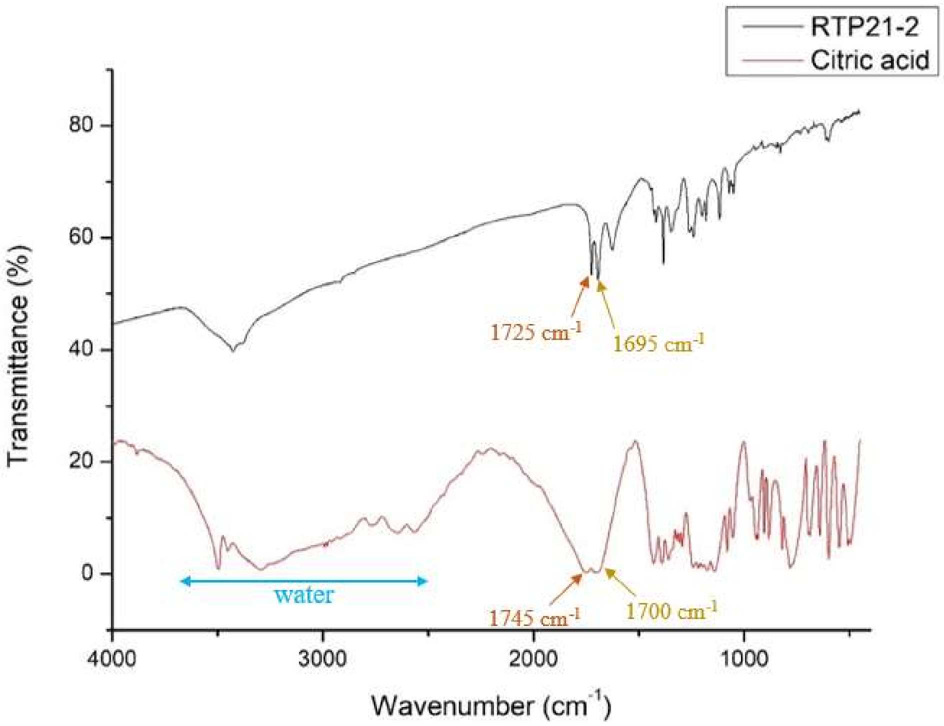

Figure 92. Infrared spectra of sample RTP21-2 (black) and of pure citric acid (red).

As expected, the spectrum of citric acid (red in Figure 92) presents a signal characteristic of the hydroxyl group at higher wavenumbers (about 3500 cm^{-1}) and the broad band in this same region, from 2500 cm^{-1} to 3500 cm^{-1} is probably ascribable to water since citric acid is hygroscopic. This band probably covers the signals relative to the CH_2 stretching, which should appear at 3140 cm^{-1}, but they should not be particularly interesting, since we expect the coordination to involve the carboxylic groups rather than the CH_2 portions. This molecule possesses, in fact, three carboxylic groups, whose C=O stretching is centred at 1680 – 1750 cm^{-1}. In the acquired spectrum this band is split into two signals at about 1745 cm^{-1} and 1700 cm^{-1}, corresponding to the C=O stretching of the central and lateral carboxylic groups respectively. Other signals characteristic of the carboxylic groups generally fall in the region between 1500 and 1800 cm^{-1}; for example, in this part of the spectrum the symmetrical stretching of COOH and the in-plane bending of OH should be observed. After this group of signals, the C–OH stretching can be identified at about 1130 cm^{-1} and the bendings of C–OH and COOH can be observed at lower wavenumbers (685 cm^{-1} and 560 cm^{-1} respectively). The identification of the main bands in an IR spectrum of citric acid has been conducted following the observations of Lavarda et al. and Zampieri et al. [71; 72]. Focusing on the central signals, corresponding to the carboxylic groups, a variation in the wavenumber can be observed, but the peak remains split. In particular, the two signals in the spectrum of sample RTP21-2 are positioned at 1725 cm^{-1} and 1695 cm^{-1}, so the variation is more significant for the first one of these peaks.

Nevertheless, in the reaction medium caesium acetate was added before the end of the reaction, so the carboxylic group of the acetate portion might also present peaks in the IR spectrum, and it cannot be easily confirmed that the ones observed are not ascribable to this second compound.

3.2.3 Discussion

Because of the formation of lead citrate, a certain amount of lead cations is incorporated into this compound and, consequently, do not form the desired perovskite material. Moreover, the fact that some of the white solids identified with lead citrate present a weak green emission under UV light (365 nm) leads to think that a small part of the desired product crystallizes on such precipitate. Lead citrate should not form in an acid environment, but the solution pH tends to increase slightly right after adding the aqueous solution of caesium acetate and the acetate itself may bring to the citrate formation. The interaction between citric acid and acetate is schematically represented in Figure 93.

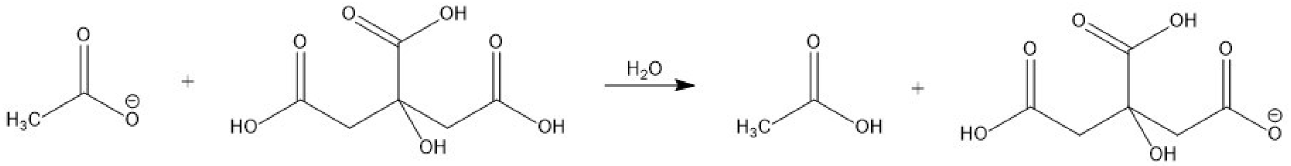

Figure 93. Interaction between citric acid and acetate in the aqueous solution.

In order to verify the solution conditions, the pH was roughly determined through the use of the litmus paper and it has been observed that right after adding the second precursor the pH shifts about one unit higher. A more precise pH determination is needed in order to determine the ideal pH value to avoid the formation of this by-product.

As can be seen from the X-Ray analysis of all the samples described in this chapter, a variety of phases is obtained and, at times, these phases cannot be easily separated. It is relevant to note that the Cs_4PbBr_6 phase is always present in the RTPx-2 type samples and can be found in some of the RTPx-1 samples too. On the other hand, the $CsPbBr_3$ and $CsPb_2Br_5$ structures are generally detected only in the RTPx-1 samples. Figure 94 summarizes the presence of a particular phase in the RTPx-1 and RTPx-2 samples with the purpose of highlighting which perovskite phases prevails.

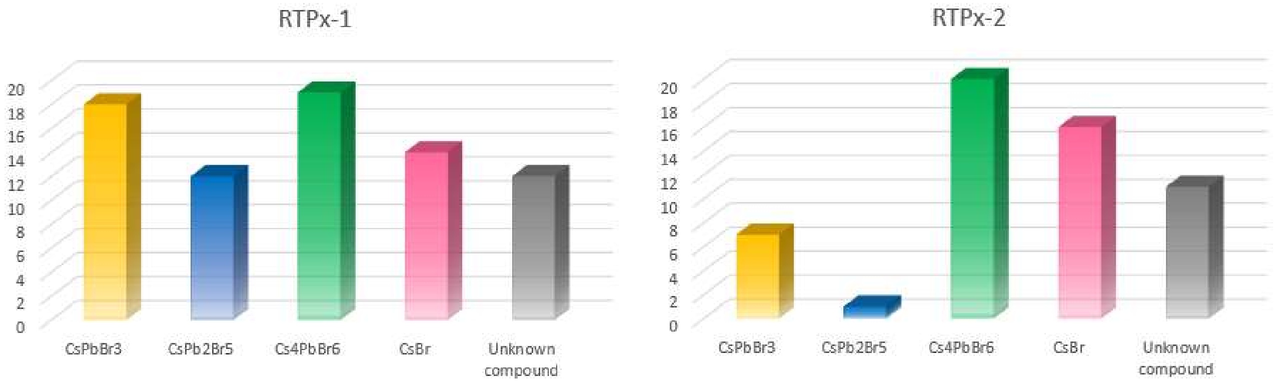

Figure 94. Distribution of the different structures that have been detected in the two distinc groups of samples.

As can be observed from the figure, the predominant phase is Cs_4PbBr_6, which has been detected in both type of samples (39 out of 42 samples contain this perovskite nanostructure and RTP18-2 was mainly composed of this phase as well before it was dispersed in water). It can be assumed that at first the $CsPb_2Br_5$ perovskites are formed and that these gradually convert into $CsPbBr_3$ and then into Cs_4PbBr_6 during the washing steps. As explained in Paragraphs 2.2.3.3 and 2.4.4, the presence of water favours the $CsPb_2Br_5$ structure, which forms in polar mediums through the removal of CsBr from $CsPbBr_3$ and this second phase can in turn form from Cs_4PbBr_6 when CsBr is removed in a polar solvent [42]. During the evaporation of the solvent and the washing process with acetone, water is removed, and it is possible that the conversion is reverted, leading to the formation of $CsPbBr_3$ and then of $Cs4PbBr_6$. Consequently, the presence of caesium bromide is expected in the samples where $CsPbBr_3$ and $CsPb_2Br_5$ structures are detected, since it has not been included in the structure to form Cs_4PbBr_6 yet. However, this halide salt was also found in samples where the only detected perovskite phase was the one rich in caesium, such as RTP29. This leads to think that CsBr is present in the initial solution in excess so, even if all the perovskite structures have been converted into Cs_4PbBr_6, a certain amount of caesium bromide is still available. This excess of caesium bromide is in accordance with the fact that part of the lead cations, present in the reaction mixture, react with citric acid to form lead citrate monohydrate, so they are not available to react with the caesium precursor to form perovskite nanocrystals. Caesium bromide in not the only impurity detected in the sample. An unknown compound has been observed and, while its composition was not determined through X-ray diffraction analysis, the EDS results reported that this second by-product is also mainly composed of caesium.

Considering the high variability in the samples analysed through X-ray diffraction and taking into consideration that no distinctive pattern was found, more than one explanation can be hypothesised. First of all, the influence of moisture, which has been clearly observed in the stage after the supernatant was evaporated, might be more important than expected. Since the drying of the obtained solid was conducted at ambient conditions, no control over the amount of moisture interacting with it was applied and this led to different results. While the samples washed during the period when the humidity level was lower always changed from a white solid to a dark orange one in two days at maximum after it was left to dry, the ones elaborated in more humid days required more time to achieve this colour variation and some of them (RTP36, RTP38, RTP44 and RTP45) never became dark orange; moreover, water was found in the flask of these four samples along with the white solid after three days. This parameter is particularly important because of the influence water has on the preferential structure formed, as has been explained. A second explanation is attributable to the fact that the separation and washing processes are not optimized; the washing step does not allow to remove non-perovskite phases, as can be seen from the presence of caesium bromide and of an unknown compound in some of the samples. Moreover, the separation between the three detected perovskite structures is not ideal, seeing as the chosen solvent for this purification phase (acetone) does not dissolve completely one of these phases or leave another completely precipitated on the bottom. A solvent in which the three phases have very different solubilities has not been found, since they seem to be insoluble in both the nonpolar and the polar solvents that were tested. Between these solvents, water is not included since its use leads to a phase change and it would not be possible to obtain the Cs_4PbBr_6 structure anymore (as was observed for the dispersion test in water conducted for sample RTP18-2). Lastly, the influence of all these parameters in the post-synthetic phase might be more crucial than the impact of the parameters that have been varied during the reaction, such as time and temperature. It might be hypothesized that at the end of the synthetic process the perovskite structures are not formed yet and only an aqueous solution of the precursors is obtained or only complexes involving lead or caesium cations were formed. After evaporating the solvent, the obtained white solid might contain a series of salts that have not reacted with each other due to the presence of citric acid. Acetone might remove part of the excess of citric acid, allowing the reaction between the precursors to happen and leading to the actual formation of different perovskite structures. An example where acetone was used to start the nucleation and growth stages was reported [73]. In this paper, the explanation to acetone's role in the formation of perovskite nanocrystals has been given and experimental analysis allowed to demonstrate that the desired nanocrystals do not form before its addition. Acetone probably destabilizes the complexes that lead(II) and caesium(I) have formed with the other species present in the reaction medium. This mechanism is reported in Figure 95.

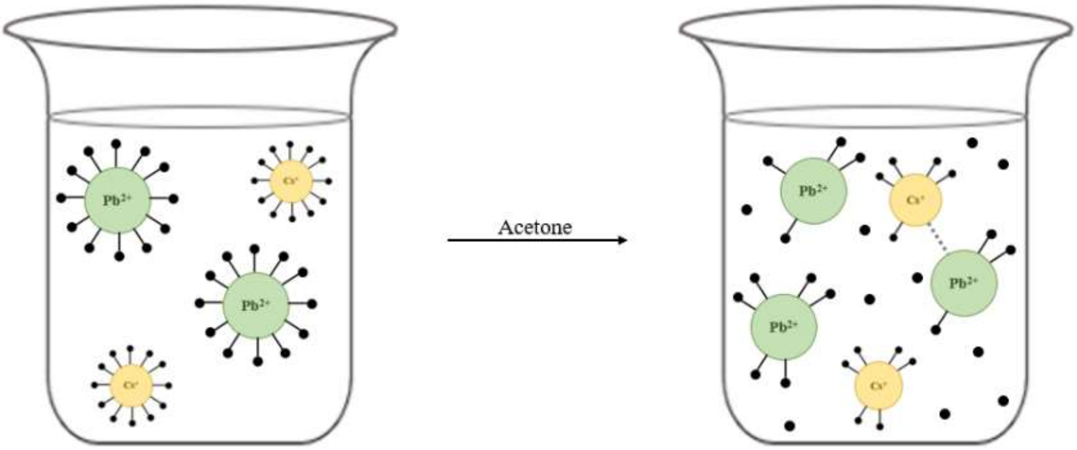

Figure 95. Representation of the effect that acetone has in the reaction medium.

The presence of a variety of species in both the RTPx-1 and the RTPx-2 samples has been observed both by X-ray diffraction and by scanning electron microscopy. The latter techniques coupled with energy-dispersive X-ray spectroscopy showed, in fact, that some of the crystals observed in the samples do not contain lead and consequently allowed to distinguish between perovskite structures and caesium bromide. Moreover, the SEM analysis led to the identification of a variety of morphologies and sizes that do not appear to follow a patter in the three groups studied. This may be a consequence of the beforementioned factors (the influence of moisture during the post-synthetic reaction or the possibility of the perovskite nanocrystals' formation happening after the evaporation of the supernatant obtained at the end of the synthetic process). However, another reason may be listed in order to explain such irregularity. The only compound that has been added that might act as a capping ligand is citric acid and a second type of ligand might be necessary. Consequently, an amine should be added to provide a capping ligand that may better control the final aspect of the product. If perovskite nanocrystals form during the synthetic process, this additional compound should ideally be introduced into the reaction medium before the introduction of caesium acetate or together with this precursor. On the other hand, the amine should be added to the compound during or right before the washing phase if it is demonstrated that perovskites do not form before this step.

Despite not highlighting a particular pattern in the three analysed groups of samples, the characterization conducted through scanning electron microscopy helped determine the importance of citric acid in this synthetic approach. It was observed that the reaction conducted without the addition of citric acid (RTP36) probably does not lead to the formation of perovskite structures, since the obtained solid at the end of the washing process appears highly hygroscopic, similarly to caesium bromide. Moreover, the SEM analysis of sample RTP37-2 (containing a CA/$Pb(OAc)_2$ ratio of 1) allowed to observe that this solid is mostly made up of caesium bromide since the EDS analysis did not identify structures where lead was detected along with caesium and bromine. The gradual increase of citric acid in the reaction medium led to the formation of perovskite structures that could be observed and identified through the coupling of SEM and EDS, until the amount of this compound was so large that an excess could be noted in the SEM images (RTP41-2).

The morphologic and dimensional characterization was then followed by an examination of the nanomaterials optical properties, focusing on their emission. As described in Paragraph 2.4.4, there is no uniform opinion over the photoluminescence of the Cs_4PbBr_6 perovskite phase. Briefly, it has been stated that an emission should not be observed since the band gap of this compound is too wide. In Figure 96, a comparison between the band structure calculated for each of the three perovskite phases is reported.

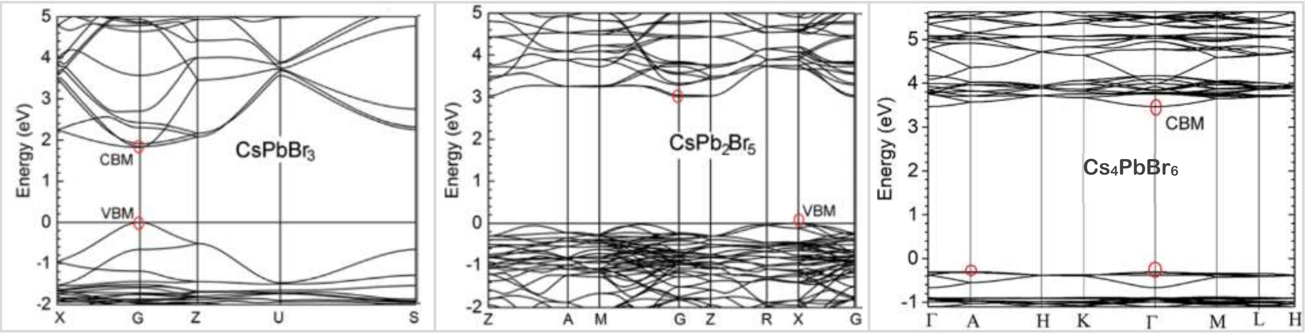

Figure 96. Comparison between the band structure of $CsPbBr_3$ (left), $CsPb_2Br_5$ (centre) and Cs_4PbBr_6 (right). The first two pictures are reported from [74] and the one on the right from [75].

As can be observed, the difference between the band gaps of $CsPbBr_3$ and Cs_4PbBr_6 is very significant, so it is expected that only the first of these two perovskite structures can present an emission. Nonetheless, the analysis presented in this work shows that samples where only the Cs_4PbBr_6 perovskite structure is present show an emission, with a peak centred at 513 – 514 nm. This might be explained considering that the reaction has been carried out in water or it might be another consequence of the influence of moisture over the obtained solids. In fact, it has been shown that hydroxyl groups, introduced in the sample through water addition, can modify the band gap and can drastically change the photoluminescence of the Cs_4PbBr_6 phase [56]. In the cited article, it has been demonstrated that, while pure Cs_4PbBr_6 nanocrystals do not have a green emission, the addition of different amounts of water in the analysed solution leads to a degree of photoluminescence that increases along with the growth of water content until a certain volume after which this parameter starts diminishing. In accordance with the fact that the luminescence observed in samples containing both Cs_4PbBr_6 and $CsPbBr_3$ is lower than the one observed for exclusively Cs_4PbBr_6, the article proves that the presence of this second phase does not appear to be linked to the increase of emission intensity [56]. Moreover, this research group states that the hydroxyl effect is not limited to the addition of water, but also to the addition of ethanol and of a solution of sodium hydroxide [56]. The influence of the different hydroxyl groups on the band structure has also been represented by the cited article and is reported in Figure 97.

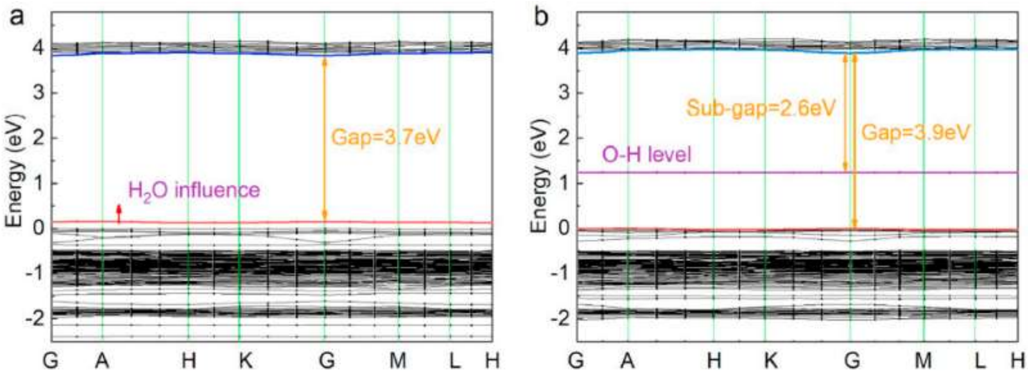

Figure 97. Band structure of Cs$_4$PbBr$_6$ perovskite nanocrystals influenced by the presence of water (a) or other types of OH group (b) [56].

This is relevant to this thesis because at first the measurements of photoluminescence and photoluminescence excitation have been conducted on ethanol solutions of the samples. This led to a considerable variability in the photoluminescence spectra acquired for sample characterized after being dispersed in ethanol for 20 minutes or 24 hours. Figure 98 reports the photoluminescence spectra acquired at 350 nm of a series of samples.

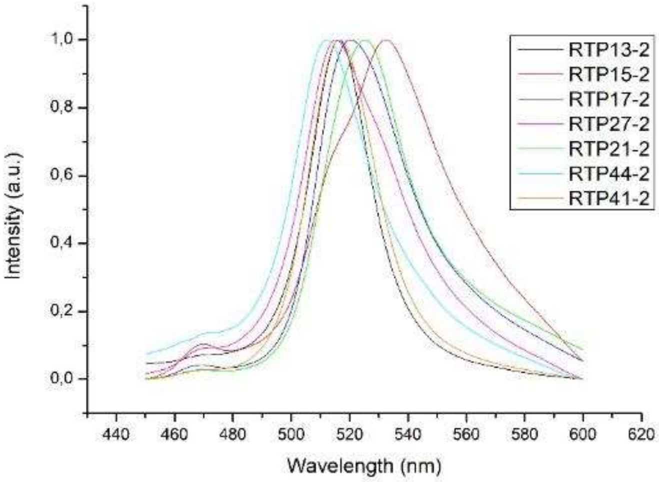

Figure 98. Comparison of the PL spectra at 350 nm of samples: RTP13-2, RTP15-2, RTP17-2, RTP27-2, RTP21-2, RTP44-2 and RTP41-2.

A shift toward higher wavelengths can be seen for samples that have spent more time in ethanol, indicating a decrease in the band gap.

Beside the emission observed for the Cs_4PbBr_6 phase, two other peaks have been identified in the PL spectrum of samples containing all three the perovskite structures, such as sample RTP24-12. By comparing these peaks to the ones observed in the samples only containing the Cs_4PbBr_6 phase or only the $CsPbBr_3$ it was possible to deduce that the peak centred at about 534 nm is ascribable to $CsPbBr_3$ and the one positioned at about 587 nm can be attributed to $CsPb_2Br_5$. The position of the three peaks is not in accordance with the band gap observed for these three phases. Since $CsPbBr_3$ has the lowest band gap, it should be positioned at higher wavelengths compared to both the other phases. However, the peak identified with the $CsPb_2Br_5$ phase falls at higher wavelengths with respect to the other two. This might indicate that the emission in the $CsPb_2Br_5$ structure is dictated by the presence of defects. The participation of defects in the emission of all the perovskite phases detected also justifies the big Stokes shift that can be observed in all the acquired spectra. As a case in point, the PLE (at 590 nm) and the PL (at 330 nm) spectra of sample RTP24-12 are reported in Figure 99. The characterization conducted through X-ray diffraction allowed to determine that this sample contains all three perovskite phases.

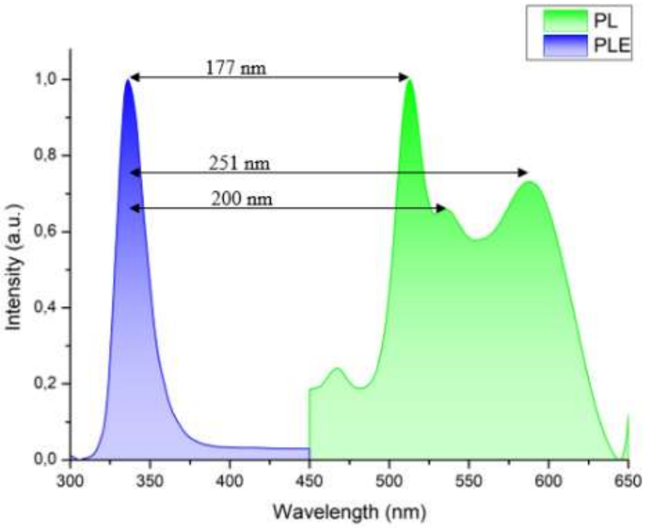

Figure 99. PLE (at 590 nm) and PL (at 330 nm) spectra of sample RTP24-12 where Stokes shift are highlighted.

As it can be observed from the figure, the difference between the excitation maxima and the emission maxima is significant and cannot be explained with an emission phenomenon that does not involve an intermediate state formed due to the presence of defects in the structure.

The influence of a defect state in the emission of the three different phases is schematically represented in Figure 100.

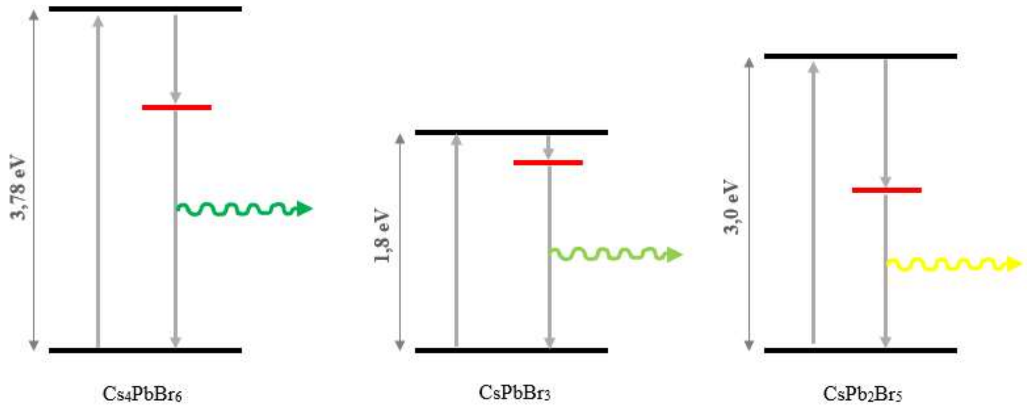

Figure 100. Comparison between the emission of the three different perovskite phases. The values reported for each band gap were calculated in [74; 75].

The last investigation was carried out by means of infrared spectroscopy. As previously mentioned, the aim of this characterization was the detection of a coordination of citric acid to establish if this compound acts as a capping ligand for the perovskite nanocrystals. The coordination is expected between the carboxyl groups and the nanocrystals, so the analysis was mostly focused on the region of the spectrum between 1500 and 1800 cm^{-1}, where the signal ascribable to the C=O stretching are generally centred. The main problem is that acetate is also present in the solution and this compound presents signals related to the C=O stretching too. Consequently, a coordination might be identified, but it cannot be confirmed that the coordinating specie is citric acid rather than the acetate anion.

Taking into account these results and the ones relative to the hot-injection procedure, the next paragraph will present the conclusive remarks of this thesis.

4. CONCLUSIONS

Two synthetic routes have been carried out in this work and both gave rise to perovskite nanocrystals. The first corresponds to the well-established hot-injection method, which allowed to obtain $CsPbCl_3$ perovskites characterized by regular morphologies and a restricted range of dimensions (compared to the second synthetic pathway discussed in this thesis). The procedure, followed to prepare the nanocrystals, was modified from the one reported by Gamelin et al. [66] and it was briefly studied as a starting point to then develop an improved approach. The hot-injection synthesis is in fact conducted at high temperature and inert atmosphere and this does not allow a facile scaling up of the process. A room temperature method was ideated and developed, aiming not only at improving the high temperature synthesis, but also at perfecting some aspects of the conventional room temperature techniques, such as the LARP and Emulsion LARP ones. To this purpose, the reaction medium was changed from dimethylformamide (or dimethyl sulfoxide) to water and the acidic component was switched from hydrobromic acid to citric acid, since ideally the latter can also act as a capping ligand, avoiding the need for additional compounds. To explore the main parameters that may influence the characteristics of the final product, three groups of reactions were carried out. First, the reaction temperature was studied by varying it in the range 20 – 70°C (samples RTP13 – RTP18). Then, the reaction time was taken into consideration through the modification of the time interval at which the reaction mixture was stirred right after the addition of caesium acetate (samples RTP21 – RTP29). Lastly, the amount of citric acid was gradually increased in samples RTP36 – RTP45 with the purpose of evaluating if different compositions could be detected in the final solid.

As demonstrated by the X-ray analysis, this new synthetic route led to the formation of perovskite nanocrystals; however, contrarily to what has been observed for the hot-injection method, more than one perovskite phase was detected. Both conventional $CsPbBr_3$ and lower-dimensional structures ($CsPb_2Br_5$ and Cs_4PbBr_6) were obtained and as explained, they were not easily separated, since they seem to present a similar solubility in all of the solvents that were tested. The predominant of these phases was however Cs_4PbBr_6, which was detected in the majority of samples. This result is significant since scientific articles generally focus on the preparation of conventional $CsPbBr_3$ nanocrystals and only obtain small quantities of Cs_4PbBr_6 as a by-product. The employment of water as a reaction medium should favour the production of the conventional or the $CsPb_2Br_5$ structures. Consequently, the use of citric acid in the synthesis or the washing steps with acetone could be responsible for the preferential formation of the Cs_4PbBr_6 nonconventional phase.

Beside the difficulties encountered in the separation of perovskite phases, the mentioned characterization also showed that impurities are sometimes present in the final product; indeed, caesium halide and an unknown compound were identified in the diffractograms of more than half of the obtained samples. This is a disadvantage, but it can be overcome by developing a better separation and washing processes compared to the ones used and described into this work. Furthermore, the presence of both impurities is probably linked to an excess of caesium in the solution, and this is due to the formation of lead citrate, which removes part of lead from the solution limiting its amount with respect to the second cation. Consequently, the problem could be solved by avoiding the formation of lead citrate and it has been observed that this can be achieved by using a different caesium precursor. In particular, the reaction has been repeated employing caesium chloride rather than caesium acetate and the solution did not turn cloudy after the addition of this precursor. The obtained product of this alternative procedure also shows an emission under the ultraviolet light with a wavelength of 365 nm, but such emission is intermediate between blue and green. The colour of this emission is expected, since the obtained nanocrystals are mixed halide perovskites, so they contain both the bromide and chloride anions which contribute together to the tuning of the emission. This sample produced by employing caesium chloride as a precursor should be further characterized to determine its composition, morphology and to better rationalize its emission.

A second issue that was evidenced during the characterization phase was related to the morphologies of the obtained nanocrystals. In all the analysed samples, more than one shape was observed by SEM analysis and a pattern in this variety of shapes was not found when observing the obtained samples by groups (for instance, by increasing the amount of citric acid or by increasing the reaction temperature). It might be possible to retain more control over the nanocrystals shape by introducing a second capping compound, such as an amine. The addition of this compounds could be operated directly in the lead solution with citric acid, or together with caesium acetate or again, during the washing steps with acetone. These hypotheses need further research and a variety of amines should be tested so as to determine which one gives the best results and how their length influences the final product. The presence of a second type of capping ligand might also improve the solubility of the perovskite phases in the sample and this could be an advantage in the separation stage, where none of the tested solvents were able to disperse the nanomaterials.

Both XRD and SEM characterizations did not highlight a pattern in the study of the reaction parameters and this variability might also be attributed to the fact that the actual reaction may occur after the addition of acetone in the steps denoted as “separation and purification”. Once again, this hypothesis needs to be proved by a more in-depth study of the reaction. The solution obtained at the end of the synthetic process as well as the solid produced after the evaporation of the solution by means of a rotavapor should be characterized to verify if perovskite phases can be detected.

The analysis of the emission of the obtained nanocrystals allowed to distinguish between the three perovskite phases, indicating that the peaks at 513, 534 and 587 nm in the PLE spectra (at 350 nm) belong to Cs_4PbBr_6, $CsPbBr_3$ and $CsPb_2Br_5$ respectively. On the other hand, the PL spectra allowed to conclude that all three of these emission phenomena probably involve an intermediate energy level formed due to the presence of defects. Such insight was brought by the observation of the wide Stokes shift present between the PL and the PLE spectra, which falls in the range 170 – 260 nm depending on the considered phase. Nevertheless, the emission mechanism should be more amply studied. In addition, the analysis of this optical property remains incomplete since the measurement of the photoluminescence quantum yields and of the lifetimes is also necessary to compare the efficiency of the perovskite phases' emission.

The investigation over the role of citric acid in the reaction did not lead to definitive results either. This compound is important for the dissolution of lead bromide in the solution, since the right amount of citric acid leads to a change in the aspect of the solution, which turns transparent starting from cloudy. Moreover, some characteristics of the final products might be attributed to its presence. The stability of the formed nanocrystals in atmospheric conditions without the need for further encapsulation and the impressing photoluminescence, which is possibly governed by the presence of hydroxyl groups, are two of those characteristics. However, while the infrared analysis showed a shift in the position of the carboxylic stretching with respect to the spectrum of pure citric acid, such variation is not conclusive. Indeed, caesium acetate has also been introduced in the solution and the carboxylic group of this compound might be responsible for the signals in the region 1680 – 1750 cm^{-1} of the spectrum as well.

Finally, the innovative room temperature method that has been discussed into this thesis needs improvements on a variety of aspects. Nevertheless, this synthetic pathway is promising since the obtainment of photoluminescent perovskite nanocrystals, while using water as a solvent, generally presents a series of issues. The instability to this solvent does not appear to be a problem for the synthesized nanocrystals, but its influence is still important especially when considering the dependence of their characteristics on environmental factors such as moisture. Another important result is the obtainment of stable nanocrystals at atmospheric conditions through this route. While it has frequently been reported that nanoperovskites undergo a degradation due to environmental factors (Paragraph 2.2.3.3), which leads to the deterioration of their optical properties, the products obtained through this innovative synthetic method do not present the same issue. The emission of sample RTP21-2 has been observed periodically for three months under an ultraviolet light at 365 nm and at the end of this time its luminescence did not seem to suffer from deterioration. This observation should be verified through the periodic measurement of the PLQY values, but it is an impressive result. Further studies should include the rationalization of the role of citric acid as a capping ligand and the evaluation of amines as a second group of capping ligands that may improve size and shape control. Moreover, the function of acetone should be unveiled to understand if it acts as a reaction starter or simply as a washing solvent. Regarding the washing stage, a different procedure should be defined with the purpose of removing the impurities and possibly isolating a single perovskite phase. The study of the optical properties should also be expanded, aiming at the production of an optoelectronic device. With this last purpose in mind, the possibility of including these nanomaterials in polymeric matrixes should be explored and tested. Lastly, the procedure should be repeated with different halide anions to evaluate if other perovskite compositions could be achieved. This would allow to expand the variety of emission wavelengths and might be useful for future optoelectronic applications. Another way to tune their photoluminescence properties would be through anion exchange reactions. These have already been partially tested by dispersing in ethanol a small amount of sample RTP21-2 and adding potassium chloride (KCl) or potassium iodide (KI). Figure 101 shows the emission of the obtained solutions.

Figure 101. On the left, the combination of sample RTP21-2 with KCl is shown, while on the right the combination of sample RTP21-2 with KI can be observed.

A blue emission was observed for the insertion of chloride anions in the perovskite phases and a red emission was observed for the insertion of iodide anions. Nevertheless, a more systematic study should be conducted including PL and PLE characterization of these solutions' emission.

5. *BIBLIOGRAPHY AND SITEOGRAPHY*

[1] S. Wang, A. A. Y. Amin, L. Wu, M. Cao, Q. Zhang, T. Ameri, Small Struct., 2021, 2 (2000124), 1 – 33

[2] A. Pan, B. He, X. Fan, Z. Liu, J. J. Urban, A. P. Alivisatos, L. He, Y. Liu, ACS Nano, 2016, 10, 7943 – 7954

[3] J. Shamsi, A. S. Urban, M. Imran, L. De Trizio, L. Manna, Chem. Rev., 2019, 119, 3296 – 3348

[4] A. A. M. Brown, B. Damodaran, L. Jiang, J. N. Tey, S. H. Pu, N. Mathews, S. G. Mhaisalkar, Adv. Energy Mater., 2020, 10 (2001349), 1 – 19

[5] A. Dey, J. Ye, A. De, E. Debroye, S. K. Ha, E. Bladt, A. S. Kshirsagar, Z. Wang, J. Yin, Y. Wang, L. N. Quan, F. Yan, M. Gao, X. Li, J. Shamsi, T. Debnath, M. Cao, M. A. Scheel, S. Kumar, J. A. Steele, M. Gerhard, L. Chouhan, K. Xu, X. Wu, Y. Li, Y. Zhang, A. Dutta, C. Han, I. Vincon, A. L. Rogach, A. Nag, A. Samanta, B. A. Korgel, C. Shih, D. R. Gamelin, D. H. Son, H. Zeng, H. Zhong, H. Sun, H. V. Demir, I. G. Scheblykin, I. Mora-Seró, J. K. Stolarczyk, J. Z. Zhang, J. Feldmann, J. Hofkens, J. M. Luther, J. Pérez-Prieto, L. Li, L. Manna, M. I. Bodnarchuk, M. V. Kovalenko, M. B. J. Roeffaers, N. Pradhan, O. F. Mohammed, O. M. Bakr, P. Yang, P. Müller-Buschbaum, P. V. Kamat, Q. Bao, Q. Zhang, R. Krahne, R. E. Galian, S. D. Stranks, S. Bals, V. Biju, W. A. Tisdale, Y. Yan, R. L. Z. Hoye, L. Polavarapu, ACS Nano, 2021, 15 (7), 10775 – 10981

[6] J. P. Attfield, P. Lightfoot, R. E. Morris, Dalton Trans, 2015, 44, 10541 – 10542

[7] Q. A. Akkerman, L. Manna, ACS Energy Lett., 2020, 5, 604 – 610

[8] F.S. Galasso, Structure, properties and preparation of perovskite-type compounds, Pergamon Press, 1969

[9] R. J. D. Tilley, Perovskites: Structure-Property Relationships, John Wiley & Sons, 2016

[10] Y. Zhou, Y. Zhao, Energy Environ. Sci., 2019, 12, 1495 – 1511

[11] F. Haydous, J. M. Gardner, U. B. Cappel, J. Mater. Chem. A, 2021, 9, 23419 – 23443

[12] Y. Rong, Y. Hu, A. Mei, H. Tan, M. I. Saidaminov, S. I. Seok, M. D. McGehee, E. H. Sargent, H. Han, Rong et al., Science, 2018, 361 (1214), 1 – 7

[13] K. S. Schanze, P. V. Kamat, P. Yang, J. Bisquert, ACS Energy Lett., 2020, 5, 2602 – 2604

[14] K. Zhang, N. Zhu, M. Zhang, L. Wang, J. Xing, J. Mater. Chem. C, 2021, 9, 3795 – 3799

[15] R. H. Mitchell, M. D. Welch, A. R. Chakhmouradian, Mineralogical Magazine, 2017, 81 (3), 411 – 461

[16] R. M. Hazen, Scientific American, 1988, 258, 74 – 81

[17] M. V. Kovalenko, L. Protesescu, M. I. Bodnarchuk, Science, 2017, 358, 745 – 750

[18] M. W. Lufaso, P. M. Woodward, Acta Cryst., 2004, B60, 10 – 20

[19] J. Chen, Q. Zhao, N. Shirahata, J. Yin, O. M. Bakr, O. F. Mohammed, H. Sun, ACS Materials Lett., 2021, 3, 845 – 861

[20] B. Halperin, R. Englman, Physical review B, 1971, 3 (6), 1698 – 1708

[21] P. Atkins, T. Overton, J. Rourke, M. Weller, F. Armstrong, Chimica inorganica, 2nd edition, Zanichelli, 2012, 502 – 503

[22] N. F. Atta, A. Galal, E. H. El-Ads, Chapter 4: Perovskite Nanomaterials – Synthesis, Characterization, and Applications, in Perovskite Materials – Synthesis, Characterisation, Properties, and Applications, edited by L. Pan and G. Zhu, IntechOpen, 2016, 107 – 151

[23] Q. A. Akkerman, G. Rainò, M. V. Kovalenko, L. Manna, Nature Materials, 2018, 17, 394 – 405

[24] S. Lou, T. Xuan, J. Wang, Optical Materials: X, 2019, 1 (100023), 1 – 17

[25] J. Almutlaq, J. Yin, O. F. Mohammed, O. M. Bakr, J. Phys. Chem. Lett., 2018, 9, 4131 – 4138

[26] S. A. Kulkarni, S. G. Mhaisalkar, N. Mathews, P. P. Boix, Small Methods, 2019, 3 (1800231), 1 – 16

[27] M. C. Brennan, M. Kuno, S. Rouvimov, Inorg. Chem., 2019, 58, 1555 – 1560

[28] J. Ma, J. Yin, Y. Chen, Q. Zhao, Y. Zhou, H. Li, Y. Kuroiwa, C. Moriyoshi, Z. Li, O. M. Bakr, O. F. Mohammed, H. Sun, ACS Materials Lett., 2019, 1, 185 – 191

[29] M. Imran, V. Caligiuri, M. Wang, L. Goldoni, M. Prato, R. Krahne, L. De Trizio, L. Manna, J. Am. Chem. Soc., 2018, 140, 2656 – 2664

[30] X. Tang, M. van den Berg, E. Gu, A. Horneber, G. J. Matt, A. Osvet, A. J. Meixner, D. Zhang, C. J. Brabec, Nano Lett., 2018, 18, 2172 – 2178

[31] J. Butkus, P. Vashishtha, K. Chen, J. K. Gallaher, S. K. K. Prasad, D. Z. Metin, G. Laufersky, N. Gaston, J. E. Halpert, J. M. Hodgkiss, Chem. Mater., 2017, 29, 3644 – 3652

[32] G. Ramalingam, P. Kathirgamanathan, G. Ravi, T. Elangovan, B. Arjun kumar, N. Manivannan, K. Kasinathan, Quantum Dots - Fundamental and Applications, F. Divsar, IntechOpen, 2020, 11 – 12

[33] D. P. Nenon, K. Pressler, J. Kang, B. A. Koscher, J. H. Olshansky, W. T. Osowiecki, M. A. Koc, L. Wang, A. P. Alivisatos, J. Am. Chem. Soc., 2018, 140, 17760 – 17772

[34] J. Ye, M. M. Byranvand, C. Otero Martìnez, R. L. Z. Hoye, M. Saliba, L. Polavarapu, Angew. Chem., 2021, 133, 21804 – 21828

[35] H. Jin, E. Debroye, M. Keshavarz, I. G. Scheblykin, M. B. J. Roeffaers, J. Hofkens J. A. Steele, Mater. Horiz., 2020, 7, 397 – 410

[36] A. De, S. Das, N. Mondal, A. Samanta, ACS Materials Lett., 2019, 1, 116 − 122

[37] J. De Roo, M. Ibáñez,P. Geiregat,G. Nedelcu, W. Walravens, J. Maes, J.C. Martins, I. Van Driessche, M.V. Kovalenko, Z. Hens, ACS Nano, 2016, 10, 2071 – 2081

[38] Y. Wang, D. Yu, Z. Wang, X. Li, X. Chen, V. Nalla, H. Zeng, H. Sun, Small, 2017, 13 (1701587), 1 – 8

[39] H. Lu, Y. Tang, L. Rao, Z. Li, X. Ding, C. Song, B. Yu, Nanotechnology, 2019, 30 (295603), 1 – 10

[40] Y. Wei, Z. Cheng, J. Lin, Chem. Soc. Rev., 2019, 48, 310 – 350

[41] S. Bera, R. K. Behera, S. D. Adhikari, A. K. Guria, Narayan Pradhan, J. Phys. Chem. Lett., 2021, 12, 11824 – 11833

[42] M. Liu, J. Zhao, Z. Luo, Z. Sun, N. Pan, H. Ding, X. Wang, Chem. Mater., 2018, 30, 5846 – 5852

[43] J. Chen, D. Liu, M. J. Al-Marri, L. Nuuttila, H. Lehtivuori, K. Zheng, Sci. China Mater., 2016, 59 (9), 719 – 727

[44] J. Im, C. Lee, J. Lee, S. Park, N. Park, Nanoscale, 2011, 3, 4088 – 4093

[45] L. C. Schmidt, A. Pertegás, S. González-Carrero, O. Malinkiewicz, S. Agouram, G. Mínguez Espallargas, H. J. Bolink, R. E. Galian, J. Pérez-Prieto, J. Am. Chem. Soc., 2014, 136, 850 – 853

[46] L. Protesescu, S. Yakunin, M. I. Bodnarchuk, F. Krieg, R. Caputo, C. H. Hendon, R. X. Yang, A. Walsh, M. V. Kovalenko, Nano Lett., 2015, 15, 3692 – 3696

[47] J. A. Sichert, Y. Tong, N. Mutz, M. Vollmer, S. Fischer, K. Z. Milowska, R. García Cortadella, B. Nickel, C. Cardenas-Daw, J. K. Stolarczyk, A. S. Urban, J. Feldmann, Nano Lett., 2015, 15, 6521 – 6527

[48] F. Zhang, H. Zhong, C. Chen, X. Wu, X. Hu, H. Huang, J. Han, B. Zou, Y. Dong, ACS Nano, 2015, 9 (4), 4533 – 4542

[49] L. De Trizio, I. Infante, A. L. Abdelhady, S. Brovelli, L. Manna, Trends in Chemistry, 2021, 3 (8), 631 – 644

[50] M. Aamir, T. Adhikari, M. Sher, M. D. Khan, J. Akhtar, Jean-Michel Nunzi, Chem. Rec., 2018, 18, 230 – 238

[51] S. Sun, D. Yuan, Y. Xu, A. Wang, Z. Deng, ACS Nano, 2016, 10, 3648 – 3657

[52] H. Huang, F. Zhao, L. Liu, F. Zhang, X. Wu, L. Shi, B Zou, Q. Pei, H. Zhong, ACS Appl. Mater. Interfaces, 2015, 7, 28128 – 28133

[53] Q. A. Akkerman, V. D'Innocenzo, S. Accornero, A. Scarpellini, A. Petrozza, M. Prato, L. Manna, J. Am. Chem. Soc., 2015, 137, 10276 – 10281

[54] R. G. Pearson, J. Am. Chem. Soc., 1963, 85 (22), 3533 – 3539

[55] M. I. Saidaminov, J. Almutlaq, S. Sarmah, I. Dursun, A. A. Zhumekenov, R. Begum, J. Pan, N. Cho, O. F. Mohammed, O. M. Bakr, ACS Energy Lett., 2016, 1, 840 – 845

[56] X. Wang, J. Yu, M. Hu, Y. Wu, L. Yang, W. Ye, X. Yu, Journal of Luminescence, 2020, 221 (116986), 1 – 6

[57] A. Garza, R. Vega, E. Soto, Med Sci Monit, 2006, 12 (3), RA57 – 65

[58] G. Schileo, G. Grancini, J. Mater. Chem. C, 2021, 9, 67 – 76

[59] R. A. Sheldon, Current Opinion in Green and Sustainable Chemistry, 2019, 18, 13 – 19

[60] G. Lammel, H. Grassel, ESPR- Environ. Sci. & Pollut. Res., 1995, 2 (1), 40 – 45

[61] F. Zhou, Z. Hearne, C. Li, Current Opinion in Green and Sustainable Chemistry, 2019, 18, 118 – 123

[62] F. G. Calvo-Flores, M. J. Monteagudo-Arrebola, J. A. Dobado, J. Isac-García, Top Curr Chem (Z), 2018, 376 (18), 8 – 9

[63] D. Li, D. Zhang, K. Lim, Y. Hu, Y. Rong, A. Mei, N. Park, H. Han, Adv. Funct. Mater., 2021, 31 (2008621), 1 – 27

[64] D. B. Mitzi, Chem. Rev., 2019, 119, 3033 – 3035

[65] V. M. Fthenakis, H. C. Kim, Comprehensive Renewable Energy, 1, 2012, Pages 143-159

[66] T. J. Milstein, D. M. Kroupa, D. R. Gamelin, Nano Lett., 2018, 18, 3792 – 3799

[67] Inorganic Crystal Structure Database (ICDS): https://icsd.fiz-karlsruhe.de/index.xhtml *(last access:17/06/2022)*

[68] M. Kourgiantakis, M. Matzapetakis, C. P. Raptopoulou, A. Terzis, A. Salifoglou, Inorganica Chimica Acta, 2000, 297, 134 – 138

[69] M.S. Sonmez, R.V. Kumar, Hydrometallurgy, 2009, 95, 53 – 60

[70] C. de Weerd, J. Lin, L. Gomez, Y. Fujiwara, K. Suenaga, T. Gregorkiewicz, J. Phys. Chem. C, 2017, 121, 19490 – 19496

[71] M. Zampieri, S. R. Lazaro, C. A. Paskocimas, A. G. Ferreira, E. Longo, J. A. Varela, Journal of Sol-Gel Science and Technology, 2006, 37, 9 – 17

[72] R. Marques Ferreira, M. Motta, A. Batagin-Neto, C. F. de Oliveira Graeff, P. Noronha Lisboa-Filho, F. C. Lavarda, Materials Research, 2014, 17(3), 550 – 556

[73] Q. A. Akkerman, S. Genaro Motti, A. R. S. Kandada, E. Mosconi, V. D'Innocenzo, G. Bertoni, S. Marras, B. A. Kamino, L. Miranda, F. De Angelis, A. Petrozza, M. Prato, L. Manna, J. Am. Chem. Soc., 2016, 138, 1010 – 1016

[74] Z. Zhang, Y. Zhu, W. Wang, W. Zheng, R. Linac, Feng Huang, J. Mater. Chem. C, 2018, 6, 446 – 451

[75] Z. Zhang, Y. Zhu, W. Wang, W. Zheng, R. Lin, X. Li, H. Zhang, D. Zhong, F. Huang, Cryst. Growth Des., 2018, 18, 6393 – 6398

6. APPENDIX

6.1 X-ray diffraction

6.1.1 Reaction temperature

RTP13-1	RTP13-2
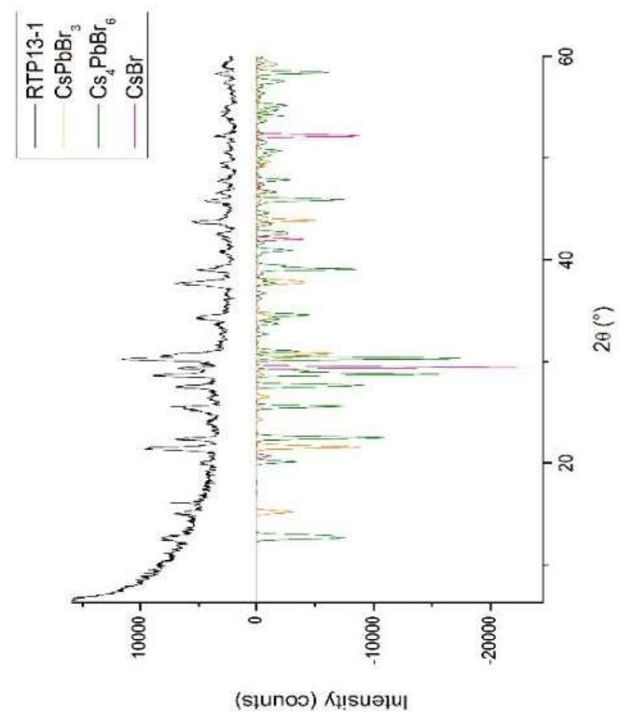	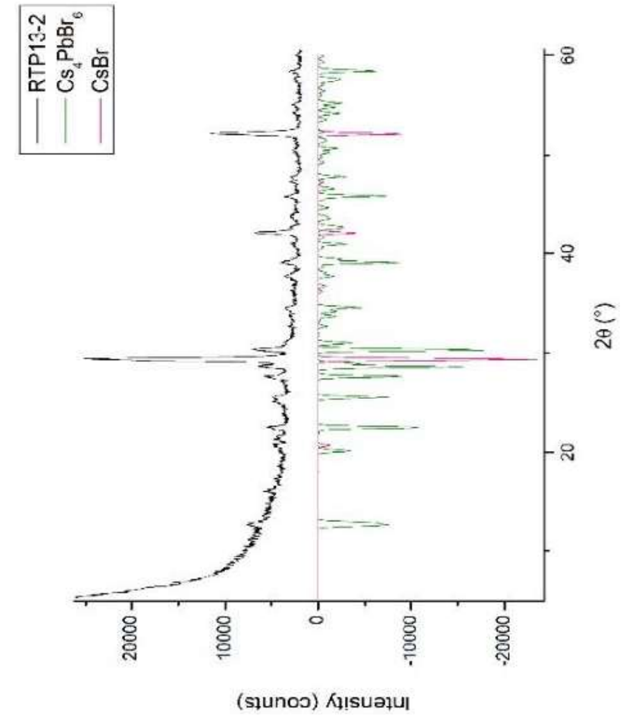
RTP14-1	RTP14-2
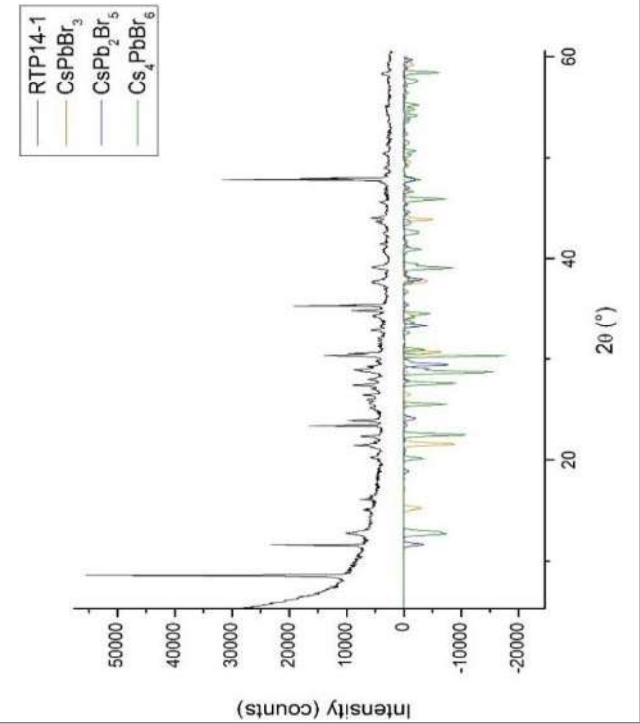	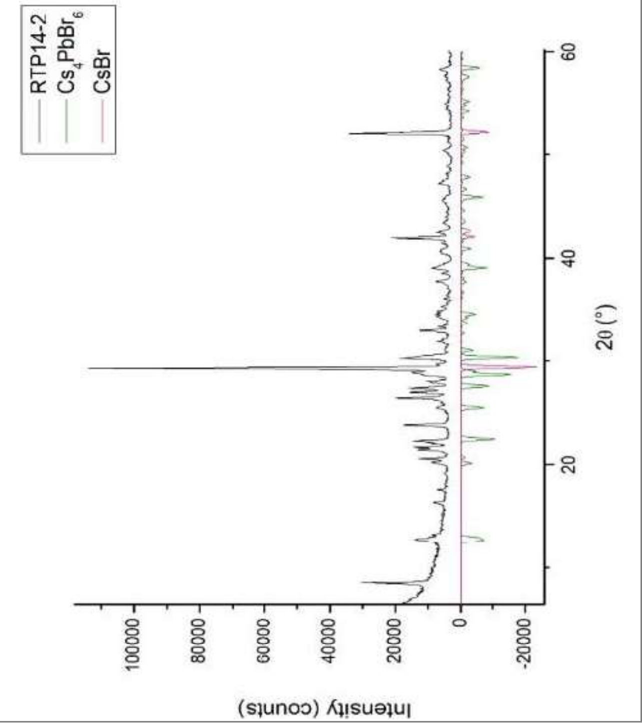

RTP15-1

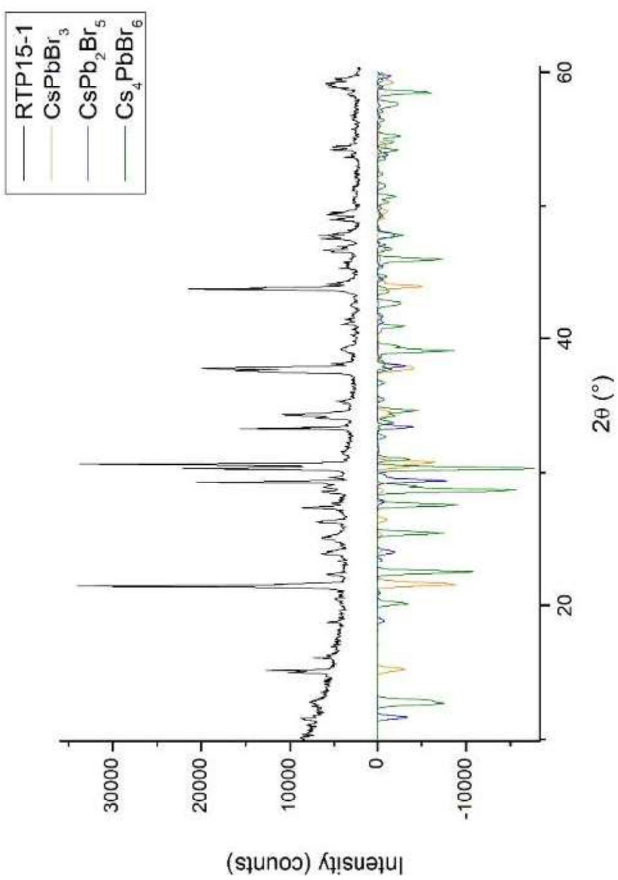

RTP15-2

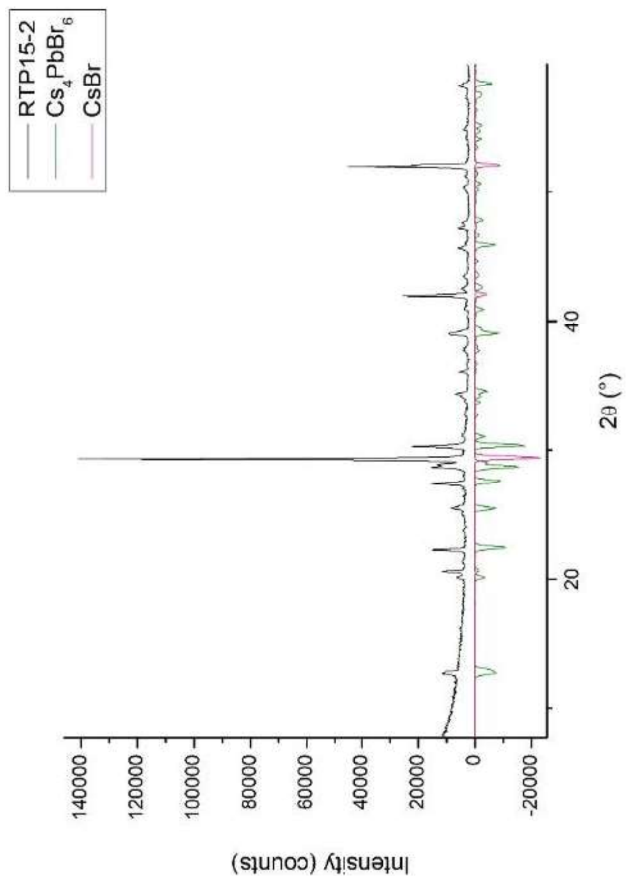

RTP16-1

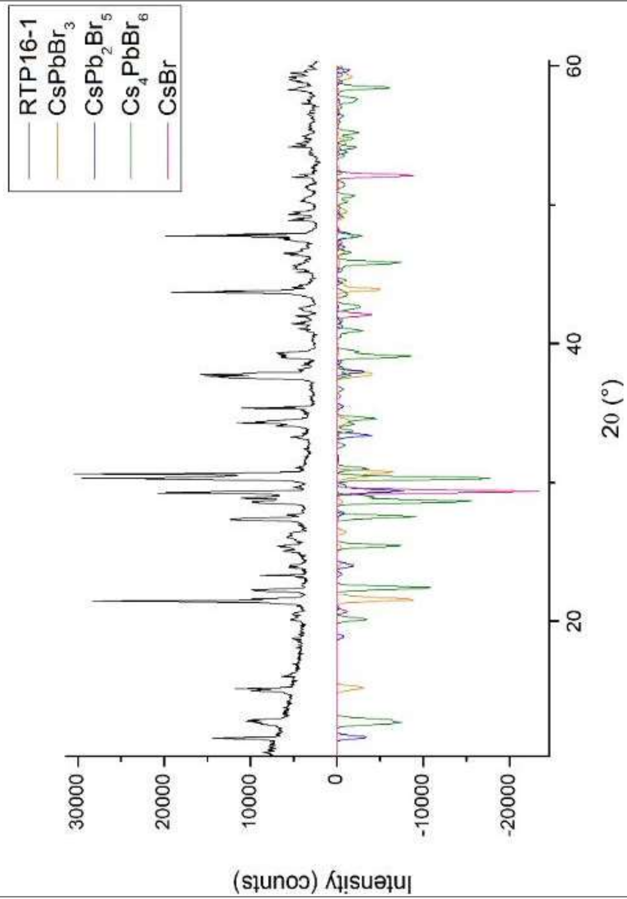

RTP16-2

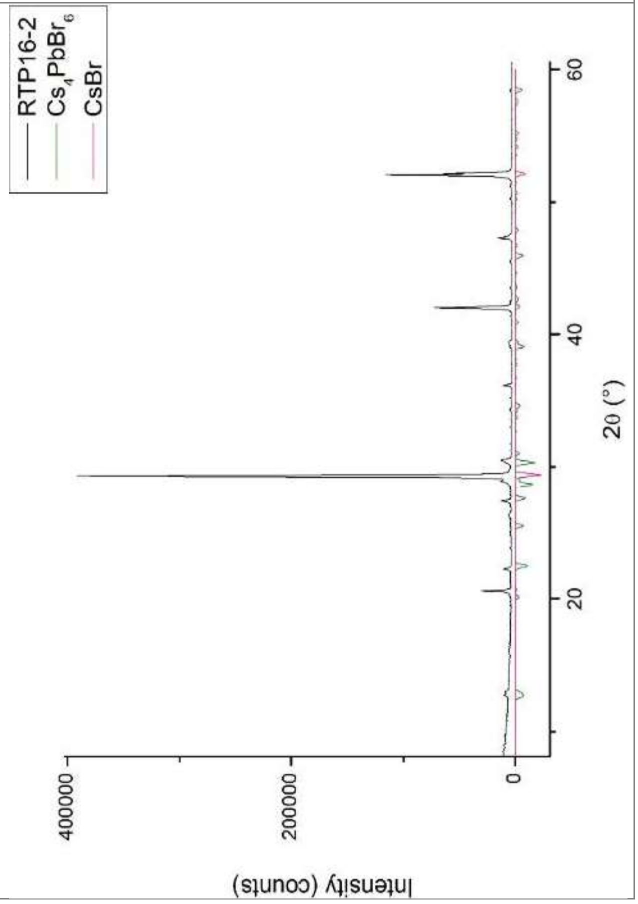

RTP17-1	RTP17-2
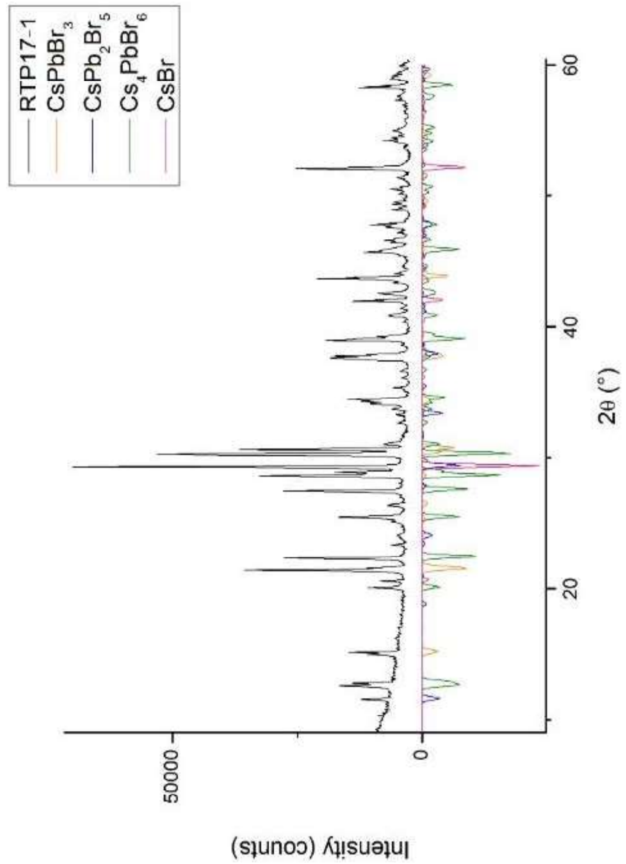	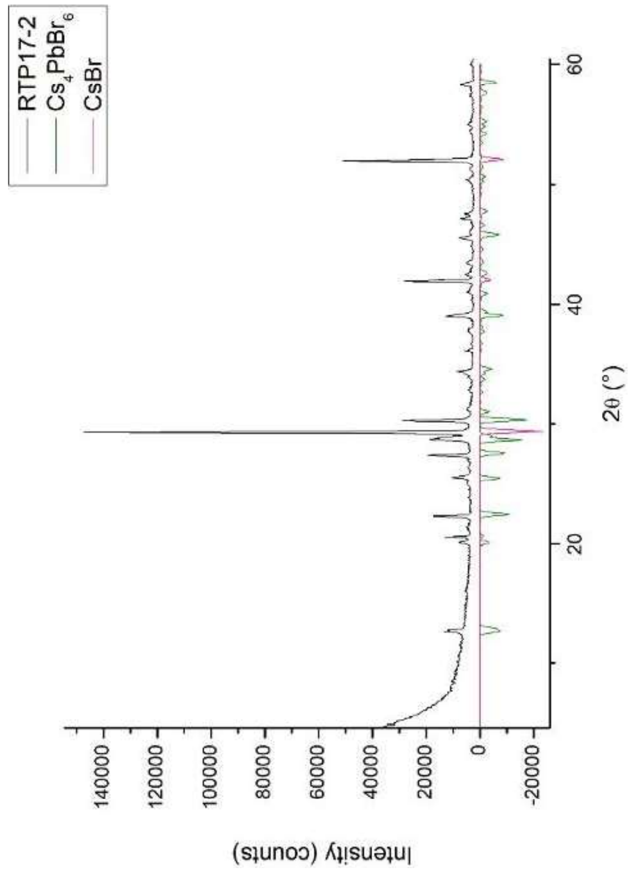
RTP18-1	**RTP18-2**
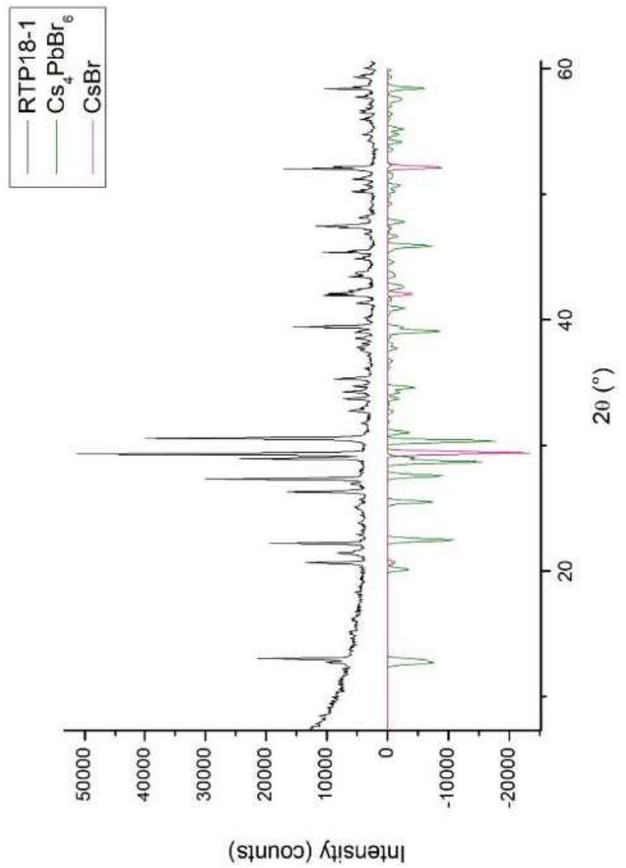	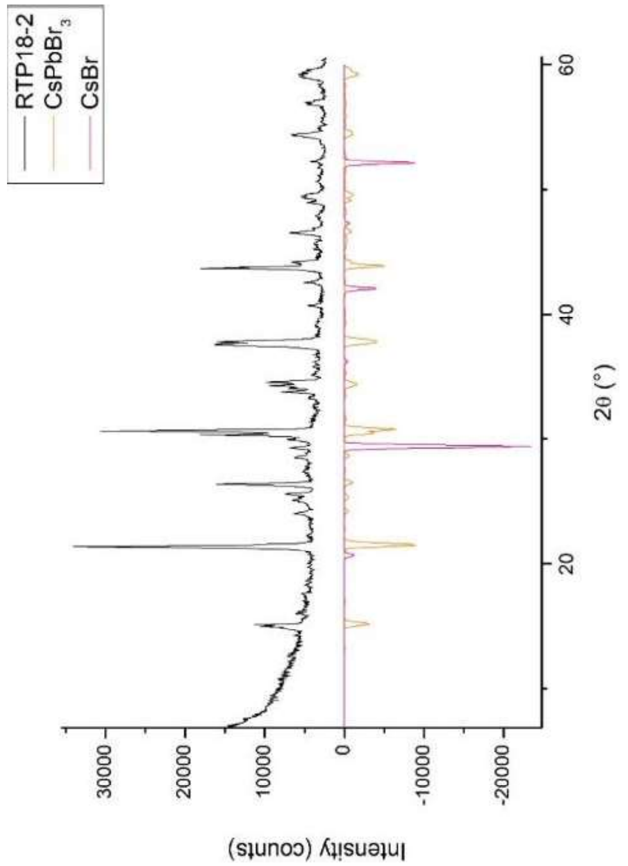

6.1.2 Reaction time

RTP27-1	RTP27-2
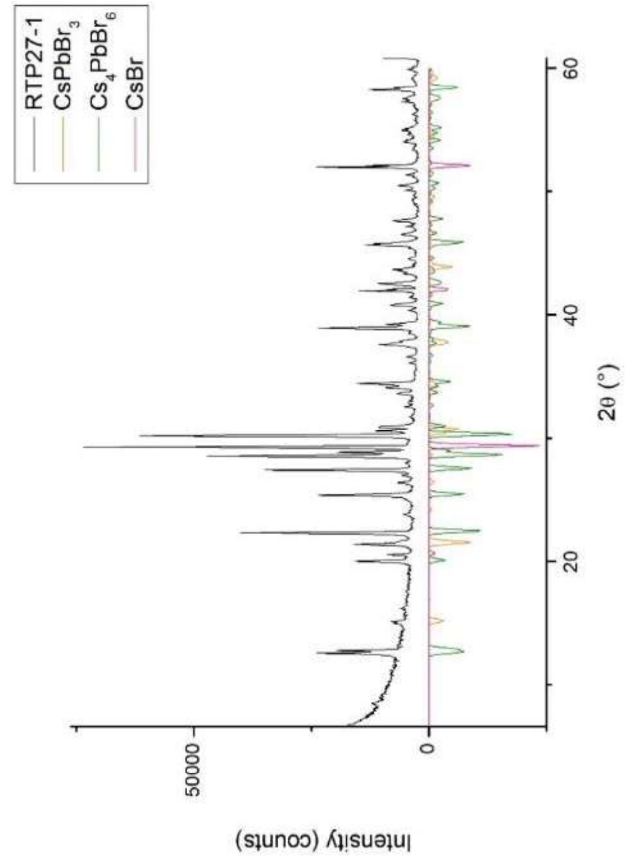	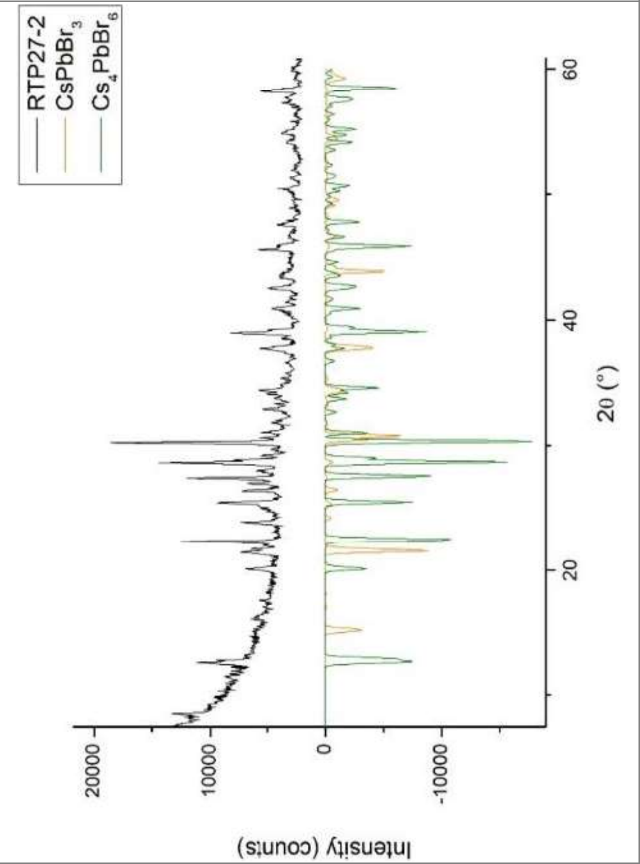
RTP28-1	RTP28-2
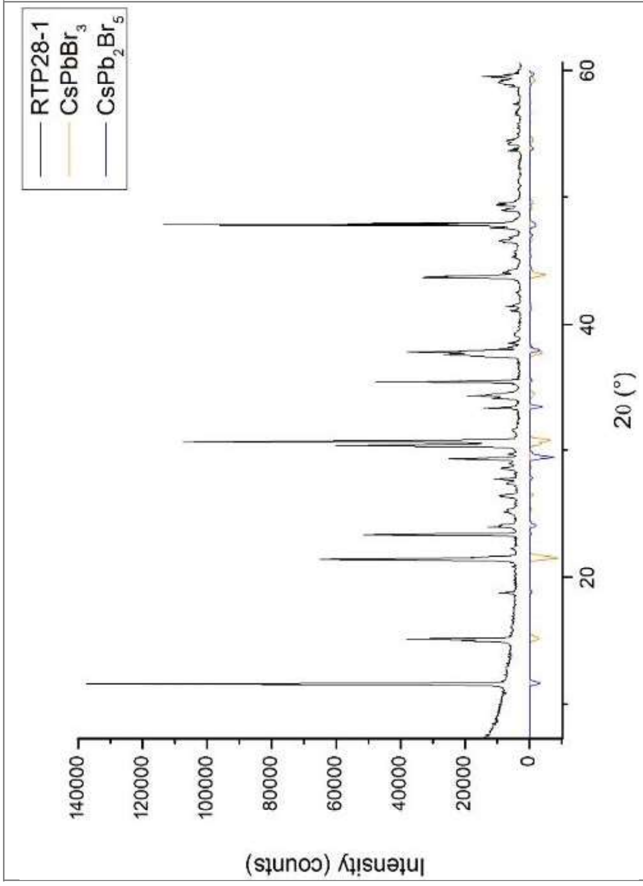	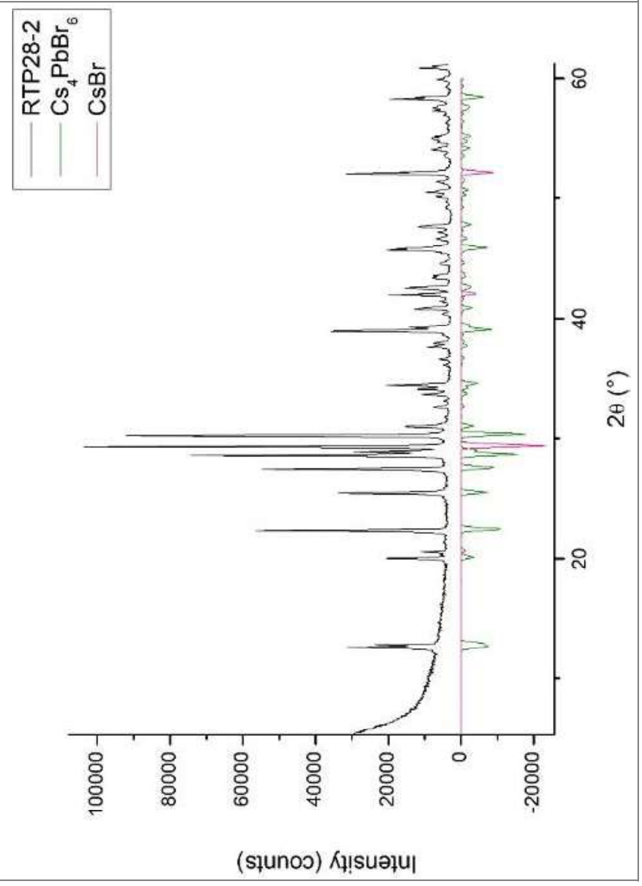

RTP29-1	RTP29-2
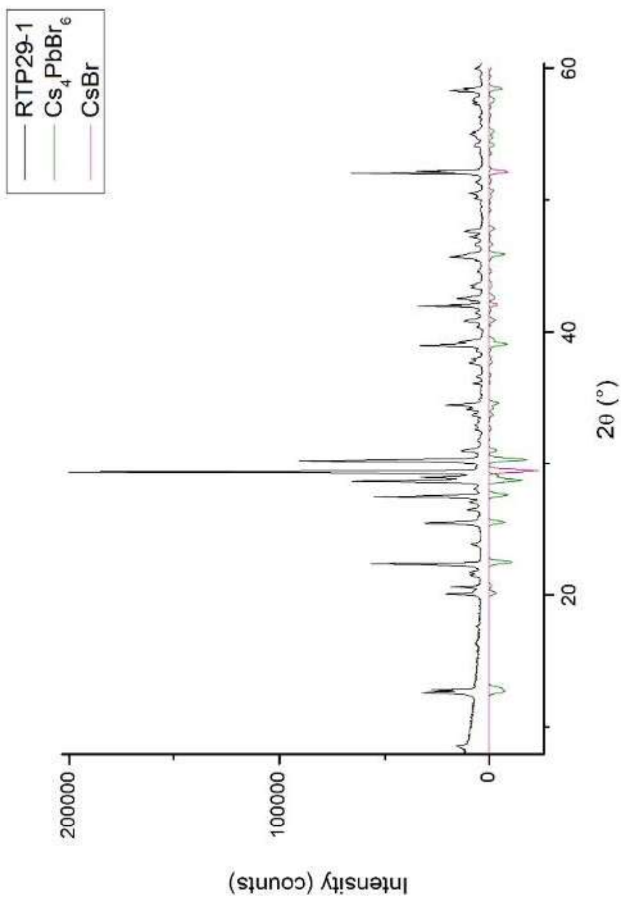	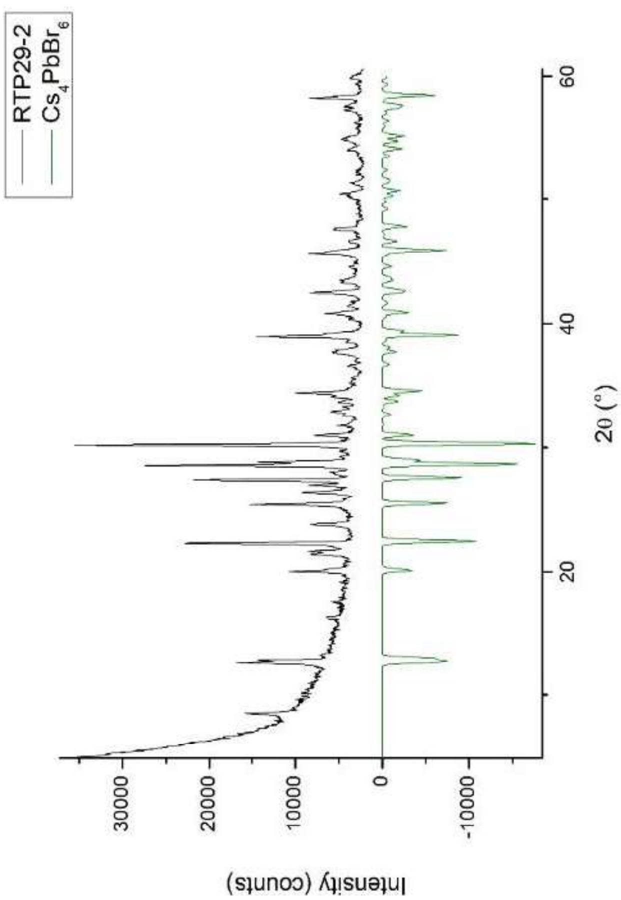
RTP21-1	RTP21-2
	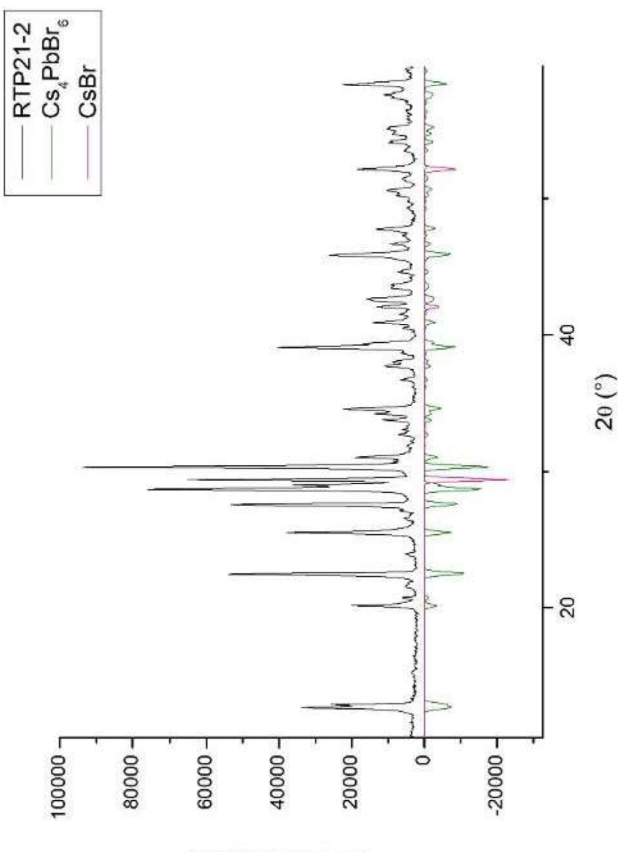

RTP22-1

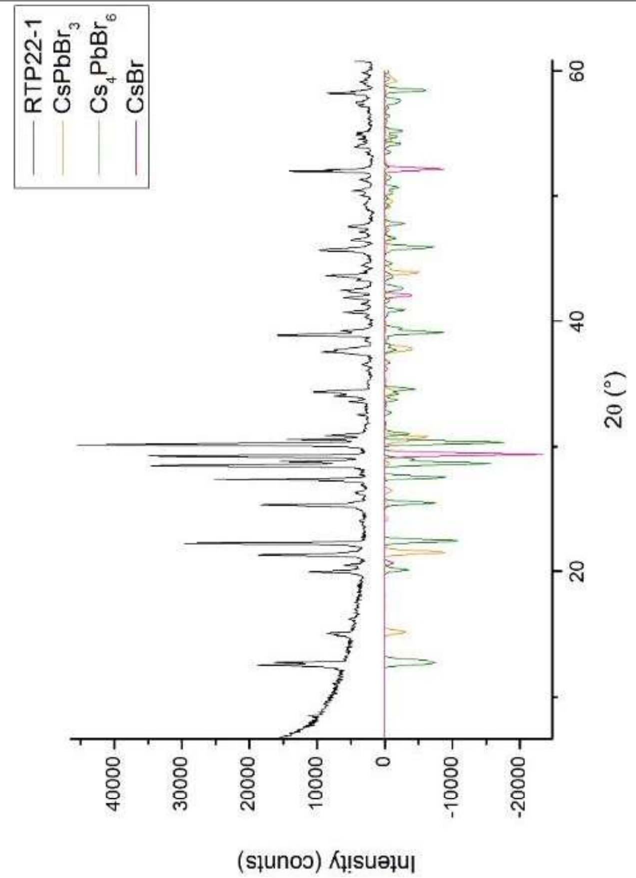

RTP22-2

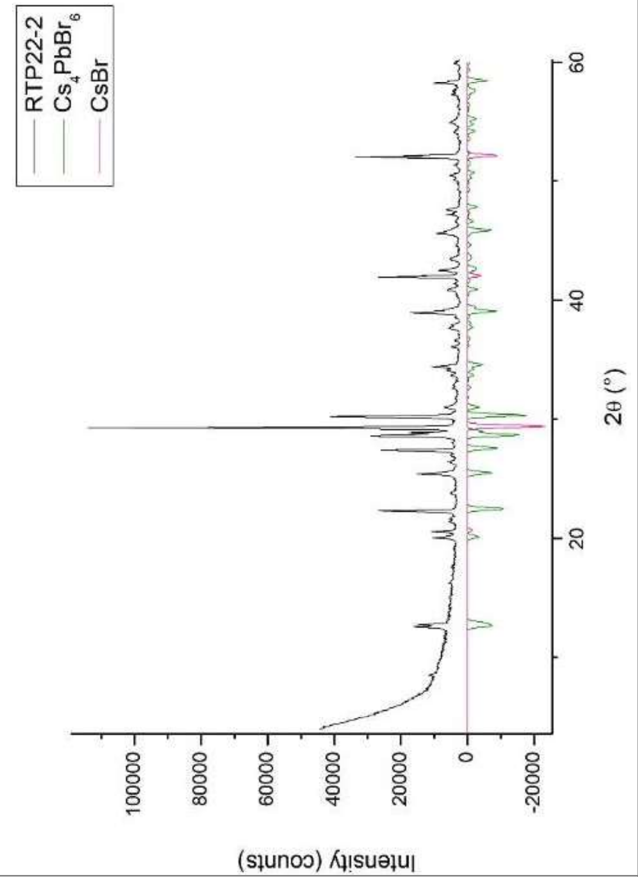

RTP23-1

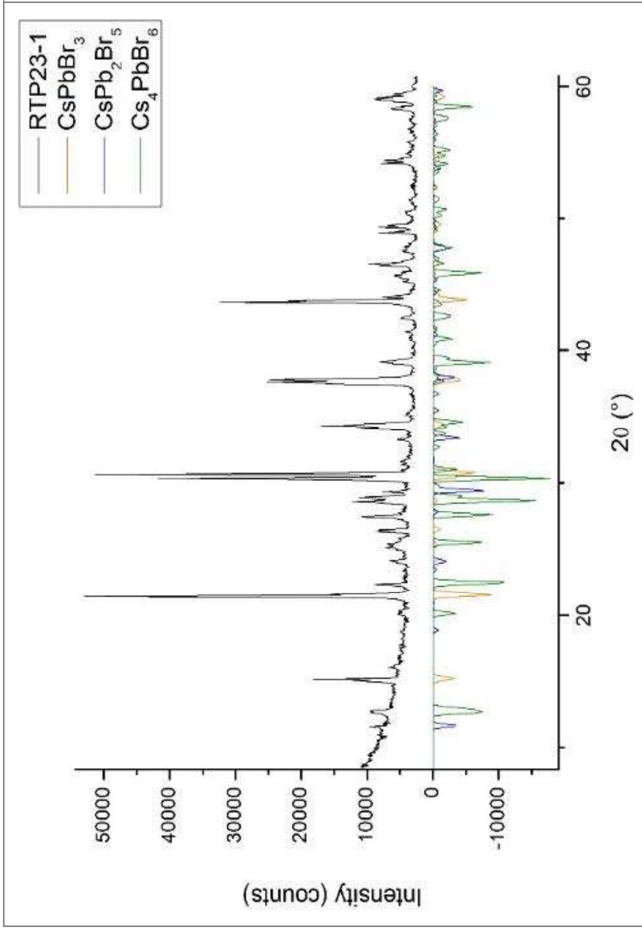

RTP23-2

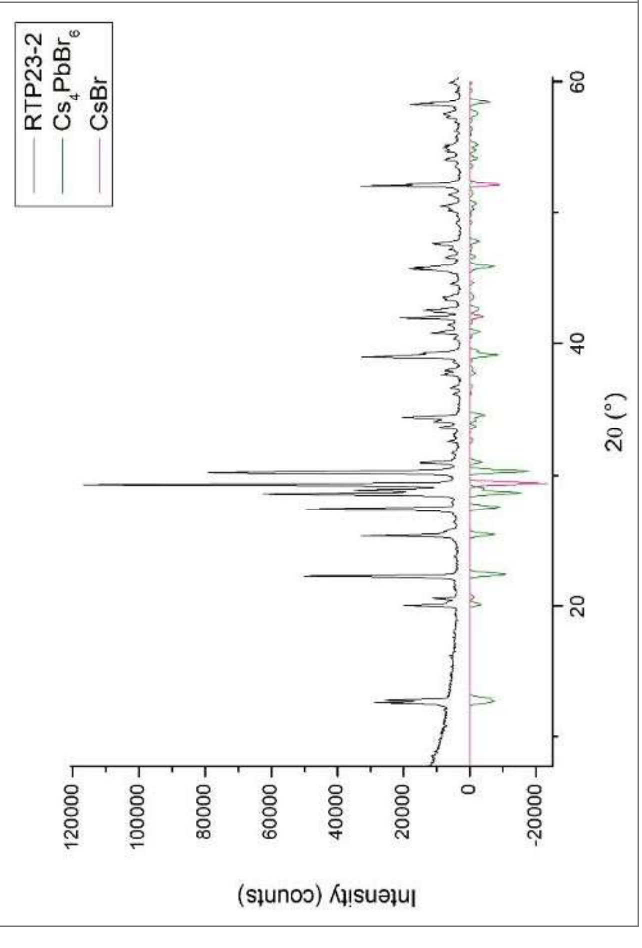

RTP24-11

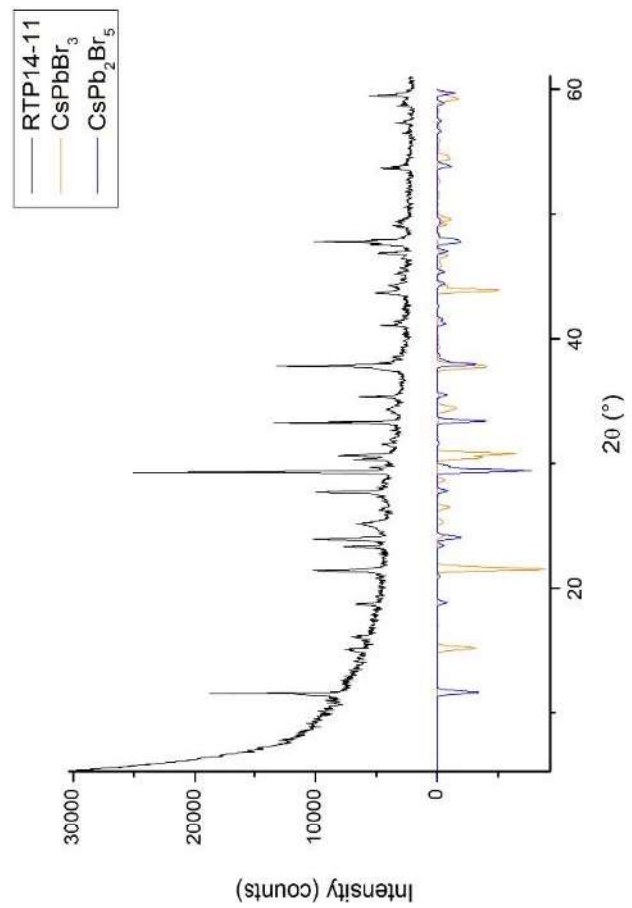

RTP24-12

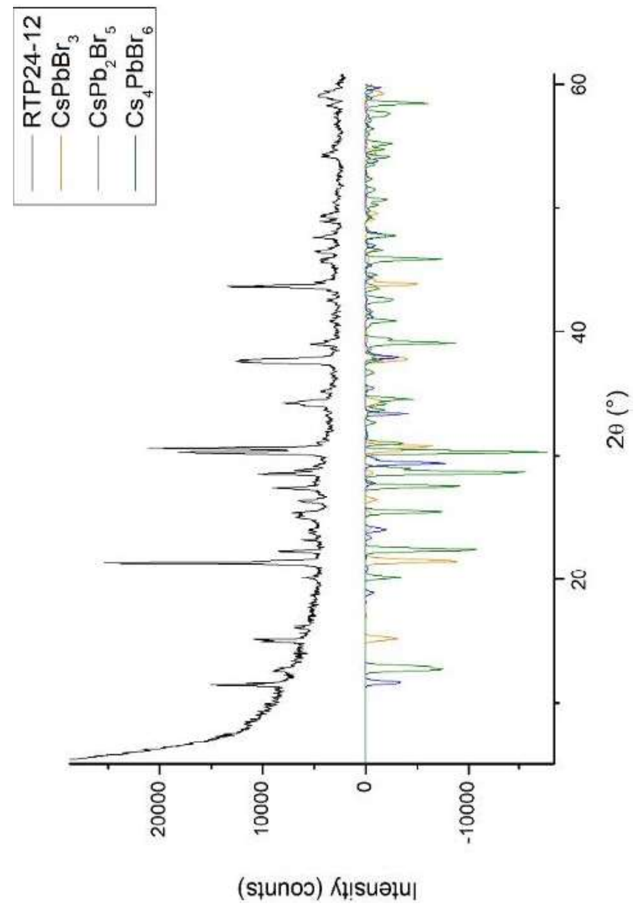

RTP25-1

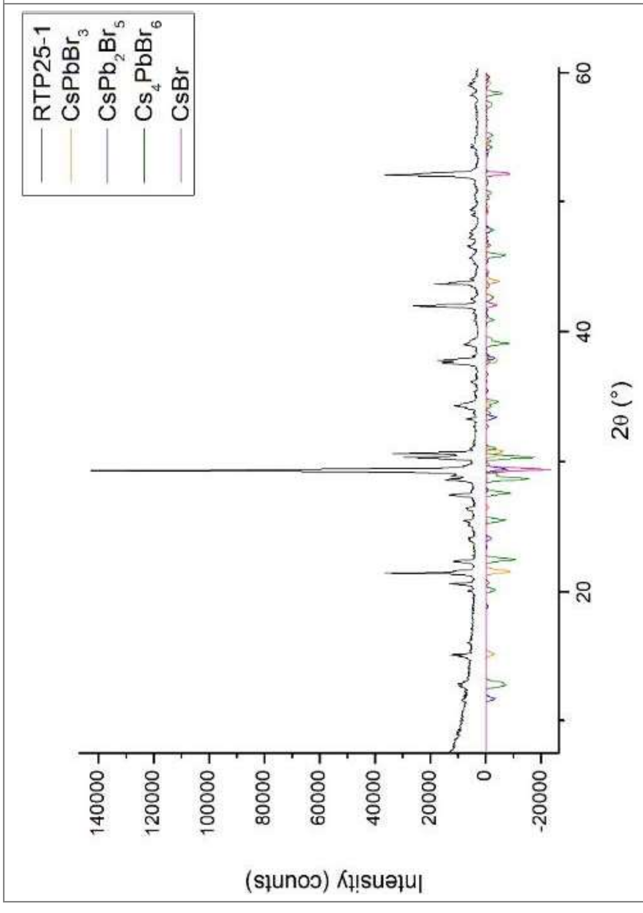

RTP25-2

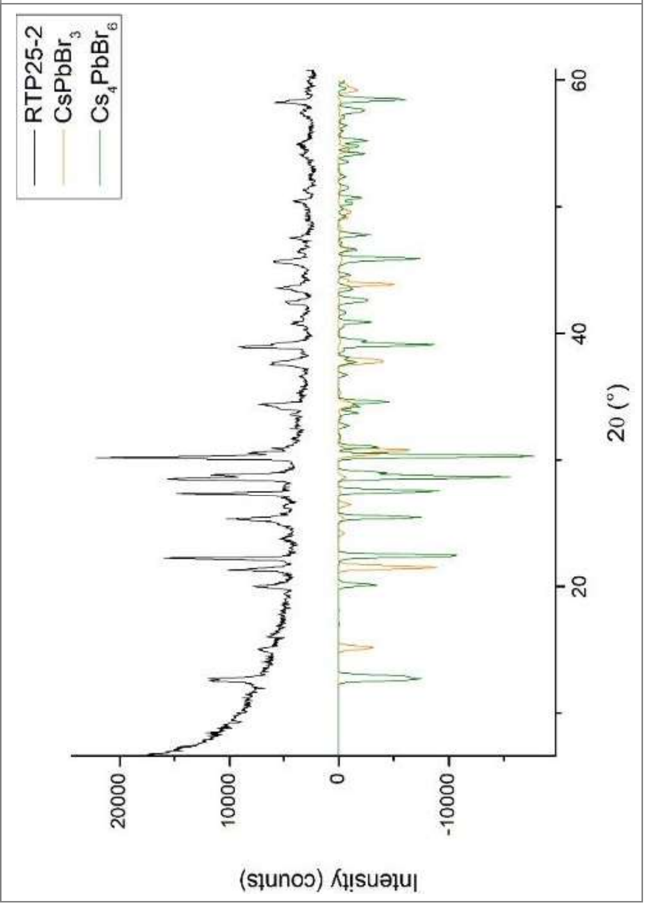

RTP26-1	
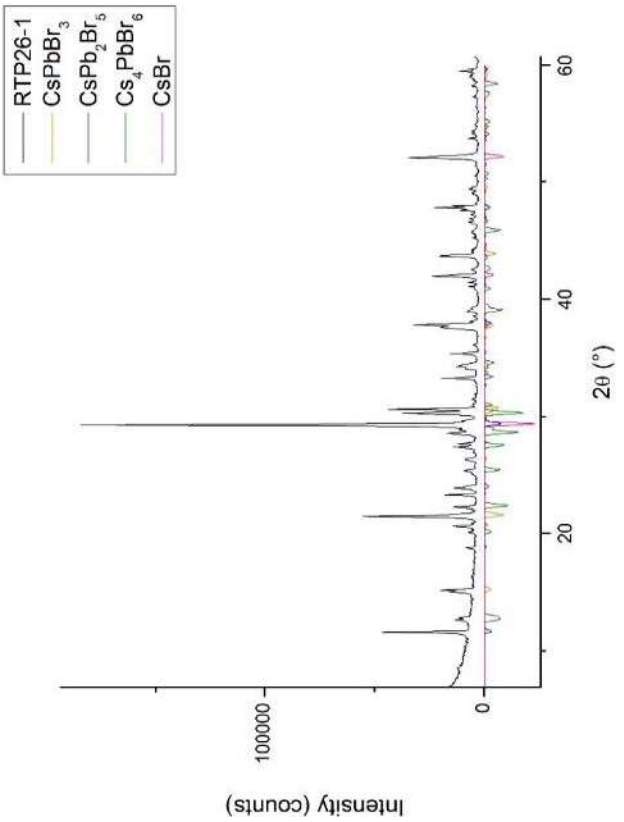	

6.1.3 Amount of citric acid

RTP37-1	RTP37-2
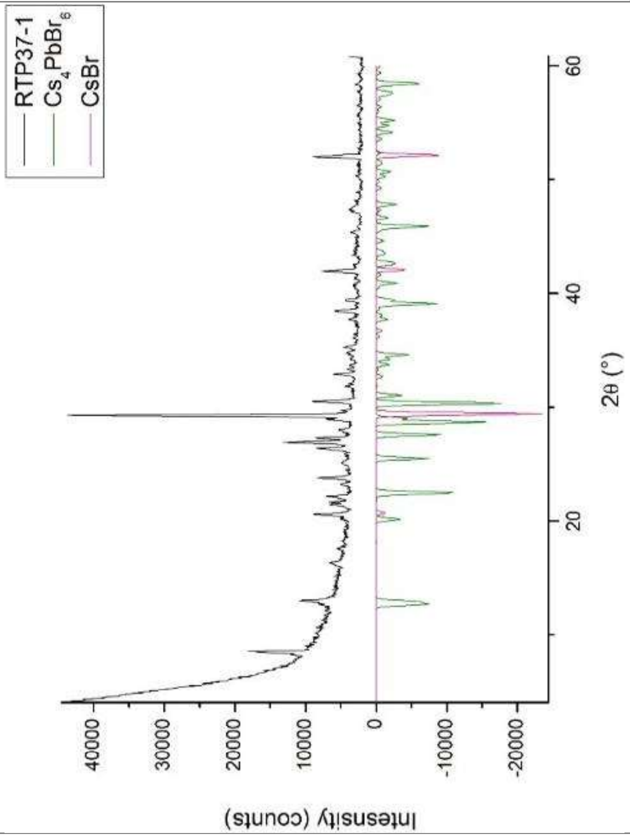	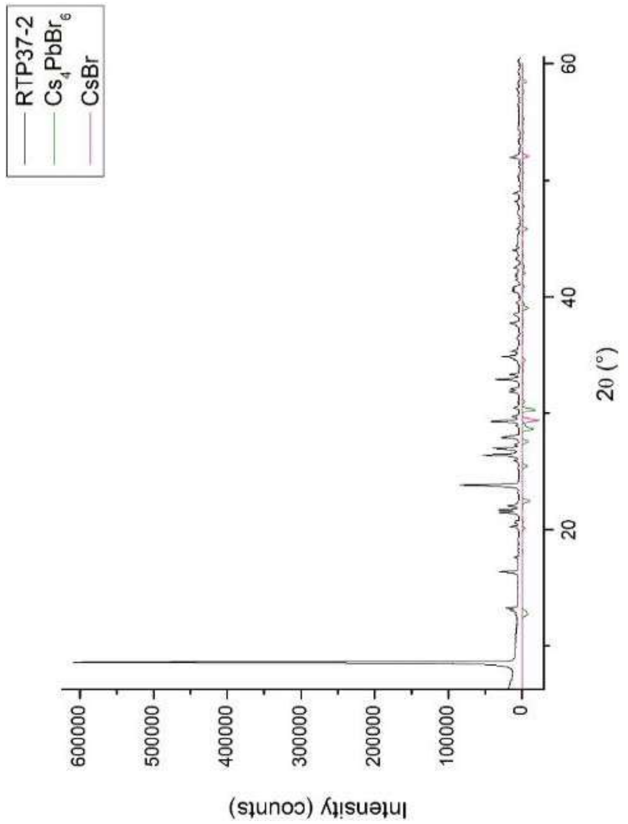

RTP38-1

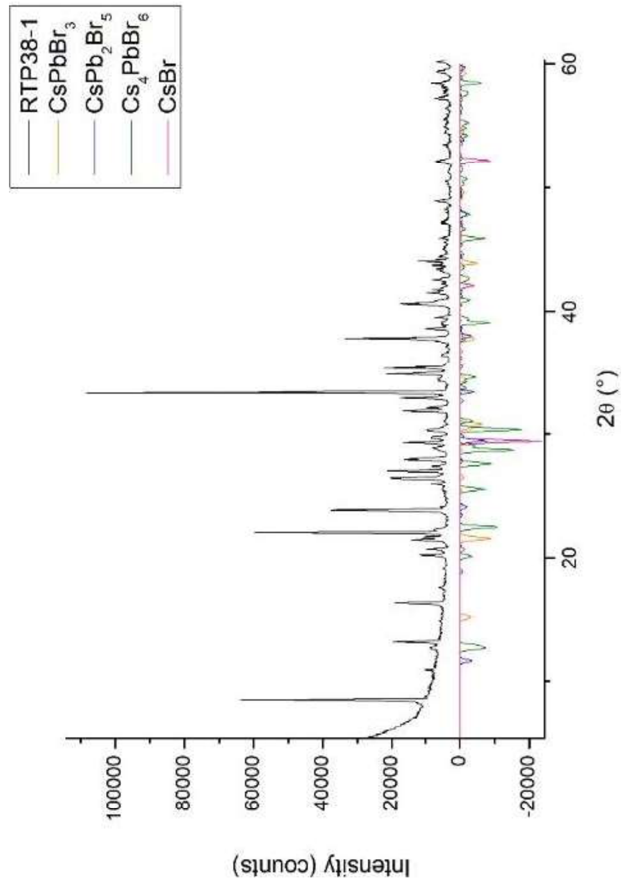

RTP38-2

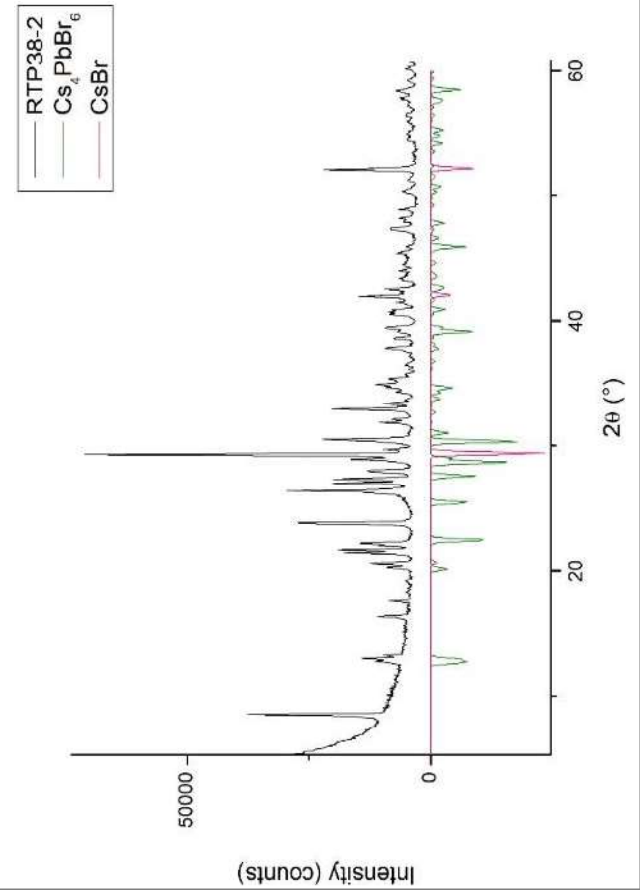

RTP43-1

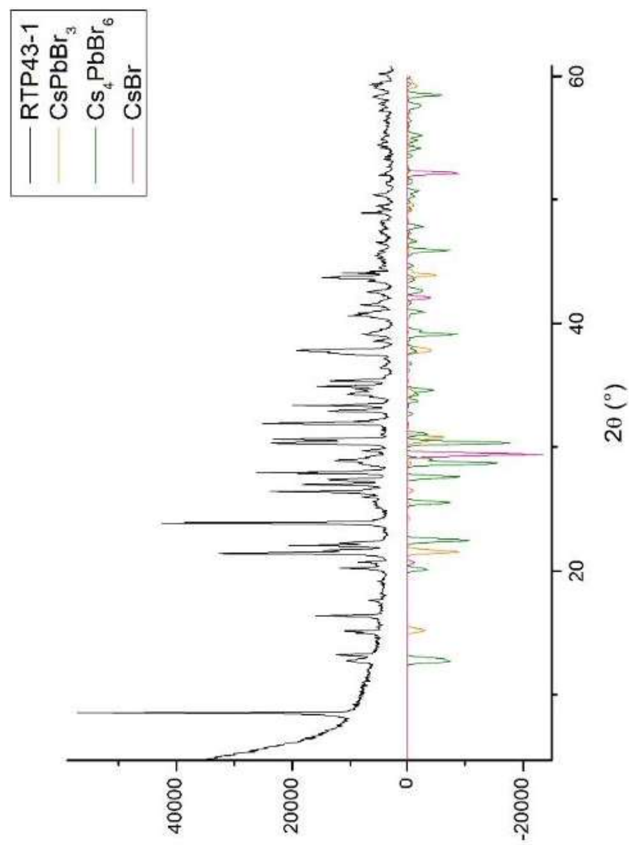

RTP43-2

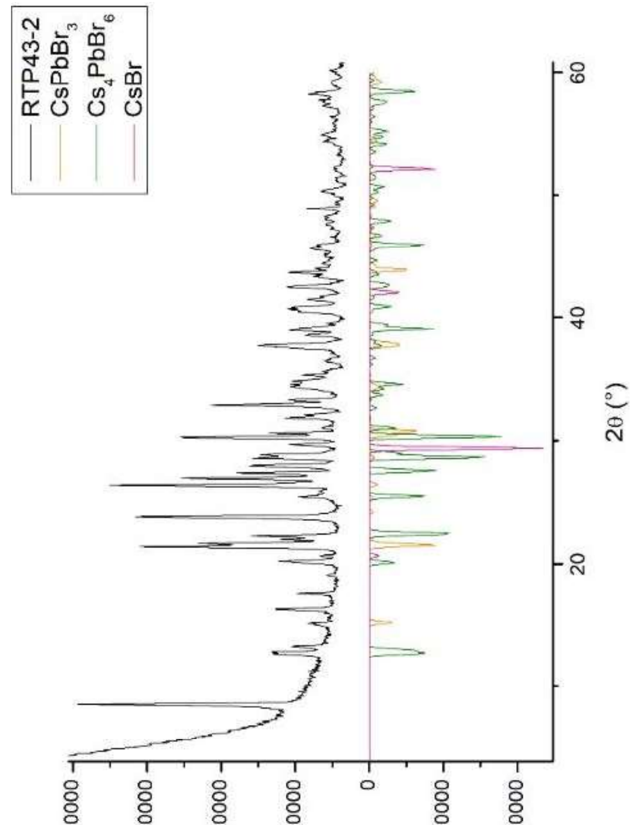

RTP44-1	RTP44-2
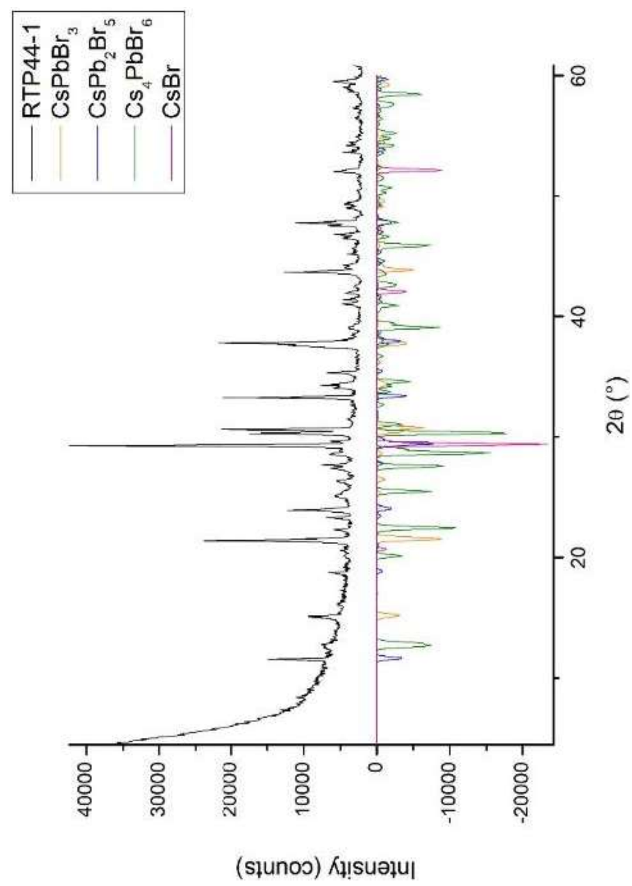	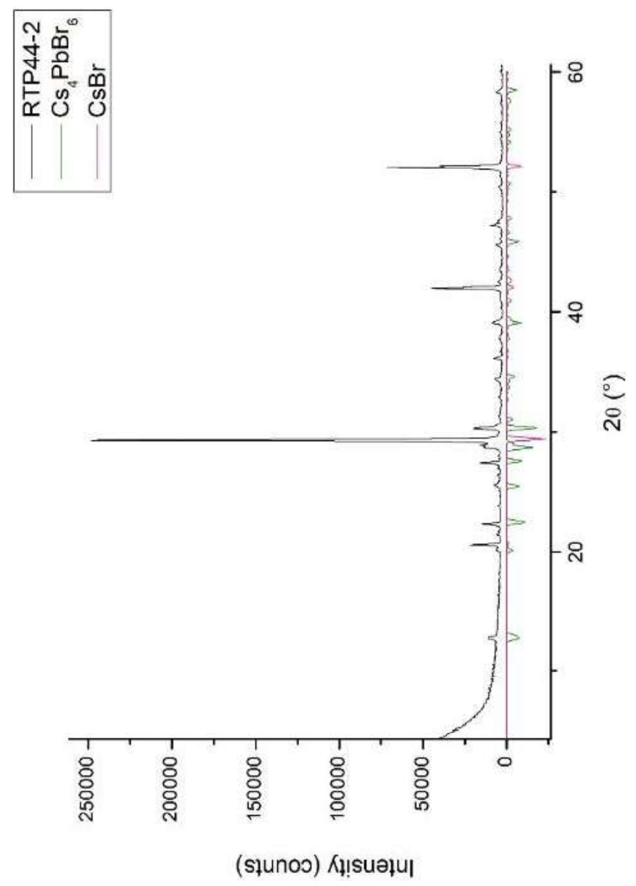
RTP45-1	**RTP45-2**
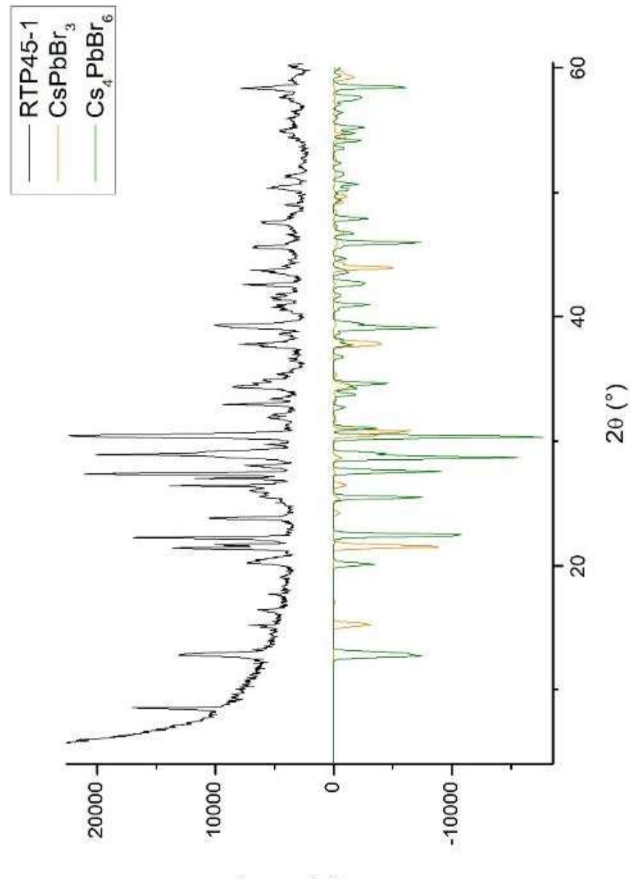	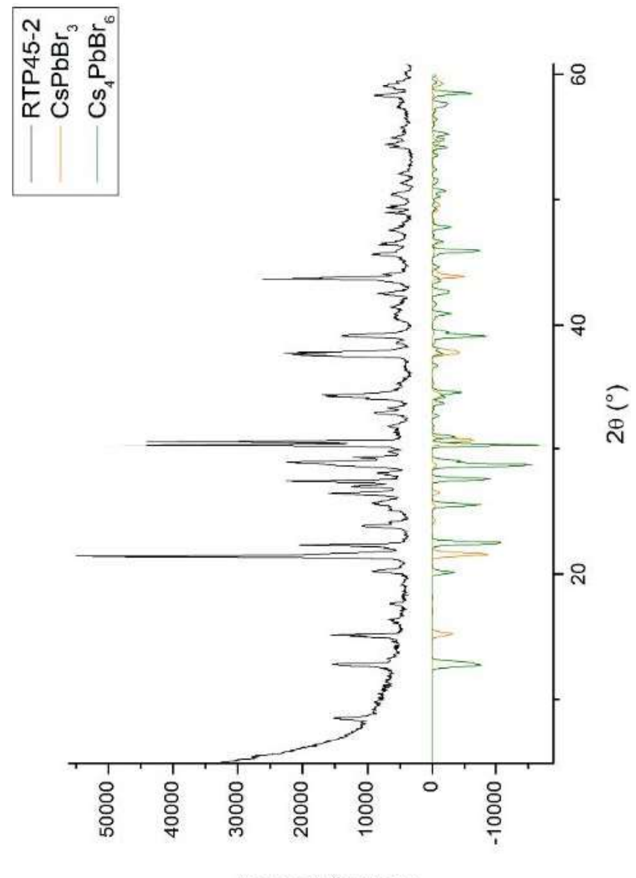

RTP42-1	RTP42-2
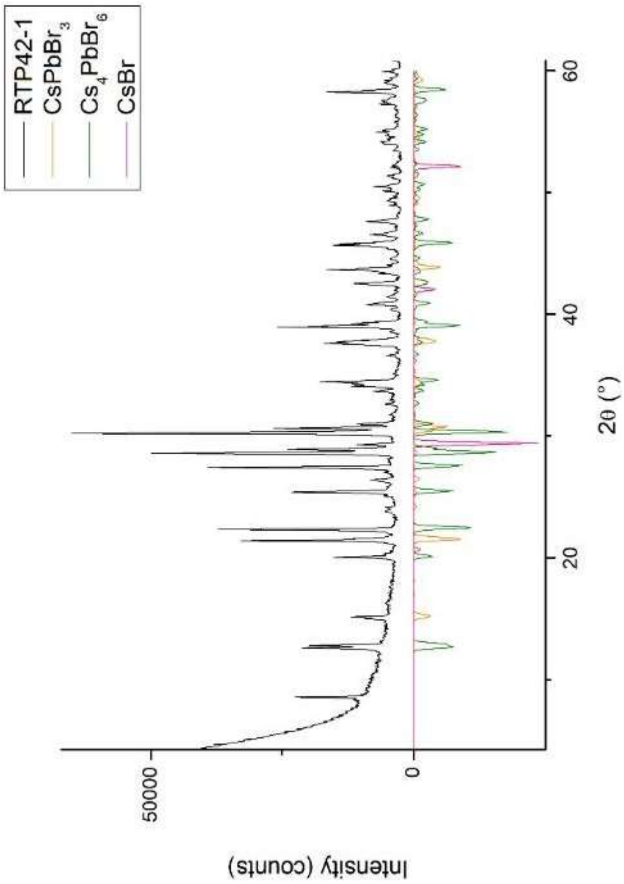	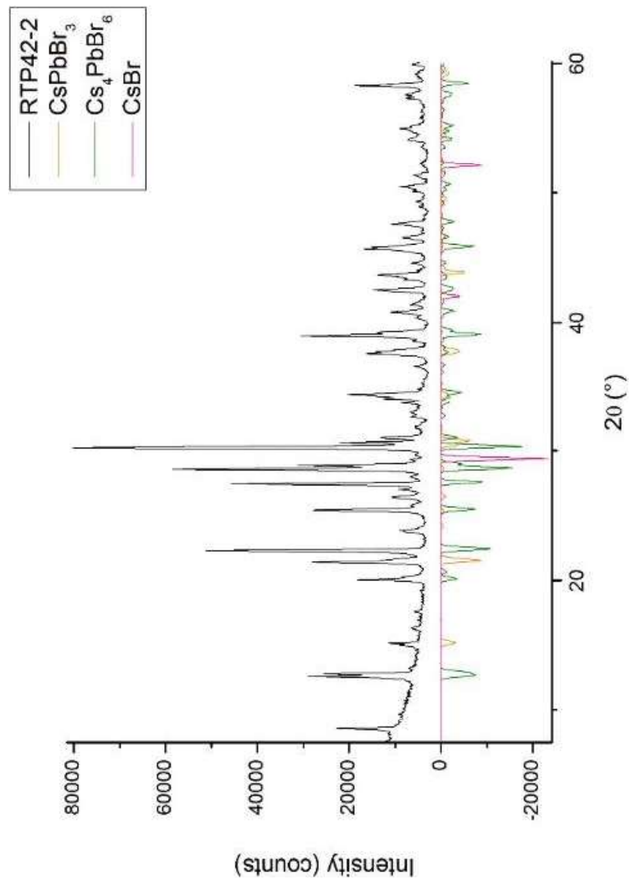
RTP41-1	RTP41-2
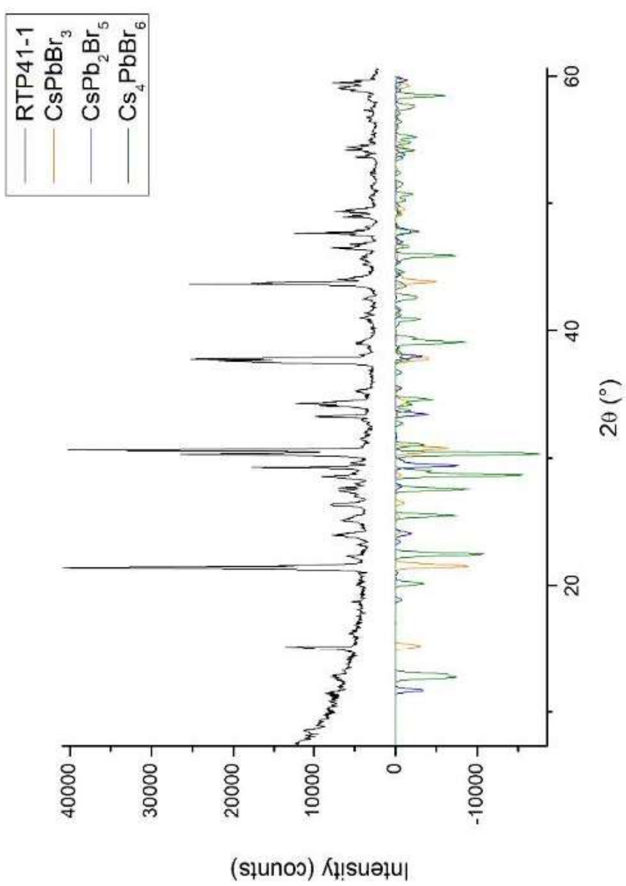	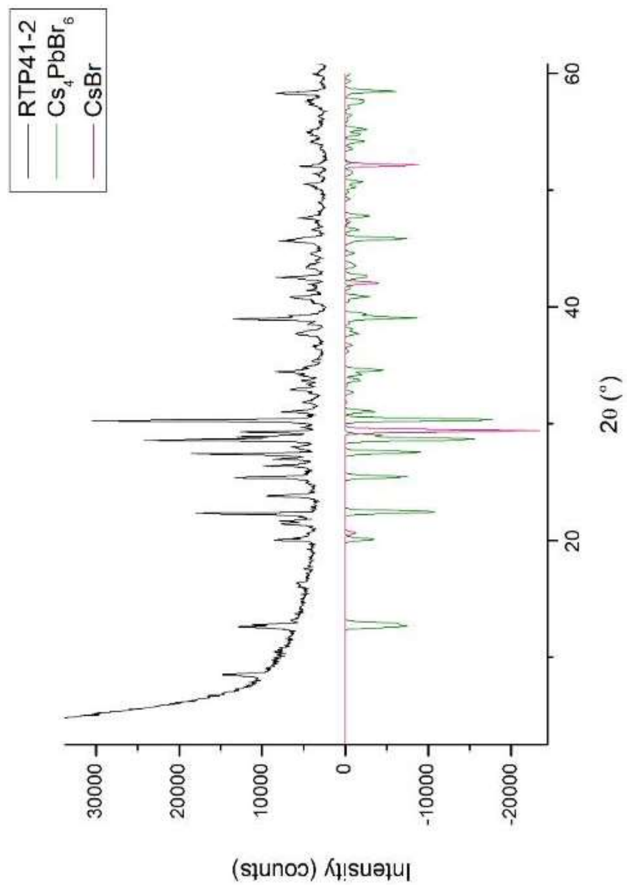

6.2 Scanning electron microscopy

<table>
<tr><td colspan="2">RTP13-2</td></tr>
<tr><td>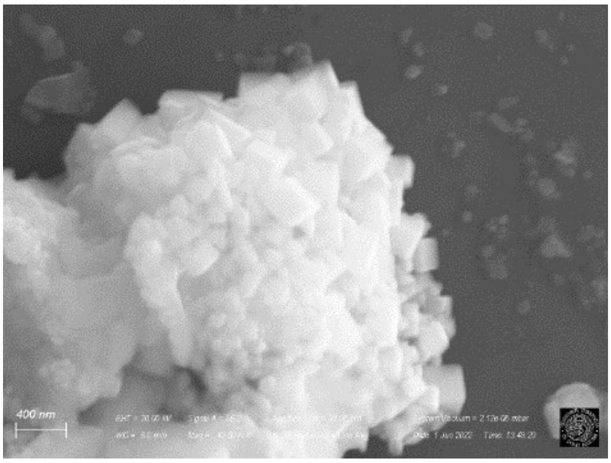 </td><td>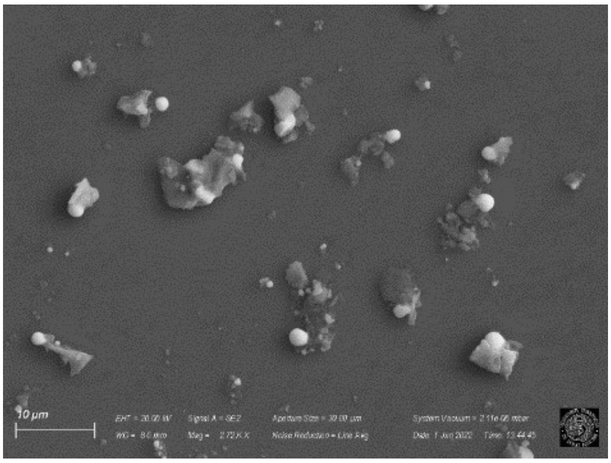 </td></tr>
<tr><td colspan="2">RTP14-2</td></tr>
<tr><td>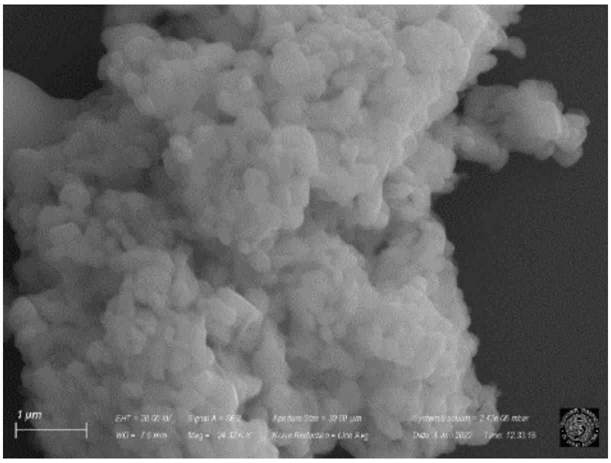 </td><td>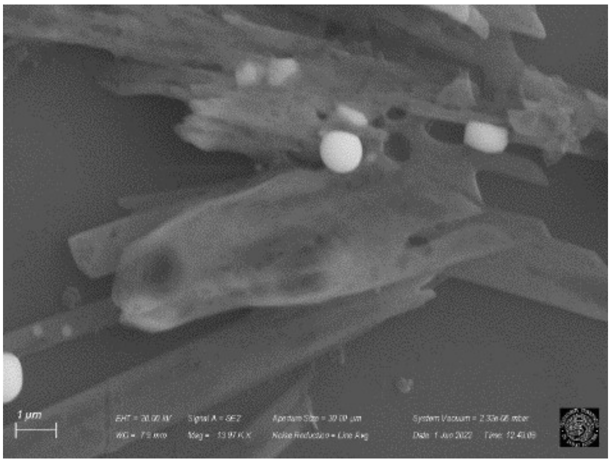 </td></tr>
<tr><td colspan="2">RTP18-1</td></tr>
<tr><td>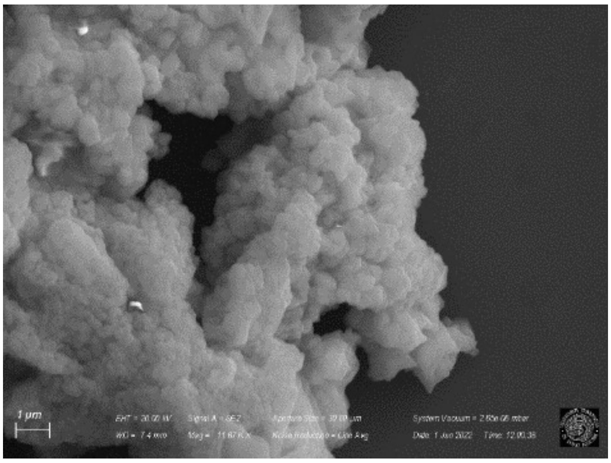 </td><td>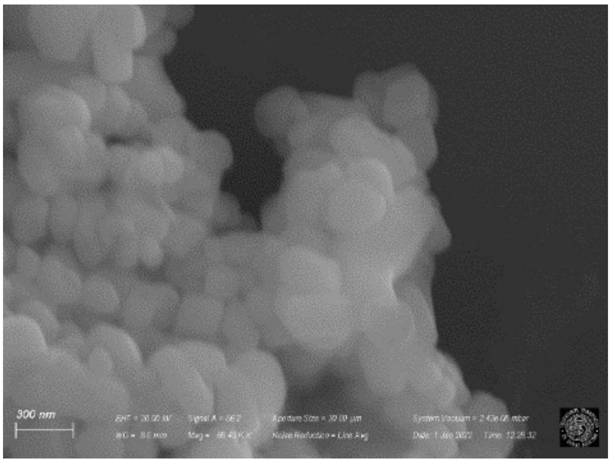 </td></tr>
</table>

RTP27-2

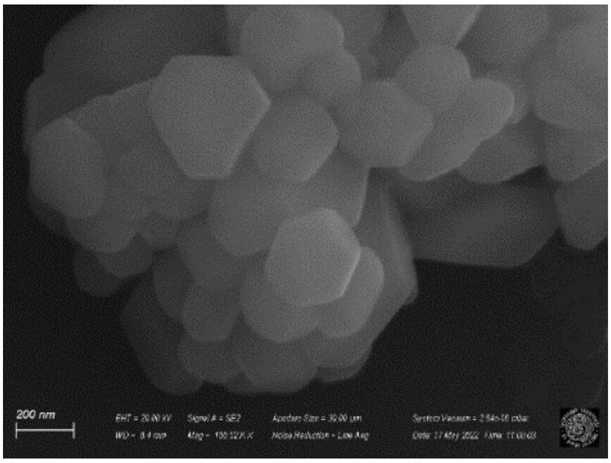

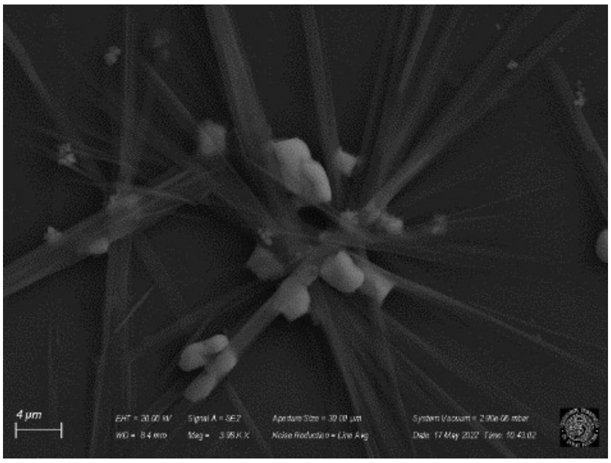

RTP21-2

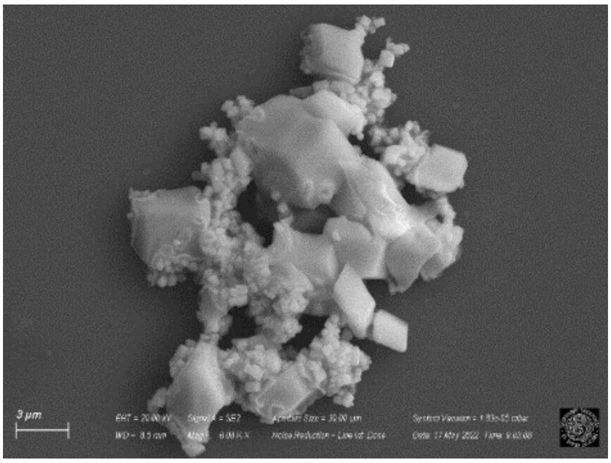

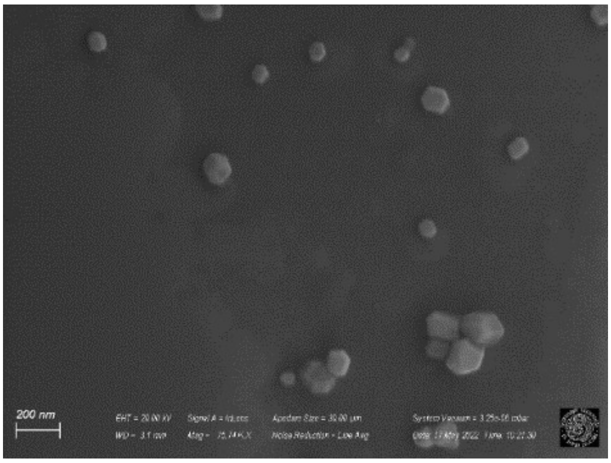

RTP24-12

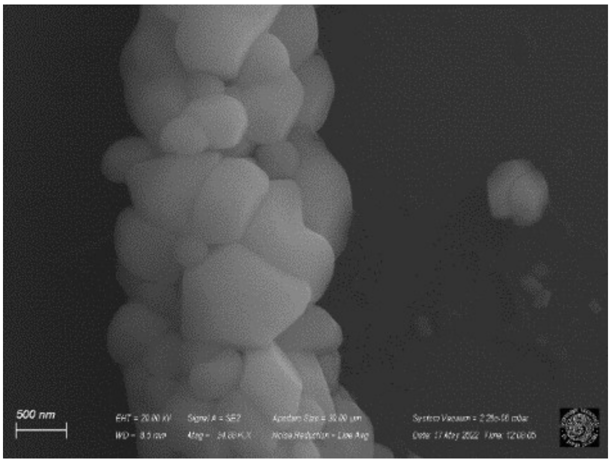

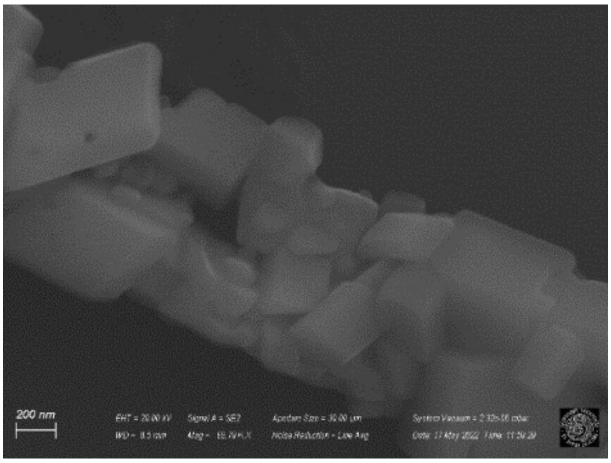

<table>
<tr><td colspan="2">RTP41-2</td></tr>
<tr><td>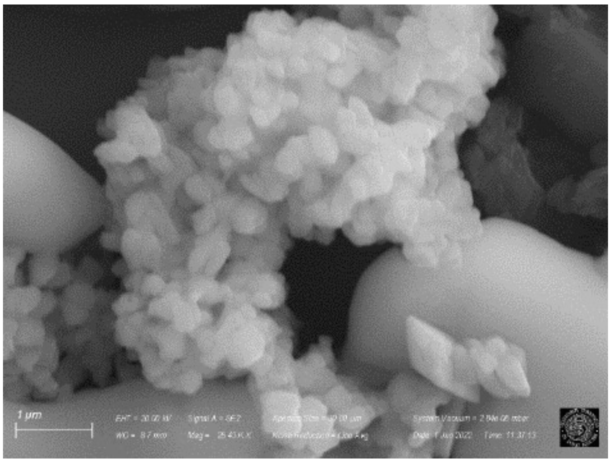
</td><td>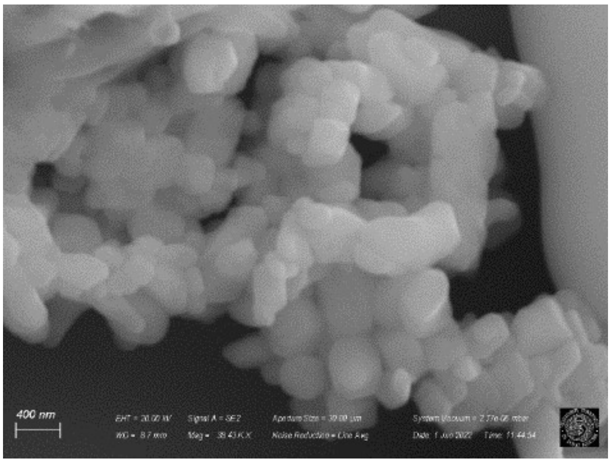
</td></tr>
<tr><td colspan="2">RTP44-2</td></tr>
<tr><td>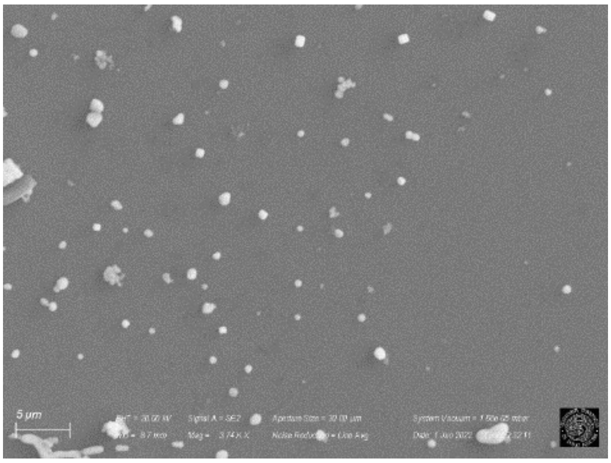
</td><td>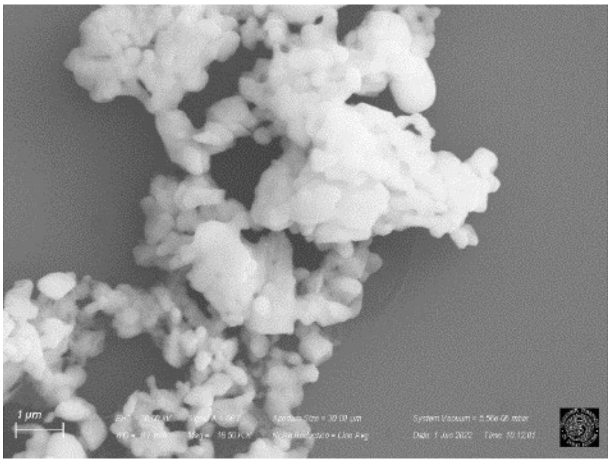
</td></tr>
</table>

6.3 Photoluminescence and photoluminescence excitation spectroscopy

RTP13-2	RTP15-2
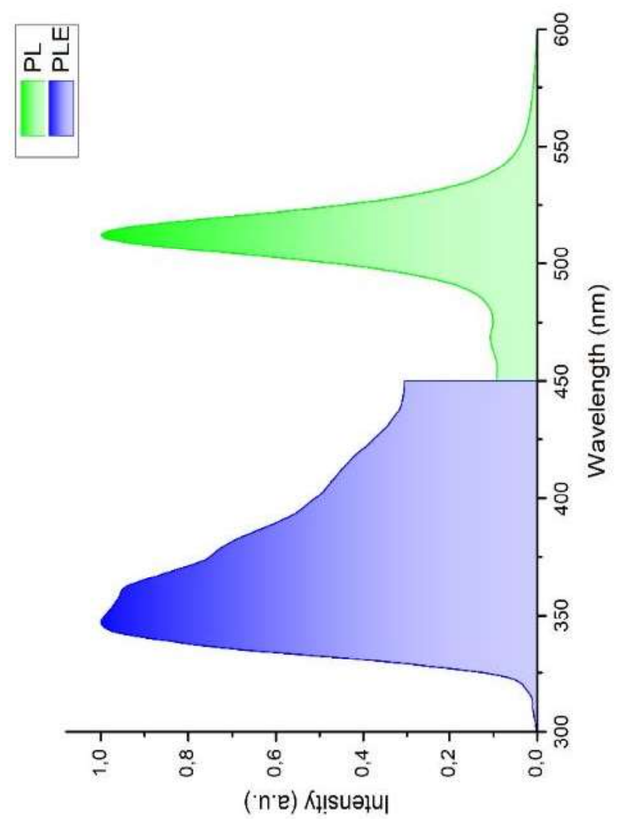	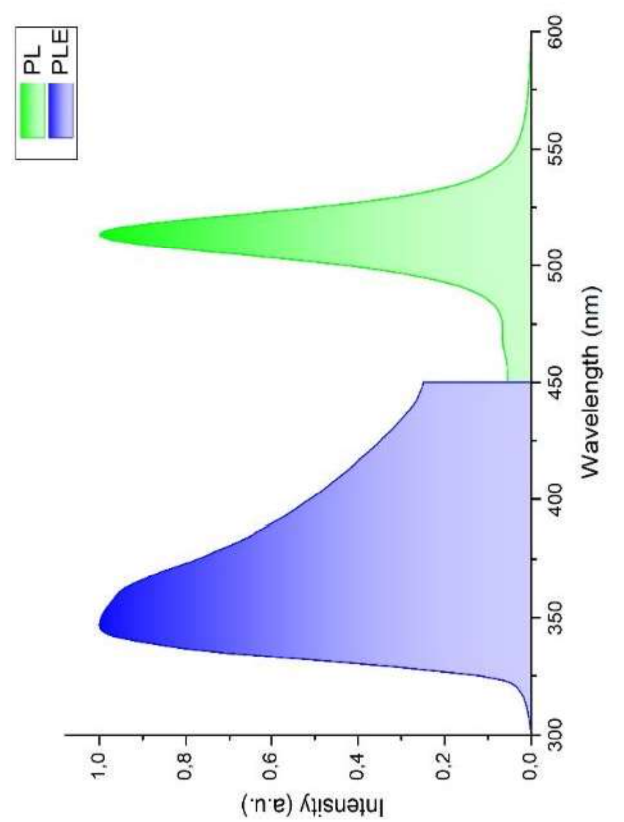
RTP17-2	RTP27-2
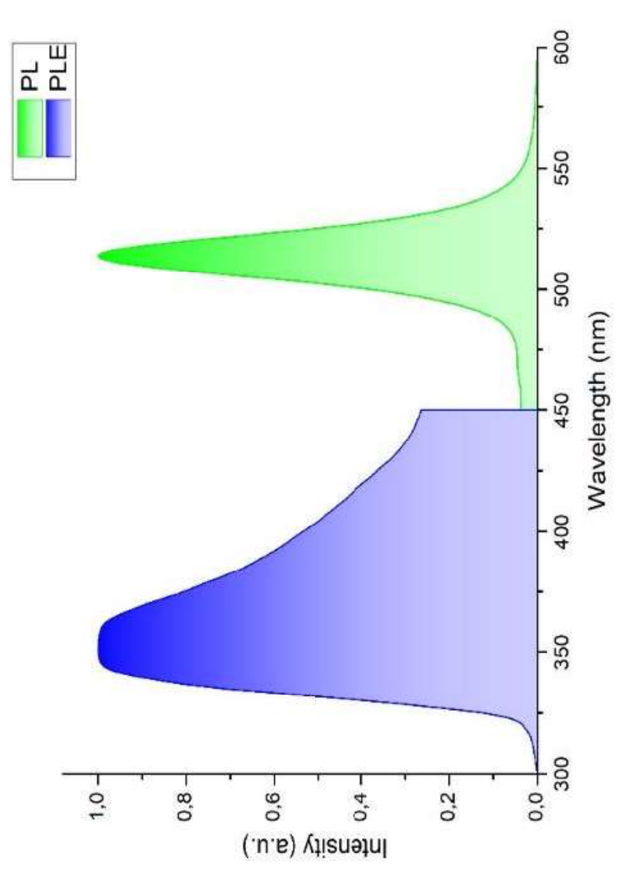	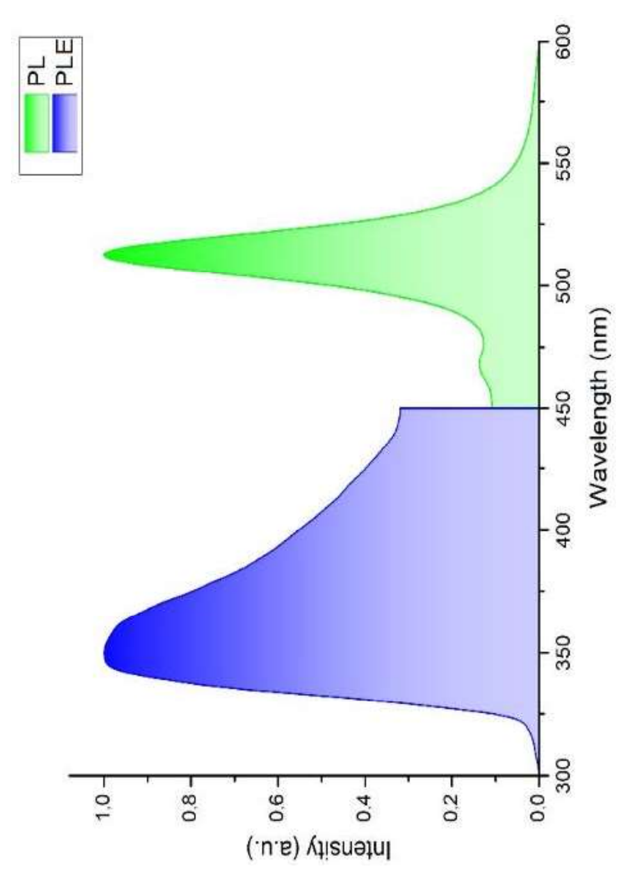

RTP21-2

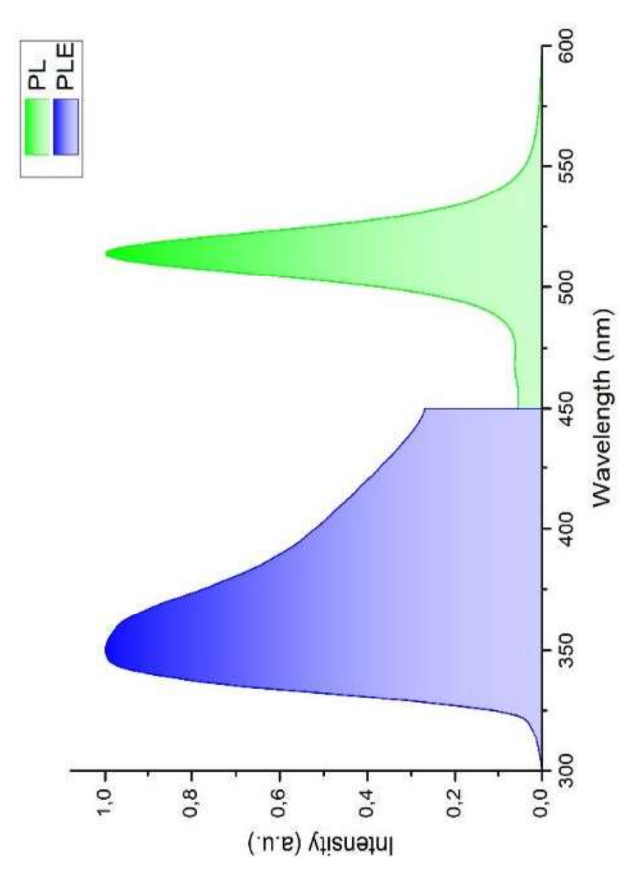

RTP24-12

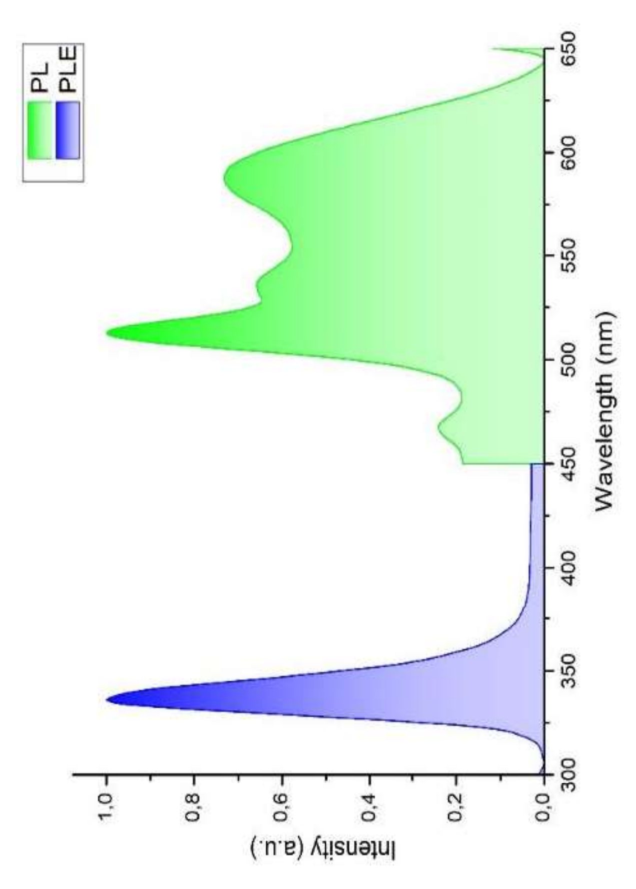

RTP38-2

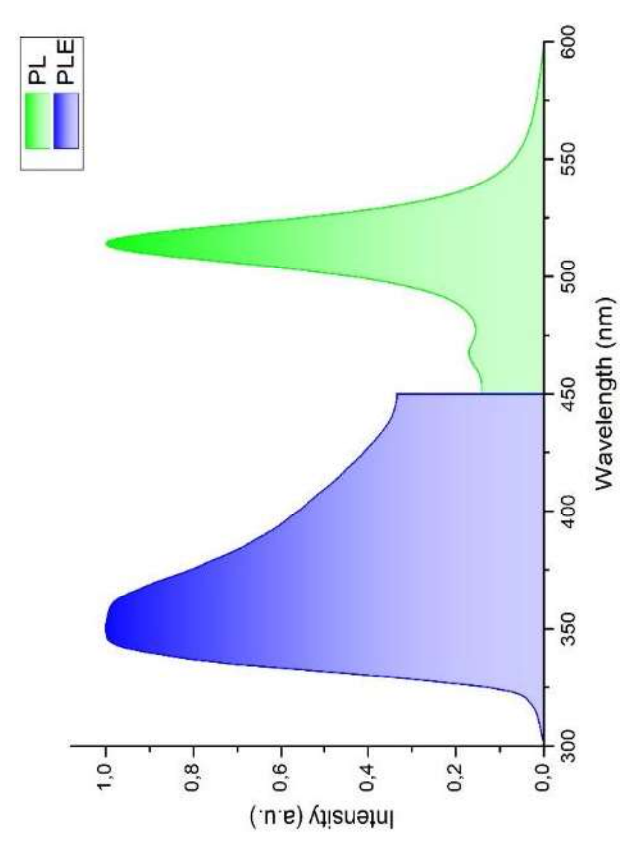

RTP43-2

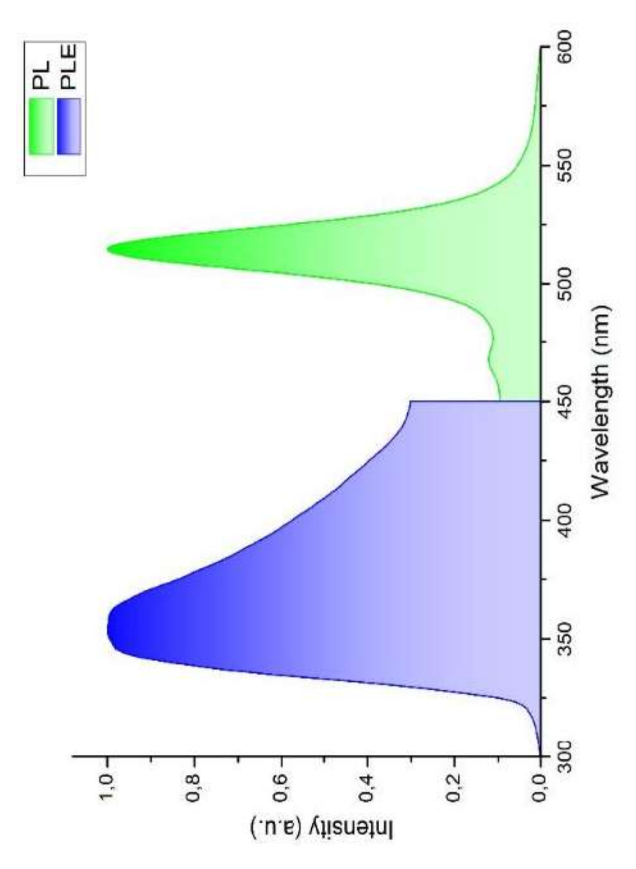

RTP42-2	RTP41-2